The Dissertation Committee for Karthik Kumar Certifies that this is the approved version of the following dissertation:

Microelectromechanical Handheld Laser-Scanning Confocal Microscope: Application to Breast Cancer Imaging

Committee:

Xiaojing (John) Zhang, Supervisor

Dean P. Neikirk, Co-Supervisor

Michael F. Becker

H. Grady Rylander III

Thomas E. Milner

Tse-Kuan Yu

Microelectromechanical Handheld Laser-Scanning Confocal Microscope: Application to Breast Cancer Imaging

by

Karthik Kumar, B.E.; M.S.

Dissertation

Presented to the Faculty of the Graduate School of

The University of Texas at Austin

in Partial Fulfillment

of the Requirements

for the Degree of

Doctor of Philosophy

The University of Texas at Austin

May 2009

Dedication

For Gayathri

Acknowledgements

This has been a fabulous experience.

Indeed, studying at the University of Texas has afforded me such grand luxuries as sitting atop a Helimak contemplating the mysteries of plasma physics, working in state-of-the-art cleanrooms with absolute mastery over the nanoscale, and applying my devices to important clinical problems at the very best medical institutions. Along the way, I have had the good fortune to befriend great minds, caring mentors, able colleagues, and true friends who taught me what I could not have learnt alone. And did I mention that I met the love of my life in the middle of all this?

I shall forever be indebted to Texas. Hook ‘em.

Of the many who have contributed to my professional development during my time here, I am able to explicitly thank but a few. Prof. John Zhang has been a sage advisor, and has led by example with his work ethic, determination, and commitment to excellence in research. Professors Grady Rylander and Tom Milner took a chance on me and gave me the first opportunities to work in biomedical optics, for which I remain grateful. They have been a constant source of encouragement and guidance ever since I entered graduate school. Prof. Michael Becker, through his irrepressible enthusiasm for teaching Fourier Optics, inspired me to think creatively. The experiments on “objective-less microscopy” detailed in Chapter 5 bear his mark. Prof. Dean Neikirk reminded me to never lose sight of the big picture, candidly assessed my work, and helped me achieve clarity of thought in analyzing all aspects of this research. Prof. Tse-Kuan Yu at the University of Texas M.D. Anderson Cancer Center provided objective and practical advice regarding imaging experiments, which proved extremely important to the timely completion of this work.

I am thankful for the valuable contributions and insightful advice of several collaborators and colleagues. Professor Jonathan Uhr and the team at the University of Texas Southwestern Medical Center (UTSW) provided cancer immunobiology expertise. It was a pleasure working on swine liver imaging with Dr. Rony Avritscher and the Dunn lab at M.D. Anderson Cancer Center, where I even got the opportunity to participate in necropsies! My co-workers at Zhang Lab, past and present, have made working in the lab a most enjoyable experience. I make special mention of our research associate, Dr. Kaz Hoshino, for this dissertation would not have been possible without him. の勤勉な調査千日よりよいすばらしい教師を 含む1日は。. Mary Tang, Ed Myers, Eric P., and many others at Stanford Nanofabrication Facility kindly shared their wealth of process development experience. Many thanks also to J.R. Watson and his crew of machinists at Applied Research Laboratories for their services while developing the handheld probe.

Primary financial support of this research by the Wallace H. Coulter Foundation Early Career Translational Research Award is gratefully acknowledged. The work reported herein on optical coherence tomography was supported by grants from the National Institutes of Health (R01 EY 016462) and the Veterans Administration. The micromirrors were fabricated by the author at Stanford Nanofabrication Facility and University of Texas at Austin Microelectronics Research Center, both supported by the National Science Foundation under the National Nanotechnology Infrastructure Network. The University of Texas Southwestern Tissue Repository at UTSW provided the human specimens used for this research. Control images were obtained using equipment at the Core facilities within the Institute for Cellular and Molecular Biology at the University of Texas at Austin.

Microelectromechanical Handheld Laser-Scanning Confocal Microscope: Application to Breast Cancer Imaging

Publication No._____________

Karthik Kumar, Ph.D.
The University of Texas at Austin, 2009

Supervisor: Xiaojing Zhang
Co-Supervisor: Dean P. Neikirk

Demographic data indicate that 60% of 6.7 million annual global cancer mortalities and 54% of 10.8 million new patients are in developing nations, unable or unwilling to avail of invasive screening tests that are the current norm. For most cancers, survival rate is strongly dependent on early detection, highlighting the need for improved screening methods.

Studies have shown that cancers can be identified based on distinct sub-cellular morphological features and expression levels of specific molecular markers. Since 85% of cancers are known to originate in the epithelium, portable *in vivo* imaging techniques providing sub-cellular detail in tissue up to depths of 250 μm could help improve access to biopsy-free examination in low-infrastructure environments. The resultant early detection could dramatically improve patient prognosis, while reducing screening costs, treatment delay, and occurrences of unnecessary and potentially harmful medication.

This dissertation investigates handheld instrumentation for laser-scanning confocal microscopy (LSCM) and its applicability to breast cancer detection and subsequent image-guided management. LSCM allows high-resolution mapping of spatial variations in refractive index or tumor marker expression within a single cell layer situated few hundred micrometers beneath the tissue surface. The main challenge facing miniaturization lies in the mechanism of beam deflection across the sample. The first part of the dissertation presents a fast, large-angle, high-reflectivity two-axis vertical comb driven silicon micromirror fabricated by a novel method compatible with complementary metal-oxide-semiconductor processing employed in the semiconductor industry. The process enables integration of rotation sensors on the chip to adaptively correct for aberrations in beam scanning while significantly reducing fabrication costs and barriers to market acceptance. The second part of the dissertation explores the integration of this micromirror with other optical and electronic components into a handheld laser-scanning confocal microscope. Applicability of the probe to epithelial breast cancer screening via reflectance and fluorescence imaging is investigated. Finally, enhanced imaging modalities based on the micromirror are presented. 3D cellular-level *in vivo* imaging via rapid swept-source optical coherence tomography is demonstrated. A method for "objective-less" microendoscopy, potentially resulting in substantially reduced probe dimensions, employing reflective binary-phase Fresnel zone plates monolithically integrated on the surface of the micromirror is presented.

Table of Contents

List of Tables

List of Figures

CHAPTER 1

INTRODUCTION

1.1 Motivation

Demographic data indicate that each year, 6.7 million mortalities result from, and an additional 10.8 million new patients are diagnosed globally with the collection of diseases commonly referred to as cancer [1, 2]. 60% of the mortalities and 54% of the new cases are in developing nations, where patients have limited access to sensitive screening tests and advanced healthcare facilities. The management of cancer in these patients is further complicated by the fact that cancers vary significantly in their molecular biology, clinical presentation, and outcome [3]. Sensitive, informative, portable, and cost-effective tools are therefore required to diagnose the condition, understand the unique signatures characterizing each patient's disease, and tailor treatment strategies individually. A clear understanding of the epidemiology, risk factors, pathogenesis, characteristics, and current management strategies employed for an organ-specific cancer is required in order to make these engineering contributions effective. Here we embark on a brief survey of the facts surrounding breast cancer and its current management strategies, for we envision the contributions outlined in this dissertation to, eventually, aid in this cause.

Globally, breast cancer is the most common cause of death by cancer in women, accounting for 16% of cancer mortalities [2]. In the United States, breast cancer is the leading cause of cancer death for women aged 20 to 59 years [4, 5]. In 2005 alone, 211,240 new cases (second to skin cancer) and 40,410 deaths (second only to lung cancer) were reported for women. Reported incidences of breast cancer has steadily risen

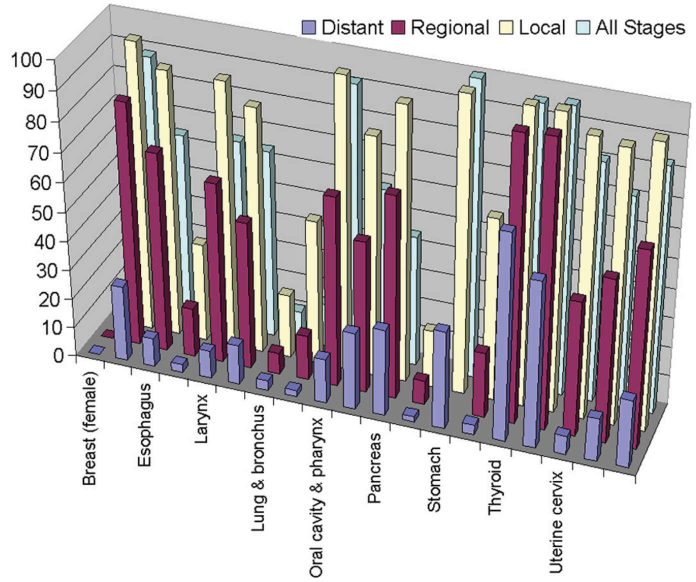

Figure 1.1: Graph of 5-year relative survival rate by cancer type and spread extent [4].

since the 1980s; this is attributed to, among other factors, increased screening by mammography and other techniques, lower levels of physical activity, and delayed childbearing [4]. Mortality rates have dropped in recent years, however, largely due to increased awareness, earlier detection of the condition through increased screening, and improved treatment options. Early detection is high on the future agenda of oncologists because of significant evidence that it will result in a higher cure rate [6, 7]. The importance of early detection by screening is highlighted by studying the dependence of survival rates on the stage at which the disease was diagnosed. Figure 1.1 shows the graph of five-year survival rates [4] for different types of cancers, including breast cancer, against the stage of the tumor when the condition was diagnosed. The most evident observation is that survival chances are far better if a diagnosis is obtained when the tumor is confined locally than when metastasis has occurred, due to the availability of better treatment options that are less toxic to normal tissues in the former case.

1.2 Rationale for approach

1.2.1 Cancer identifiers

Knowledge of the morphological and phenotypic changes that accompany cancer pathogenesis is important for building tools and determining criteria to diagnose the condition early. Cancer progression usually begins with hyperplasia (abnormal increase) of normal and atypical cells, to non-invasive carcinoma *in situ*, and finally to invasive cancer [8, 9]. In the case of breast cancer, hyperplasia usually begins with non-malignant epithelial cells that line the ducts and lobules within the breast. The cells of the non-malignant tumor, gradually increasing in number, can differ in size, shape and orientation from the surrounding normal tissue. Specifically, they are larger, have small cytoplasmic regions, indistinct cell borders and little to no nucleoli. The carcinoma *in situ* that develops from such regions is typically characterized by necrosis (unnatural localized cell death) and calcification of the resulting cellular debris. The carcinoma then invades the basal membrane of the duct or lobule. At this point, the tumor has the potential to spread through the rest of the organ and invade the lymphatic system, causing significant structural changes including lymphoedema and skin thickening. From here, the cancer can metastasize to other parts of the body.

In addition to morphological changes such as those described above, distinct molecular signatures present themselves at various stages of the tumor. The uncontrolled growth of abnormal cells characteristic of cancer can result from alterations of the cell signaling network that controls cell proliferation, that may pose as molecular markers [9]. As examples, *p53* is the most commonly mutated gene in human cancers. The *p53* gene plays a pivotal role in the suppression of cell cycle progression, which is inactivated by mutation in a variety of tumors [10]. The *Bcl-2* gene family mediates apoptotic (programmed cell death) behavior, and has been implicated in a number of cancers [9, 11]. The *Her-2* gene has been associated with increased cell division, malignant transformation, and metastasis [10, 12]. Increased exposure to certain hormonal factors may also stimulate breast cancer progression. For instance, estrogen can regulate the expression of mRNA of some of the modulatory proteins in the apoptotic pathway [13].

1.2.2 Image-guided intervention in cancer management

Tools that have the ability to measure the expression levels of proteins that are products of the breast cancer-associated genes will be important in breast cancer management. Imaging techniques are often touted as the best method for detection, diagnosis, and clinical management of breast cancer [14]. The primary tools in current use for this purpose are mammography, magnetic resonance imaging (MRI), positron emission tomography (PET), ultrasonography and single photon emission computed tomography (SPECT). These methods have traditionally relied on discerning structural and anatomic features [15], and typically only detect tumors after they have grown to 1-2 cm in size, by which time micro-metastasis may have occurred and the condition is no longer confined locally. Their ability to render large volume scans can be useful in certain surgical and therapeutic procedures, but are non-ideal in that they provide limited spatial resolution [16]. Some of these methods are also not easily adaptable to molecular imaging (i.e., the ability to image regional biochemistry and molecular biology), a feature that has the potential to be a powerful tool in clinical breast cancer management [3, 15, 17-21]. Optical imaging methods, in contrast to these, can provide extremely high spatial resolution and sensitive mapping of both morphological features and physiological function of tissues in inexpensive and portable instrumentation [16]. Although optical methods have limited penetration from the tissue surface, the ability to develop minimally-invasive endoscopic probes indicates their strong potential to complement existing low-resolution methods for sensitive and accurate imaging of the structural and functional elements of non-palpable breast tumors.

1.2.3 Abilities of the handheld laser-scanning confocal microscope

We have developed a handheld laser-scanning confocal microscope for breast cancer imaging addressing the above technological niche that complements existing breast cancer imaging methods. The instrument is capable of resolving sub-cellular morphological and physiological features of tissues via reflectance and fluorescence confocal imaging of optical sections up to 250 μm beneath the tissue surface. Single-cell-layer optical sectioning, comparable to conventional histology, is obtained without the need for multiple excisional biopsies. Manufacturing processes that exploit the economy of scale and precision engineering of the silicon nanofabrication industry are leveraged to achieve high-quality and cost-effective handheld probes. The instrument is designed in a single-fiber, portable format to help improve access to biopsy-free examination in low-infrastructure environments. The resulting early detection and high-resolution, sensitive mapping of structural and physiological function could dramatically improve patient prognosis, while reducing screening costs, treatment delay, and occurrences of unnecessary and potentially harmful medication.

1.3 Contributions

Minimally invasive optical imaging instruments that can discern the morphological and physiological changes that accompany cancers can revolutionize the field of breast cancer management. Fast-scanning mechanisms for deflecting the excitation illumination across the sample in a raster fashion form the core technological components in realizing high-resolution, real-time *in vivo* imaging systems for applications in biomedicine. Silicon micro-electro-mechanical system (MEMS) technologies are ideally suited to creating these actuating microstructures that can be incorporated into compact imaging systems. The use of silicon as the mechanical material in devices fabricated by processes employed in the electronics industry allows for co-fabrication of the MEMS systems with complementary metal-oxide-semiconductor (CMOS) transistor logic [22, 23]. This can enable integration of position sensors, control electronics, and power systems with the MEMS system on the same chip for fast feedback-controlled operation, resulting in high-quality, real-time imaging abilities.

This dissertation presents three specific intellectual contributions. First, we have developed a simple, high-yield, 3-mask, CMOS-compatible micromachining process for creating two-axis silicon scanning micromirrors for use in the imaging probes. The MEMS structure can be co-fabricated with feedback control electronics, angular position sensors and power amplifier systems. The fabrication process provides fast large-angle scanning micromirrors with high-quality optical surface characteristics, with the potential of incorporating adaptive scan control systems and micromirror drive electronics for monolithically integrated CMOS-MEMS designs towards hand-held microendoscope applications in biomedicine.

Second, we demonstrate a handheld laser-scanning confocal microscopy probe incorporating the high-reflectivity two-axis scanning micromirror. The instrument provides the single cell layer optical sectioning and sub-micrometer lateral resolution imaging, comparable to conventional histology, that we set out to achieve to enable biopsy-free sensitive examination of tissue structure and function. We fabricated the handheld probe incorporating batch-fabricated rapid prototyped components for MEMS packaging, providing a first step to creating disposable one-time-use probes.

Finally, we show through initial experiments that the instrument is able to detect histologically relevant morphological and physiological features in human epithelial breast tissue, aided by molecular contrast agents (for functional imaging). Several prior studies have been devoted to *in vivo* cancer targeting using molecular contrast agents. Our research in developing sensitive optical imaging instrumentation complements this work to enable, in the future, biopsy-free detection of labels specifically associated with breast cancer.

1.4 Dissertation Roadmap

The motivations for the dissertation and rationale behind the choice of approach are introduced in Chapter 1. An overview of microelectromechanical system (MEMS) technologies that can enable the development of compact handheld probes is presented in Chapter 2, followed by our enhanced method for CMOS-compatible micromirror fabrication. The theory of micromirror actuation is also outlined using which the performance metrics desired for the optical imaging system can be translated into a detailed micromirror design. Chapter 3 presents the details of design and assembly of the handheld laser-scanning confocal microscope incorporating our scanning micromirrors. The imaging experiments to validate the instrument are described in Chapter 4. Chapter 5 described two examples of imaging enhancements that can be achieved by use of the scanning micromirrors – 3D optical imaging and compact "objective-less" microendoscopy. 3D optical imaging is demonstrated using a micromirror-based swept-source optical coherence tomography instrument, and a micromachined scanning Fresnel zone plate objective is demonstrated as a micro-mechanical platform for compact imaging modules. Finally, Chapter 6 summarizes the dissertation and presents future research directions.

CHAPTER 2

CMOS-COMPATIBLE 2-AXIS SCANNING MICROMIRROR

2.1 Introduction

Fast-scanning mechanisms for deflecting the excitation illumination across the sample in a raster fashion form the core technological components in realizing high-resolution, real-time *in vivo* imaging systems for applications in biomedicine. Several approaches have been explored previously to achieve this functionality in small form factor. Proximal scanning systems wherein a micro-optics fiber-based assembly is translated axially and/or rotated [24] within a protective sheath have been employed in imaging modalities that require only slow scan rates in sideways-imaging systems. Forward-imaging requires fiber-bundle imaging or a distal scan mechanism. A fiber-optic bundle consisting of thousands of closely spaced fibers packaged with an objective lens has been used for *in vivo* imaging [25] by selecting, at the proximal end, the fiber through which the illumination is directed, and scanning through all the fibers sequentially. Though compact, this method suffers heavily from pixilation imaging artifacts and lowered spatial resolution due to finite spacing between adjacent fiber cores. Distal scanning has been achieved by fiber/objective translation [26, 27]. These techniques suffer from slow scan rates and limited field of view either by demagnification of the objective lens or optical aberrations. The most promising technique for fast-scanning units is micromirror-based angular beam deflection. Micromirrors driven by piezoelectric [28], thermal [29-32], magnetic [33-35] and electrostatic [36-50] actuation schemes have been explored previously. Electrostatic vertical combdriven single-crystal-silicon (SCS) micromirrors [41-43, 51] have become popular by virtue of their ability to provide large actuation torque and deflection angles in resonant or non-resonant operating modes while minimizing mirror surface roughness, and dynamic mirror deformation.

Silicon micro-electro-mechanical system (MEMS) technologies are ideally suited to creating the fast-moving micromirror mechanical structures that can be incorporated into compact imaging systems. Five specific advantages of silicon MEMS systems are touted over conventional techniques. First, the significant mass reduction associated with scaling the dimensions of the device to the micrometer range results in high vibrational frequencies of the resonant mode shapes of the device, which can be utilized for fast scanning. Second, MEMS technologies exploit the tremendous body of knowledge and precision nanofabrication facilities developed over five decades of explosive research and growth of the semiconductor industry. These devices, employing silicon as a mechanical material, can therefore exploit the economies of scale obtained by batch-fabrication, while leveraging the unprecedented precision and repeatability of the fabrication methods adopted in the consumer electronics industry, with minimal additional process development costs [52]. Third, the use of silicon as the mechanical material in devices fabricated by processes employed in the electronics industry allows for co-fabrication of the MEMS systems with complementary metal-oxide-semiconductor (CMOS) transistor logic. This can enable integration of position sensors, control electronics, and power systems with the MEMS system on the same chip for fast feedback-controlled operation [53], an innovative strategy that has recently gained much attention within the MEMS community [22, 23, 54]. Fourth, the reliability of such micro-mechanical vibrating structures depends on the stress encountered at the point of maximum load. Again, as a consequence of the scaling properties of the physical laws governing their operation, the fracture stresses experienced by micromechanical structures are usually an order of magnitude lower than macro-scale systems [55]. The reliability for these devices is therefore expected to be high as evidenced by the success of the DMD™ chip pioneered by Texas Instruments. Finally, the small overall size of these devices allows for integration into compact microendoscopes, which is important for translation of innovative optical technologies from research laboratories to clinical application, a primary goal of this dissertation.

The present research attempts to combine the advantages of the electrostatic combdriven micromirrors with CMOS-compatible silicon processing technology. Electrostatic combdriven micromirrors, despite their advantages, have certain deficiencies. They do not offer perfect linear transformation between input voltage and mechanical scan angle, and can often experience scanning instabilities due to pull-in phenomena [52, 56, 57]. Complicated comb self-alignment procedures have therefore been adopted in micromirror fabrication to mitigate this problem [36-38, 42, 43, 49]. We address these drawbacks by introducing a simple 3-mask comb self-aligned micromirror fabrication process compatible with traditional CMOS processing in the semiconductor industry. The major advantage is the monolithic integration of the IC and MEMS components towards multifunctional and intelligent microsystems. Our process only utilizes conventional silicon processing tools which operate at temperatures low enough to allow pre-fabrication of CMOS circuitry on the wafer prior to commencing micromirror fabrication. For microendoscopes, this can enable CMOS-MEMS integration of power systems, control electronics and sensors to adaptively correct for aberrations in beam scanning, while significantly reducing fabrication costs and barriers to clinical applications and market acceptance. Here we outline the considerations that affect the micromirror design process, describe our novel CMOS-compatible micromachining sequence, and present the fabricated device with performance characterization results.

2.2 Micromirror Design

The design of the electrostatic actuators for rotary micromirrors requires careful consideration of several optical and micromechanical parameters including scanning angle, micromirror mass, properties of the structural material (silicon), number of resolvable points within the angular scan, comb capacitance, torsion spring constants, the micromirror resonant mode shapes and their frequencies, voltage pull-in criteria, and driving voltage limitations. The specific targeted performance characteristics and their dependencies are described here.

2.2.1 Optical performance considerations

The micromirror plays a critical role in determining the resolution, field of view, and contrast of the confocal microscope. Higher values of numerical aperture (NA) of the objective system are required to obtain better optical sectioning with high contrast in highly scattering tissue samples. There is, however, an inherent trade-off that must be considered in selecting resolution and field of view. The product of the micromirror size and its optical deflection angle determines the number of resolvable points in the image [58], which translates into a given field of view and resolution according to the NA of the objective system. The equations (2.1) below elucidates this trade-off principle. The number of resolvable points, *N*, in a one-dimensional scan is given by –

$$N = H/R = (4f\theta)/\left(1.22\,\lambda f/D\right) \propto D\theta/\lambda \tag{2.1}$$

Here, H is the scan extent (field of view), R is the lateral resolution, f is the objective focal length, θ is the micromirror mechanical scanning half-angle, λ is the operating wavelength, and D is the micromirror diameter. Micromirrors with larger diameters (~ 1 mm) providing the same deflection angles can be designed, within the limits set by the maximum driving voltage that can be supplied and die size, at the cost of increased energy consumption (to actuate the larger mirror). Dynamic mirror deformation can also contribute to beam divergence and loss of optical resolution. The non-planar surface deformation of a rectangular mirror rotating at high frequency about a torsion spring is described by equation (2.2) [37, 59] as –

$$\delta = 0.183 \frac{\rho\left(1-\nu^{2}\right)\left(2\pi f\right)^{2}\theta}{Et^{2}} L^{5} \tag{2.2}$$

Here, δ is the mirror deformation, ρ is the material density, ν is Poisson's ratio, E is Young's modulus, f is the frequency of vibration of the structure, and t is the thickness of the mirror of side $2L$. The maximum peak-to-valley surface deformation tolerable without significant degradation in image resolution is $\lambda/4$, the Rayleigh limit.

We designed 2-axis silicon micromirrors with 1 mm diameter and a maximum half-angle mechanical scan of 5° to obtain ~ 450 resolvable points per line scan. The mirrors were designed to be 30 μm thick and operate at ~ 2.5 kHz resonant frequency for the fastest scan; we therefore calculated our dynamic mirror deformation to be approximately 0.5 nm, which is negligible compared to the operating wavelength of our system (635 nm). Finally the surface quality characteristic of a good optical element is usually defined as $<\lambda/10$. We therefore require our mirror RMS surface roughness to be <65 nm, which is a factor to be considered in the fabrication process development.

2.2.2 Staggered vertical electrostatic combdrives

Electrostatic vertical combdrives are one of the favored solutions to provide fast, high-torque rotary actuation about two axes of relatively massive microstructures, as discussed in the introduction. Figure 2.1 illustrates the actuating scheme within a staggered vertical combdrive. Here, the moving (upper) comb fingers rotate about the

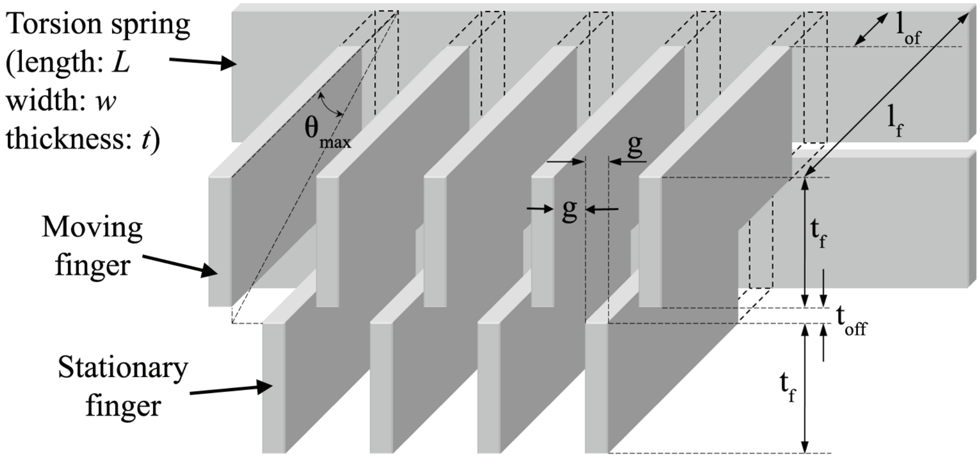

Figure 2.1: Schematic of the actuation mechanism of the staggered vertical combdrive, depicting the parameters affecting the rotation angle.

torsion spring on application of a voltage on the stationary (lower) comb fingers. When a voltage is applied at the stationary comb, an electrostatic torque is experienced by the moving comb as it is constrained primarily to rotary motion by torsion bar springs on either side of the micromirror. As the moving comb rotates, the torsion bars develop a shear stress due to twisting, and offer a mechanical restoring force against this action. The system reaches equilibrium at the rotation angle at which the electrostatic torque exactly matches the mechanical restoring torque. Equations (2.3-2.11) below describe the theoretical action of the system [34, 51, 57]. The electrostatic torque exerted by application of voltage on the stator is given by –

$$T_{Electrostatic} = \frac{1}{2}\frac{\partial C}{\partial \theta}V^2 \qquad (2.3)$$

Here, C is the total capacitance of the comb drive, θ is the rotation angle, and V is the voltage applied on the stator. For a staggered vertical comb drive (SVC) with N comb fingers, stator comb-to-rotor comb gap spacing of g, finger length l_f, and finger offset of l_{of}, the total capacitance of the SVC actuation system, for small values of θ, is given by equation (2.4) [51] –

$$C(\theta) = \frac{\varepsilon_0 N}{g}\left(l_f^2 - l_{of}^2\right)\theta = C_0\theta \tag{2.4}$$

The torsional stiffness of the springs can be expressed in terms of the geometry and material properties of the spring. Assuming each torsion spring has a length *L*, width *w*, thickness *t*, and is composed of a material with residual stress *σ*, elastic modulus *E*, and Poisson's ratio *v*, the angular torsional stiffness (k_ϕ) is given by [34, 60] –

$$k_\phi = 2\left(\frac{KG + \sigma J}{L}\right), \text{ where } \ldots$$

$$K = \frac{a^3 b}{3}\left[1 - \frac{199a}{\pi^5 b}\sum_{n=1,3,5\ldots}^{\infty}\frac{1}{n^5}\tanh\left(\frac{n\pi b}{2a}\right)\right],\ a = \min(w,t),\ b = \max(w,t),$$

$$G = \frac{E}{\left[2(1-\nu)\right]}, \text{ and}$$

$$J = \int_S \rho^2 dS \tag{2.5}$$

J is the polar moment of inertia [61] calculated by integrating the square of the radial distance *ρ* of each elemental surface area *dS* over the entire micromirror structure. The mechanical restoring torque provided by the torsion rods is simply $T_{\mathrm{Re}storing} = -k_\phi\theta$, and the equation of motion for the structure is –

$$\frac{1}{2}\frac{\partial C}{\partial \theta}V^2 = -k_\phi\theta \tag{2.6}$$

Based on equation (2.4), a solution to equation (2.6) takes the form –

$$\theta = \alpha V^2, \text{ where } \alpha = \frac{C_0}{2k_\phi} \tag{2.7}$$

The resonant frequency for rotation about an axis defined by the orientation of the torsion springs of the micromirror is given by [36] –

$$f_{resonance} = \frac{1}{2\pi}\sqrt{\frac{k_\phi}{J}} \tag{2.8}$$

The analysis above assumes that the phenomenon of pull-in of the SVC does not occur for the actuating voltages applied, and that the rotation angle θ is small. The maximum continuous rotation angle of the SVC driven micromirror is determined as the angle at which $C(\theta)$ becomes maximum, i.e. –

$$\theta_{SVC}^{\max} = \frac{t + t_{off}}{l_f} \tag{2.9}$$

The distinctly favorable pull-in characteristic of the SVC drive system differentiates it from other electrostatic actuation schemes, and is the reason for its selection to achieve the aims of this dissertation. The theory described above assumes that the torsion springs will always be able to provide mechanical restoring torque equal to the electrostatic torque. Pull-in occurs when the electrostatic torque starts overcoming the restoring torque, and the moving comb is abruptly pulled towards the fixed electrode. The point of pull-in is when they are equal, and their first derivatives are also equal [56] –

$$\frac{1}{2}V^2\left(\frac{\partial C}{\partial \theta}\right)_{\theta=\theta_{PI}} = k_\phi \theta_{PI} \tag{2.10}$$

$$\frac{1}{2}V^2\left(\frac{\partial^2 C}{\partial^2 \theta}\right)_{\theta=\theta_{PI}} = k_\phi \tag{2.11}$$

Substituting equation (2.11) in (2.10), and eliminating voltage V yields –

$$\left(\frac{\partial C}{\partial \theta}\right)_{\theta=\theta_{PI}} - \theta_{PI}\left(\frac{\partial^2 C}{\partial^2 \theta}\right)_{\theta=\theta_{PI}} = 0 \tag{2.12}$$

If we define the left hand side of equation (2.12) to be the pull-in investigation function $PI(\theta)$, the solution of the equation $PI(\theta)=0$ yields the pull-in angle. Based on equation (2.4), we find that only in the case of the SVC actuation system, the pull-in function is always positive ($PI(\theta) = C_0$ for all θ), which means that pull-in never occurs along the dominant direction of actuation for the SVC actuator. This is a significant advantage over other electrostatic actuation systems. There are other modes of pull-in that are possible with the SVC drive caused mainly by comb misalignment; however these modes will also exist for any other electrostatic actuation schemes considered. A detailed analysis of the other modes of pull-in for SVC drives may be found in Ref [57].

2.2.3 Finite element analysis

The analytical characterization of the performance of a two-axis scanning micromirror is a complicated task due to the difficulty of calculating the polar moment of inertia and torsional spring constants for a complex 3D multi-layer structure consisting of one of more materials. Finite element analysis (FEA) provides a useful tool to determine the resonant mode shapes and associated vibration frequencies for complex microstructures. We simulated the modal behavior of our scanning micromirror in CoventorWare™, an FEA tool optimized for analysis of MEMS structures. The optimized simulated structure comprises a circular micromirror having diameter of 1024 μm and thickness of 30 μm, supported within an annular structure of width 112 μm by a set of torsion springs having dimensions 220 × 8 × 30 μm^3. The annular gimbal structure is anchored to the silicon substrate via two sets of torsion springs, aligned orthogonally to

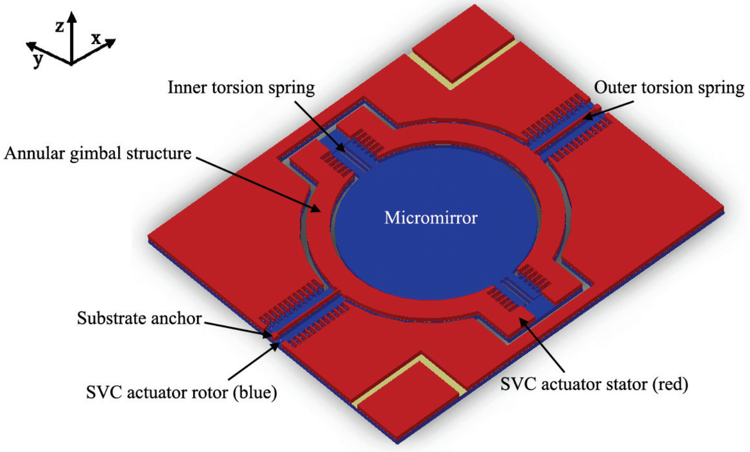

Figure 2.2: Schematic of two-axis SVC actuator-driven scanning micromirror modeled in CoventorWare™ Finite Element Analysis software.

the inner torsions springs suspending the circular micromirror within the annular structure. The outer torsions springs comprise two silicon rods, each having dimensions 412 × 8 × 30 μm^3, stacked one on top of the other with a 1 μm thick layer of insulating silicon dioxide sandwiched between them. The final dimensions of each of these torsion springs are therefore 412 × 8 × 61 μm^3. Two sets of SVC drives are provided for bi-directional rotation about the scanning axes, each having 12 (for inner axis) or 24 (for outer axis) comb fingers, comb finger lengths varying from 120 μm to 250 μm, 56 μm finger offsets, and 8 μm stator-rotor finger spacing. Figure 2.2 depicts the final structure of one of the simulated micromirror models. Deformation shapes of the six vibration modes of lowest frequency were determined, along with the associated resonance frequencies. Since we are primarily interested in inducing rotary motion about the two axes defined by the torsion rods in our system, we designed the system such that these

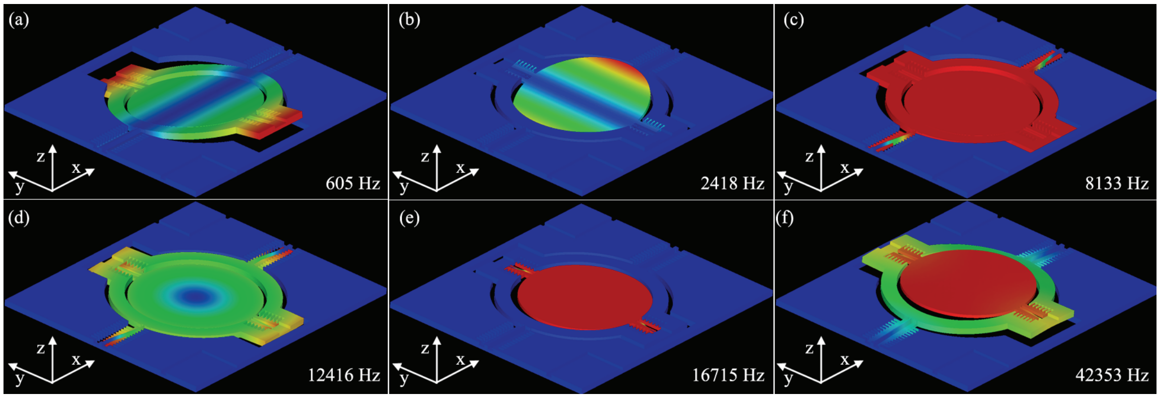

Figure 2.3: Vibration mode shapes of the six modes of lowest resonance frequency of the two-axis SVC driven scanning micromirror simulated by Finite Element Analysis in CoventorWare™. (a) Out-of-plane tilt about the outer rotation axis. (b) Out-of-plane tilt about the inner rotation axis. (c) In-plane translation by bending of the outer torsion springs. (d) In-plane rotation about z-axis by twisting of the outer torsion springs. (e) In-plane translation by bending of the inner torsion springs. (f) Out-of-plane translation (along z-axis) by bending of the outer torsion springs.

rotary mode shapes were the two with lowest resonance frequencies, corresponding to the deformation for which spring compliance is maximized. In the design process, we also attempted to maximize the separation, in resonance frequency space, between these modes and the other (unwanted) modes of vibration of the system. Figure 2.3 depicts the six vibration mode shapes of lowest resonance frequency, and Table 2.1 lists the mode shapes along with their optimized resonance frequency values.

Table 2.1: Simulated resonant mode shapes and frequencies of the micromirror

Mode No.	Axis	Mode	Frequency (Hz)	Actuation
1	Outer	Tilt (θ_x)	605	Desired
2	Inner	Tilt (θ_y)	2,418	Desired
3	Outer	Translate (y)	8,133	Bending (undesired)
4	Outer	Twist (θ_z)	12,416	Rotation (undesired)
5	Inner	Translate (x)	16,715	Bending (undesired)
6	Outer	Translate (z)	42,353	Bending (undesired)

2.3 Microfabrication Process Development

2.3.1 Considerations: CMOS compatibility

A multitude of factors must be considered in the process of developing a micromirror fabrication sequence, including –

(a) Wafer yield (percentage of devices functional after process completion)

(b) Complexity and cost of the fabrication process (i.e., number of masks/ wafer bonding, grinding or polishing steps)

(c) Materials compatibility and equipment contamination restrictions

(d) Incorporation of etch stop layers for robust etch control

(e) Equipment etch capabilities (i.e., etch selectivity, aspect ratio-dependent etching, maximum etch depth, side wall profiles etc.)

(f) Tolerance for lithographic misalignment between photomask features

(g) Ability for in-process testing, and avenues for rectification of errors in previous processing steps

(h) Maximization of wafer surface used for the device active area (i.e., high fill factor of devices on the wafer) to minimize unused silicon

(i) Methods for releasing the micromechanical structure on the wafer, and

(j) Methods for dicing the wafer into small chips without affecting the released structures contained in each die.

Our fabrication process, in addition to addressing all of these requirements, allows for the pre-fabrication of CMOS circuitry prior to the MEMS process sequence due to its low 'thermal budget' [62]. We have ensured that the process utilizes only those conventional silicon processing tools requiring low operating temperatures, to prevent diffusion of previously implanted dopants during the MEMS fabrication steps. We have adopted a 'MEMS-last' fabrication strategy [22] where the micromachining of mechanical structural layers is performed after the completion of the CMOS back-end-of-line (BEOL) process steps. This modular strategy offers the advantage of being compatible with any integrated circuit (IC) fabrication process. If the MEMS fabrication sequence is designed to have thermal budget similar to that of a BEOL process, it may be simply considered as an additional (optional) BEOL process, and should have no effect on the CMOS front-end-of-line (FEOL) processes (especially the dopant diffusion steps). This means that the circuit designs need not be modified in any way, affording greater design flexibility and shorter design cycles. If the materials used in the MEMS fabrication sequence are CMOS compatible (which the materials used in our MEMS process are), the MEMS fabrication can be done as an extension of the CMOS processing. Also, the difficulties of performing photolithography on previously bulk-micromachined substrates present in 'MEMS-first' approaches are avoided, which is especially important where high aspect-ratio structures are needed in the MEMS structure (such as in the vertical combdrives actuating our micromirror).

2.3.2 Micromachining process sequence

We have created a simple, modular 'MEMS-last', CMOS-compatible 3-mask fabrication process for a two-axis scanning micromirror driven by self-aligned vertical combdrive actuators [63]. The starting material for the micromirror fabrication process is a <1-0-0> double silicon-on-insulator wafer having two 30 µm thick <1-0-0> silicon device layers separated from each other and the handle substrate by two buried layers of 1 µm thick silicon dioxide, as shown in Figure 2.4(a). Pre-fabrication of any CMOS circuitry can be done at this time. Following CMOS pre-fabrication, the wafer is cleaned by immersion in a 9:1 solution of H_2SO_4:H_2O_2 (Piranha solution) for 8 minutes, rinsed in de-ionized water, and spun dry. The wafer is directly inserted into a furnace in which a 1.5 µm thick layer of silicon dioxide is deposited by Low Pressure Chemical Vapor Deposition (LPCVD) at low temperature (450°C) to minimize thermal budget. This low-temperature oxide (LTO) serves to protect the CMOS circuitry during the MEMS processing steps, and also acts as a hard mask for the deep trench etching that will be performed to create the high aspect ratio vertical comb structures. Photolithography of

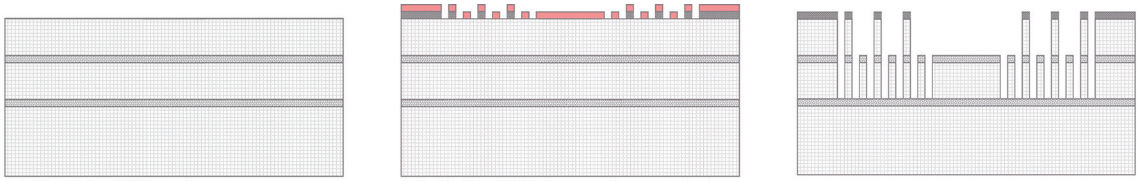

(a) Double-SOI wafer (d) Oxide RIE for mask completion (g) Deep RIE to create rotor features

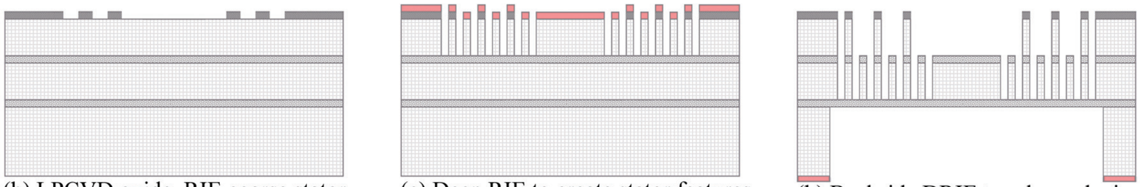

(b) LPCVD oxide, RIE coarse stator (e) Deep RIE to create stator features (h) Backside DRIE to release device

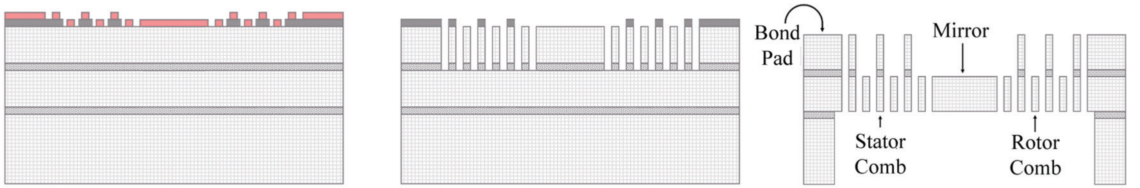

(c) Photolithography exact features (self-alignment) (f) Oxide RIE, resist removal (i) Cross-section of completed device

Figure 2.4: CMOS-compatible fabrication process for 2-axis scanning micromirrors driven by self-aligned staggered vertical combdrive actuators.

the coarse features of the micromirror is performed on the wafer using photomask #1. This involves coating a layer of hexamethyldisilazane (HMDS) on the wafer serving as an adhesion promoter between the wafer and a photo-sensitive polymer (Shipley SPR 220-3 positive resist), spinning this photoresist on the wafer, exposing parts of the photoresist to UV light through the photomask, and developing the film to remove portions of the resist that were exposed to UV excitation. The coarse features are etched into the full depth of the LTO by reactive ion etching (RIE) using CHF_3 and O_2 gases [Figure 2.4(b)]. A second photolithographic step over the etched LTO is performed using mask #2 to transfer the pattern of the exact features of the micromirror device to the photoresist. The features on this mask are aligned to the coarse features etched earlier into the LTO. Self-alignment of the rotor comb structures to the stator comb occurs during this alignment process [Figure 2.4(c)]. The misalignment tolerance for this lithography step is half of the gap spacing between fingers of the stator and rotor combs, which is 4 μm for the micromirror design on which we conducted FEA simulations. A significant advantage of our process is that, if the alignment is deemed to be unsatisfactory on inspection after the photolithography, the photoresist can be easily removed by a Piranha clean, and the self-alignment step redone as many times as necessary. This flexibility eliminates, by allowing simple in-process characterization and avenues for rectification of lithographic errors, any uncertainty in determining whether self-alignment is achieved, as may happen when the alignment needs to be performed to a layer buried deep within the materials stack [41, 42]. The wafer yield and device operating performance using this method is significantly improved over our previous efforts at using alignment to a buried layer [42]. Since the alignment procedure is extremely simple, the minimum comb gap spacing achievable is determined solely by the maximum aspect ratio that the silicon deep reactive ion etching (DRIE) tool used in subsequent steps can achieve. Oxide RIE to remove the exposed silicon dioxide trims the features of the LTO to match the overlying photoresist, completing self-alignment and etch mask formation. The photoresist remaining after oxide RIE is not removed and, in combination with the underlying LTO, forms the mask for deep etching [Figure 2.4(d)]. DRIE in an inductively-coupled plasma generator using SF_6/O_2 and C_4F_8 gases in a pulsed scheme (commonly known as the Bosch process), stopped on the first buried oxide layer, creates features of both stator and rotor combs in the upper silicon device layer [Figure 2.4(e)]. After oxide RIE of the intermediate buried oxide layer, the photoresist component of the mask is removed, leaving the rotor features in the upper device layer unprotected by any masking element, while the stator features are still protected by a layer of LTO [Figure 2.4(f)]. A second DRIE etch stopped on the second buried oxide layer removes the upper device layer silicon above the rotor combs while simultaneously defining the rotor features in the lower silicon device layer. After etch completion, the rotor layer features reside only in the lower layer of device silicon, while the stator layer extends through both device layers [Figure 2.4(g)]. The lower section of the stator features is redundant from an actuation perspective, but does not affect micromirror operation. Photolithography of thick (~ 15 μm) photoresist (Shipley SPR 220-7 positive resist), capable of protecting the underlying silicon through a substrate DRIE step, is performed on the backside of the wafer using mask #3 and employing backside alignment to the features on the front side of the wafer. Mask #3 contains the outline of the micromirror structure and is used to remove all silicon directly beneath the micromirror device. Since the feature on mask #3 is large (comparable to the size of the entire device), a significant amount of misalignment can be tolerated. The wafer is bound by photoresist to a second silicon substrate serving as a mechanical handle in preparation for backside substrate DRIE. Backside DRIE releases the devices [Figure 2.4(h)] and creates dicing lines to facilitate cleaving of the wafer into separate chips. The device wafer is separated from its handle wafer by soaking in acetone, following which oxide RIE is performed on the front and back sides of the wafer to remove any remaining exposed silicon dioxide ion the LTO mask and second buried oxide layers respectively [Figure 2.4(i)]. As a final step, metals, such as Chromium/Gold can be evaporated on the mirror surface through a shadow mask to improve reflectivity.

2.3.3 Fabrication results and discussion

For initial experiments, we fabricated micromirrors on wafers without any pre-existing CMOS circuitry. Figure 2.5 depicts scanning electron micrograph (SEM) images of the fabricated devices. The size of each chip was 2.8×2.8 mm^2. The micromirrors were of 1024 μm diameter, similar to those that we modeled in the FEA simulations.

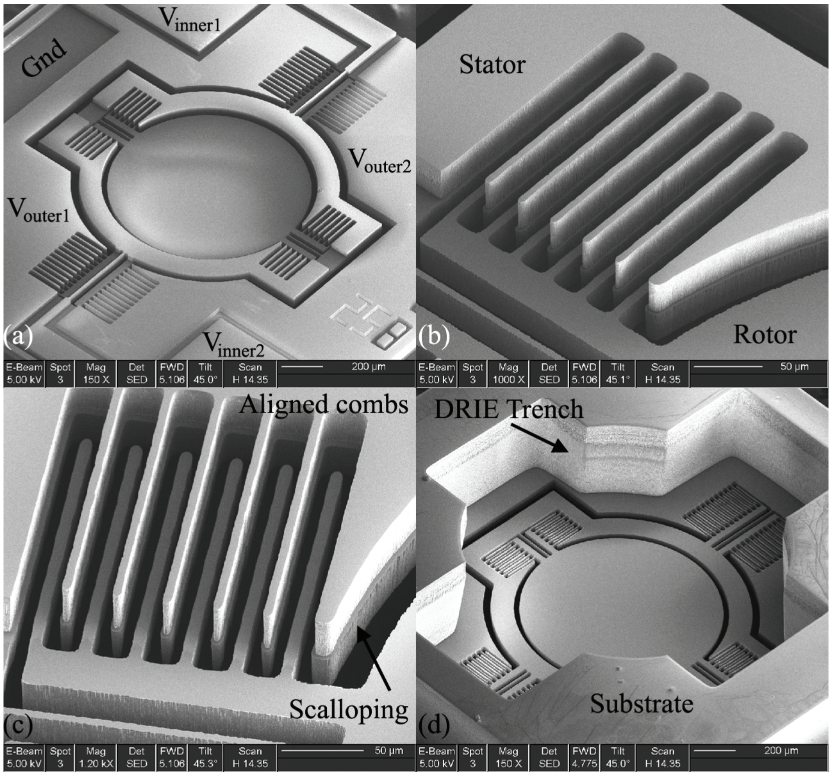

Figure 2.5: Scanning electron micrograph (SEM) images of the fabricated devices. (a) Top view of micromirror showing electrical bond pads, comb drives on both axes, and micromirror surface. (b) Close-in view of layers forming the combdrive actuator on the inner axis. (c) Close-in view of the quality of alignment between the stator and rotor comb fingers. (d) Backside view of the substrate DRIE through-etch, bottom face of the micromirror.

Each micromirror was actuated by two sets of SVC combdrive actuators for each rotation axis. Comb finger thickness and spacing between rotor and stator combs was fixed at 8 μm, yielding a 7.5:1 maximum DRIE etch aspect ratio, which is well within the abilities of most inductively-coupled plasma-based deep silicon etching systems. The quality of the self-alignment is assessed favorably, as evidenced from the SEM images in Figures 2.5(b-c). The stator comb fingers are well-defined, precisely aligned to the underlying rotor layer, and vertically offset by 31 μm. The distance between the rotor finger tips and the central axis of rotation was maintained at 200 μm or 250 μm. Some scalloping due to the pulsed nature of the DRIE Bosch process was observed [Figure 2.5(c)]; however this is expected to have a negligible effect on the micromirror operation. Final yield of usable chips from the wafers, for the two experimental runs of three wafers each, is estimated at over 85%. Damage to the micromirrors usually occurred in manual handling while releasing of the device wafer from the handle wafer after substrate DRIE, and during the cleaving of the wafers into miniature chips.

2.4 Device Performance Characterization

The performance of the laser-scanning confocal microscope is inevitably and strongly linked to the characteristics of the scanning micromirror. The characteristics of greatest interest therefore are micromirror surface roughness, micromirror response time (or alternatively, the frequency response curve), and static voltage optical deflection angles. These parameters will determine the aberration of the optical wavefront prior to focusing and thereby the imaging resolution, the field of view and number of resolvable image points, and frame rate, respectively.

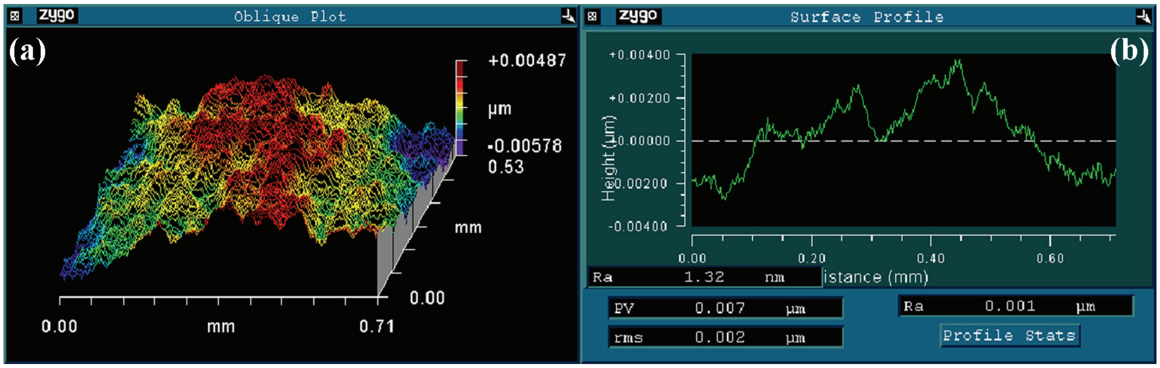

Ra 1.32 nm

PV 0.007 µm

rms 0.002 µm

Ra 0.001 µm

Figure 2.6: Sample micromirror surface roughness measurement using a white-light interferometer-based 3D surface profiler. (a) 2D map of surface roughness over 710 µm × 530 µm area. (b) 1D slice plot of mirror surface profile.

A critical requirement of the fabrication process is to ensure optical smooth mirror surface in the completed device. We measured the mirror surface roughness using a Zygo white-light interferometer-based 3D surface profiler to be 8 nm on averaging over devices from all process wafers. The measurement is performed over a 710 µm × 530 µm surface area positioned over the center of the micromirror. The surface quality is far better than the maximum tolerable RMS roughness requirement of $\lambda/10$ or 65 nm, as was discussed in section 2.2.1. A sample measurement from one of the micromirrors, indicating RMS roughness of 2 nm, is presented in Figure 2.6.

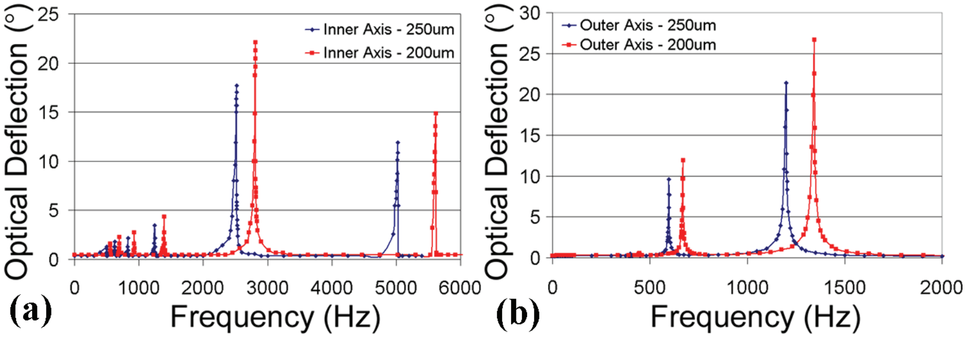

Figure 2.7: Frequency response characteristics of the two tested micromirror designs with comb tip-axis separation of 200 µm/ 250 µm. (a) Inner rotation axis response curves. (b) Outer rotation axis response curves.

The frequency response characteristics of the micromirror about the inner and outer rotation axes are presented in Figure 2.7. The responses were measured by applying a sinusoidal variable-frequency voltage with suitable offset (to ensure the applied voltage was always positive) between ground and one of the two combdrive actuators of each rotation axis. The response does not change significantly when voltages are applied to both combdrives, as the theoretical maximum double-sided deflection angle is found to be easily achieved even on application of voltage to just one actuator per axis. The devices exhibit resonances for the primary (desired) out-of-plane tilt mode shape at around 2.81 kHz and 670 Hz on the inner and outer rotation axes respectively. Optical scan angles of 22° and 12° on the inner and outer axes are observed for these resonant peaks respectively. Secondary resonance peaks are also observed at $2\omega_0$ and $\omega_0/2$, $\omega_0/3$, $\omega_0/4$ etc. (where ω_0 is the primary resonant frequency), as reported previously for micromirrors of similar configuration. The peaks below the primary resonance frequency are postulated to occur due to the non-linear relationship between voltage and electrostatic force [57]. The phenomenon is much more pronounced for rotation about the inner axis, which may be due to the smaller polar moment of inertia for the inner rotation axis compared with the outer rotation axis. This reduced polar moment of inertia also explains the downward shift in resonant frequencies for the micromirrors with 250 µm separation between the comb finger tips and the central rotation axis, as compared to the micromirrors with 200 µm separation.

While the micromirror can be operated at resonance for rotation about one axis in order to perform fast line scans, the other rotation axis must be operated at low frequencies in order to perform frame scans in raster-format point-by-point imaging

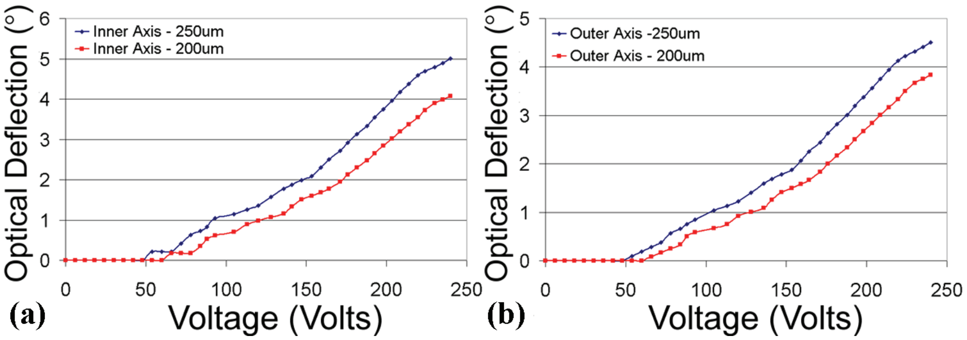

Figure 2.8: Static voltage response characteristics of the two tested micromirror designs with comb tip-axis separation of 200 µm/ 250 µm, when voltage is applied between ground and one of the two combdrive actuators per axis. (a) Inner rotation axis response curves. (b) Outer rotation axis response curves.

systems. The optical deflection angles for applied static (DC) voltages can reveal the efficacy of operation in this regime. Figure 2.8 presents the deflection curves for the inner and outer rotation axes of the micromirrors when a static voltage is applied between ground and one combdrive actuator on each rotation axis. Off-resonance actuation using only one combdrive actuator results in single-sided deflection; therefore we can double the total optical deflection angle by making use of both actuators on either side of the torsion bars forming the rotation axis. In this respect, off-resonance operation differs significantly from driving at resonant frequency. Single-side deflection angles of about 5° and 4.5° are observed on applying static voltages up to 240V on the inner and outer axes respectively. In our tests, the micromirrors with longer comb fingers (i.e., the ones with 250 μm separation between rotor comb finger tip and rotation axis) exhibited greater deflection for the same actuating voltage than those with shorter comb fingers. This can be explained by the fact that the total capacitance coefficient (C_0) of the combdrives of the former is greater than that of the latter. The curves in Figure 2.8 do not show any sign of decreasing slope for increasing voltages, indicating that the complete dynamic range of the micromirrors is not achieved for this voltage range of actuation. Increased deflection angles can be obtained by either using a high-voltage amplifier with a greater range of output voltages, or reducing the comb gap spacing and increasing comb finger length to increase the capacitance coefficient of the combdrive actuators. These combdrive design changes can be done within limits to improve the static voltage characteristics without introducing the risk of inducing pull-in modes of operation. Finally, the operating curves are not perfectly linear or smooth; this highlights the critical need for incorporating electronic feedback control systems in future generations of the device to improve off-resonance scan characteristics. Our CMOS-compatible micromachining process takes an important step forward in addressing this requirement.

2.5 Conclusions

The microelectromechanical two-axis scanning micromirror forms a core technological component enabling the miniaturization of forward-imaging probes for microendoscopy. The optical requirements of the application can be directly transformed into performance metrics required to be achieved by the scanning micromirror. Staggered vertical combdrive (SVC) actuated micromirrors can provide the fast scans, large deflection angles, and favorable mirror optical characteristics in small form factor required for real-time high-resolution *in vivo* imaging. The theory of SVC combdrives is outlined using which the performance metrics desired for the scanning system can be translated into a detailed micromirror design using finite element analysis (FEA) tools. We have developed a simple, high-yield, 3-mask, CMOS-compatible 'MEMS-last' micromachining process for co-fabricating feedback control electronics, angular position sensors and power amplifier systems with self-aligned SVC driven 2-axis micromirrors. The fabrication process provides fast large-angle scanning micromirrors with high-quality optical surface characteristics, with the potential of incorporating adaptive scan control systems and micromirror drive electronics for monolithically integrated CMOS-MEMS designs towards hand-held microendoscope applications in biomedicine.

CHAPTER 3

HANDHELD LASER-SCANNING CONFOCAL MICROSCOPE

3.1 Introduction

Medical imaging techniques play an important role in guiding the critical clinical healthcare decisions affecting patient outcomes. Point-of-care diagnostic methods improve patient prognosis by enabling the physician to diagnose medical conditions and deploy treatment options with confidence. The ability to detect diseases *in situ* at an early stage when they can be countered effectively, and to perform image-guided excisional microsurgery and monitored photodynamic therapy, is of particular importance in combating the global menace of cancer. There is significant evidence that patient survival rate would improve dramatically on early detection and excision of the primary tumors [6, 7]. Several studies have shown that precancers can be unambiguously identified based on the mapping of the overexpression of targeted tumor biomarkers specific to the cancer type [64-67] and sub-cellular morphological features, including nuclear size and nuclear-cytoplasm ratio [68, 69]. Since 85% of all cancers are known to originate in the epithelium [9], portable *in vivo* imaging techniques that can resolve sub-cellular detail in tissue up to depths of 250 μm could help improve access to biopsy-free examination in low-infrastructure environments. The resultant early detection can dramatically increase treatment options and improve patient prognosis, while reducing screening test costs, treatment delay and occurrences of unnecessary and potentially harmful medication. The same imaging techniques can be used for accurate tumor staging and margin assessment, and for image-guided excisional microsurgery and photodynamic therapeutics.

The choice of image technique employed in these operations depends on its efficacy for use in the particular organ environment. Traditional imaging techniques such as magnetic resonance imaging (MRI), ultrasound imaging, positron emission tomography (PET) and computed tomography (CT) are useful in surgical and therapeutic procedures requiring scans over large volumes. However, these techniques suffer from lowered spatial resolution and the inability to track the overexpression of specific molecular biomarkers that are the hallmark of most forms of cancer. These observations indicate that minimally invasive endoscopic high-resolution optical imaging methods can potentially fill this void in technology to improve the accuracy and outcome of delicate clinical procedures.

Optical imaging techniques, including conventional endoscopy, laser-scanning confocal and multi-photon microscopies, and optical coherence tomography can offer high sensitivity and spatial resolution at the cellular and sub-cellular levels. Laser-scanning confocal microscopy [70], in particular, allows sub-cellular resolution *in vivo* imaging of a single cell layer situated a few hundred micrometers beneath the tissue surface by performing biopsy-free optical sectioning comparable with histology [71]. Its flexibility in mapping either spatial variations in refractive index of native tissue or detecting fluorescent markers preferentially bound to tumor sites is an important factor in its selection over the other high-resolution optical imaging techniques for the purposes of this dissertation. Preliminary studies have shown that reflectance and fluorescence confocal microscopy can be useful in targeted cancer imaging [71-74]. Several of these studies have employed fiber-bundle based confocal imaging systems [75-77] that suffer from inherently lowered resolution due to the pixilation artifact arising from the finite spacing between adjacent fiber cores. Microelectromechanical systems technologies have been investigated to create miniaturized optical benches for micro-optical assemblies for microendoscopy [78-82]. The use of scanning micromirrors has only recently begun to be investigated for two-photon imaging [81, 83] and handheld single-axis [84-86] and dual-axes confocal microscopy [87, 88]. Here we describe a forward-imaging handheld laser-scanning microscope demonstrating sub-micrometer lateral resolution and single-cell-layer optical sectioning capability in reflectance and fluorescence confocal imaging based on 2-axis fast-scanning micromirrors, towards interventional micro-imaging.

3.2 System Design

We have developed a handheld forward-imaging single-fiber laser-scanning confocal microscope incorporating our fast high-reflectivity two-axis micromirror in the distal scanning mechanism. The single-fiber approach provides high-quality pixilation-free imaging and a simple approach to aligning the confocal pinhole to the image of the point on the sample created by the objective system [70]. The schematic of the optical layout of our system is provided in Figure 3.1. The semiconductor diode laser module LM (Blue Sky Research, Inc., FMXL-635-017-PA-0B), operating at a wavelength of 635 nm and maximum power of 17 mW, launches linearly polarized light into a polarization maintaining single-mode fiber PM, with the electric field of the coherent laser light oriented along the slow axis of the PM fiber. The PM fiber terminates at an optical bench (OFR, Inc., FT-38x100-3W) housing the components to extract light reflected from the sample. Light exiting the fiber is coupled into a second PM fiber (Oz Optics, Inc., LPC-01-635-4/125-P, 0.11 NA) through two identical collimating lenses CL (OFR, Inc., PAF-X-5-VIS) and a calcite walk-off polarizer POL (OFR, Inc., PB-5x7-16-VIS). The polarizer ensures that only light of polarization aligned to the slow axis the PM fibers enters the second fiber. This light diverges out of the exit aperture of the second fiber into

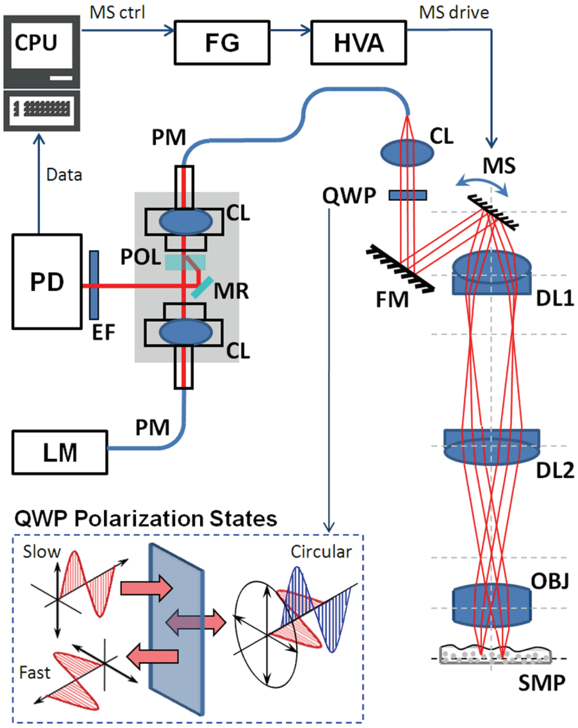

Figure 3.1: Schematic of the optical layout of the single-fiber laser-scanning confocal microscope. LM: laser module; PM: polarization-maintaining single-mode fiber; CL: collimating lens; QWP: quarter-wave plate; FM: folding mirror; MS: micromirror scanner; DL1: doublet beam expander lens 1; DL2: doublet beam expander lens 2; OBJ: objective lens; SMP: sample being imaged; POL: walk-off polarizer; MR: miniature reflector; EF: emission filter; PD: photo-detector; CPU: central processing unit; FG: function generator; HVA: high-voltage amplifier.

the distal-end optical system. The core of the second PM fiber is 4.0 μm in diameter; therefore the exit aperture of the second PM fiber serves as the confocal pinhole in our system by virtue of its small size. The still linearly-polarized light diverging from the fiber is collimated into a quarter-wave plate QWP by a miniature 5 mm effective focal length (EFL) aspheric lens to a diameter of 1 mm, matching the size of the micromirror scanner in our system. The QWP (Red Optronics, Inc., 0.1”×0.1” Zero-Order MicroWaveplate) converts the light linearly polarized along the slow axis of the PM fiber into circularly polarized light, as shown in the inset in Figure 3.1. The circularly polarized light is deflected of the folding mirror onto the micromirror scanner in a folded optical path, for compactness. The micromirror scanner is positioned at the back focal plane of a doublet lens DL1 (Thorlabs, Inc., AC050-008-A1) and deflects the beam across its entrance aperture in raster fashion. The doublet lens DL1 is part of an afocal Keplerian beam expander system, acting in conjunction with doublet lens DL2 (Thorlabs, Inc., AC127-025-A1-ML). The doublet lens DL1 converts the angular deflection created by the micromirror scanner into linear deflection of the focused spot in the intermediate focal plane. The position of the back focal plane of doublet lens DL2 is adjusted to match this intermediate focal plane. Doublet lens DL2 reconverts the linear scan into angular scan about a pivot point located at the point on the optical axis intersecting with the front focal plane of DL2. In effect, the beam expander increases the full-width half maximum (FWHM) diameter of the laser beam by a factor of about 3× in order to almost fill the back aperture of the objective lens OBJ, thereby maximizing the object-space numerical aperture (NA) of the distal optical system. In addition to increasing the object-space NA, the beam expander also translates the real pivot point, i.e., the micromirror scanner, to a virtual pivot point located at the back focal plane of the objective lens OBJ. This action results in the objective lens OBJ (Thorlabs, Inc., 350390-B, Ø4 mm, 2.75 mm EFL, 0.68 NA) converting the angular scan about the virtual pivot point into a linear scan across the sample. It is to be noted that the range of angular scan about the virtual pivot point is reduced by a factor equal to the beam expansion ratio of the Keplerian beam expander, i.e., the effective optical deflection angle about the virtual pivot point is 1/3× that of the total optical deflection angle produced by the micromirror scanner.

The focused and scanned spot on the sample induces direct backscatter due to native spatially-varying refractive index contrast present in the sample, or induces emission (enhanced reflective backscatter) from fluorophores (reflective contrast agents) selectively tagged to tumor biomarkers at the imaging site. The reflective backscatter is known to maintain its original circularly polarized state while the fluorescence emission has components of all polarization states. The polarization-maintaining property of reflective backscatter is exploited to improve the signal-to-noise ratio in reflection confocal imaging mode [89, 90]. The backscattered light retraces its path through the distal optical system and the QWP. At this point, the circularly polarized reflective backscatter is converted linearly polarized light, this time however, aligned along the fast axis of the PM fibers. Any spurious reflection from a part of the optical system prior to the QWP is therefore easily distinguished from the signal we wish to detect from the sample by analyzing its polarization. The QWP has no significant effect on fluorescent emission from the sample. The reconverted light is coupled into the PM fiber through the CL lens that acts as a focuser. Only light backscattered (or created, in the case of fluorescence) from the sample plane that was confocal with the aperture of the PM fiber enters into the fiber, and out-of-focus light is rejected at the PM fiber entrance, yielding confocal action. The spatially filtered light propagates through the PM fiber and into the proximal end of the system, where it is collimated by the lens CL into the polarizer POL. The polarizer separates the polarization aligned along the fast and slow axes of the fiber. The slow axis polarization is rejected, while the fast axis light is reflected off a miniature reflector into an emission filter. For reflectance imaging, the emission filter is removed, while in fluorescence imaging, the emission filter eliminates the laser line and allows any sample fluorescence to enter into the photodetector (New Focus, Inc., Model 2051-FS).

The circuitry that drives the micromirror scanner and synchronized data collection is controlled by a central processing unit (CPU). The CPU controls the amplitude and phase of the 2-channel function generator FG (Tektronix, Inc., AFG3022B), which outputs two drive signals corresponding to two-axis scanning and their associated trigger pulses in synchrony. The voltages of the drive signals output by the FG are amplified by a factor of 50× by a high-voltage amplifier HVA (TEGAM, Inc., Model 2350) before being supplied to the micromirror scanner. The first drive signal operates at the resonant frequency of the inner axis of the micromirror scanner to create fast line scans, while the second signal varies slowly at the frame rate required for imaging. The pulses trigger the recording of samples from the photodetector by the data acquisition board (National Instruments, Inc., NI PCI-6111). Data samples are acquired only during the forward line and frame traces of the micromirror, while image processing is performed in real time during the acquisition idle time in the retrace scanning segment. All data acquisition, signal processing, and image rendering is performed in a Matlab® graphical user interface program loaded in the CPU.

3.3 Performance Analysis

Careful design of the optical system is required to ensure that diffraction-limited performance is obtained from the optical elements, and that the sub-cellular lateral resolution and single-cell-layer optical sectioning comparable to histology, required for morphological feature identification and tumor biomarker overexpression analysis, is obtained from our system. We obtain the prescription data regarding our objective system (DL1-Dl2-OBJ) from ZEMAX® optical design simulations, and use the parameters obtained from them to verify, through calculations outlined in Refs [91, 92], that the confocal action of our single-mode fiber-based instrumentation provides the necessary lateral spatial resolution and out-of-focus light rejection. The simulations also provide insight into the off-axis performance of the optical system, comparisons between actual performance against the diffraction-limited maximum obtained in the absence of Seidel aberrations, a prediction for the total angular deflection required from the micromirror scanner in order to obtain the lateral field of view of 200 µm × 200 µm desired from the system, and a projection of the distortions present in the field of view.

3.3.1 Objective system: ZEMAX® optical simulations

Figure 3.2 presents the schematic of the layout of the distal-scanning objective system simulated in ZEMAX® optical design software. The simulated system [Figure 3.2(a)] consists of the two-axis micromirror scanner, the afocal Keplerian beam expander (comprising lenses DL1 and DL2), and the high-NA objective lens OBJ. For a total micromirror scanner optical deflection angle of 13°, the field of view is approximately 192 µm × 192 µm, as shown in Figure 3.2(b). The angular deflection of the micromirror

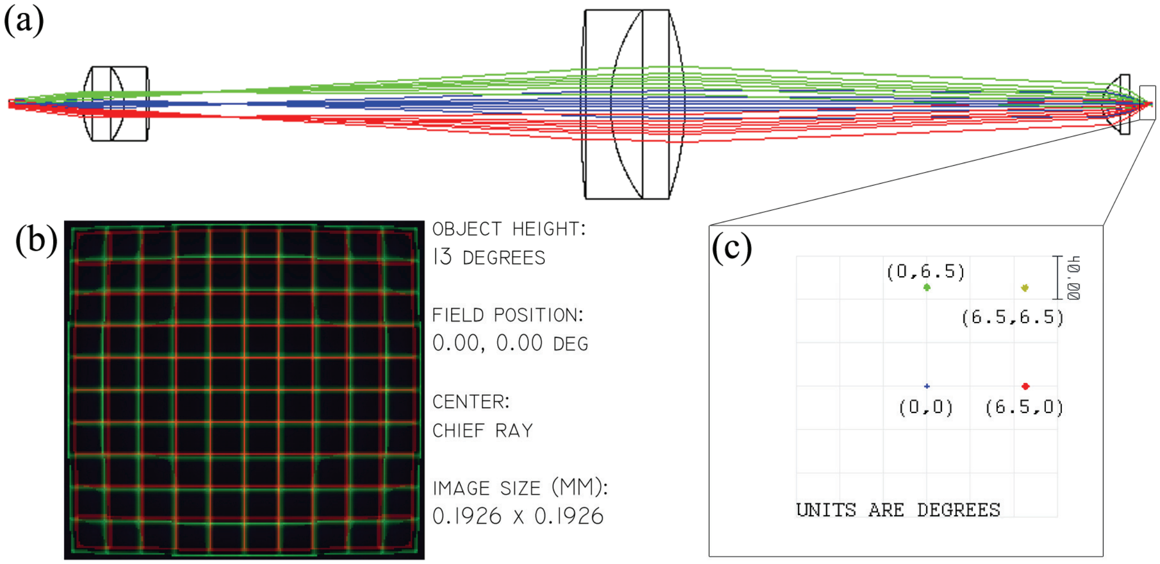

Figure 3.2: Schematic of the optical layout of the distal scanning objective system simulated in ZEMAX® optical design software. (a) 3D layout of the micromirror scanner, afocal Keplerian beam expander (DL1-DL2), and high NA objective lens (OBJ). (b) Simulated lateral field of view for total micromirror optical deflection angle of 13°. (c) Location of four points within the field of view where optical performance is characterized.

scanner is not translated into the lateral field of view with perfect linearity; the slight distortions in the lateral field of view are visible in Figure 3.2(b). Detailed characterization of the system optical properties is performed for the four points within the lateral field of view indicated in Figure 3.2(c); the results obtained at these four points are expected to be indicative of the performance over the entire field of view.

The first set of simulations is focused on the lateral resolution characteristics of the system. Performance in this dimension is assessed by studying the spot sizes and patterns within the field of view in the sample focal plane, the modulation transfer

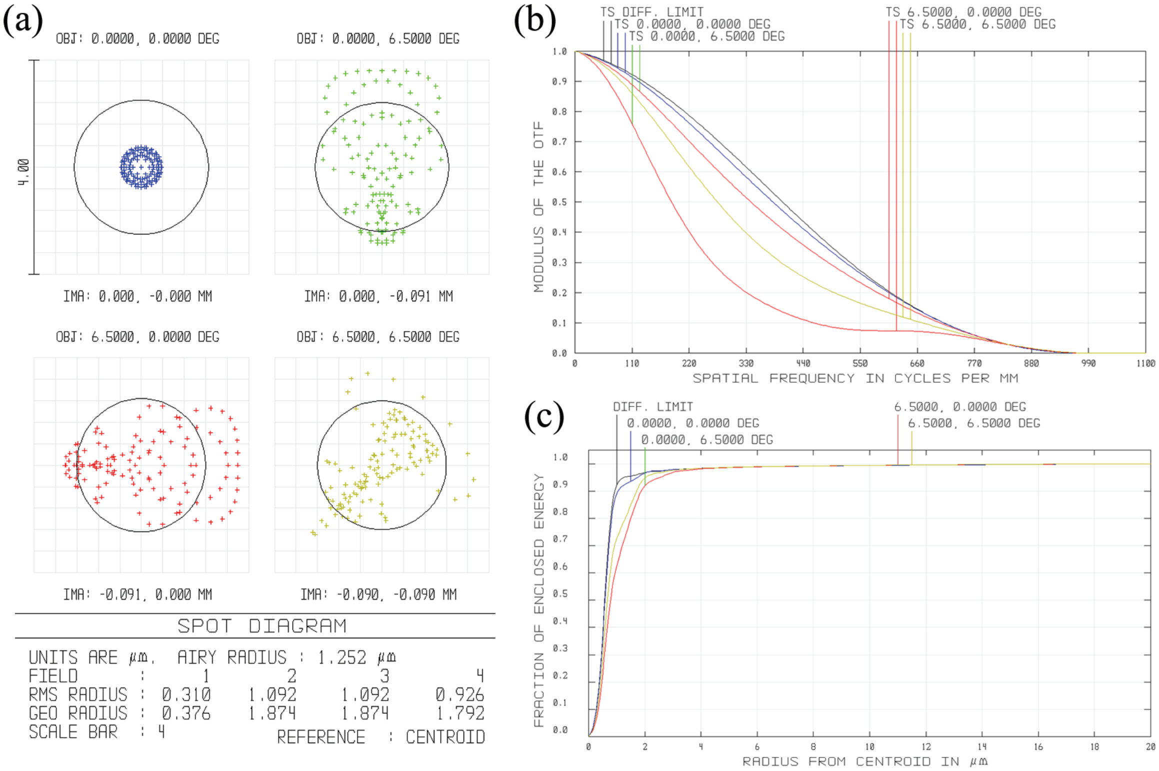

UNITS ARE µm. AIRY RADIUS : 1.252 µm

FIELD :	1	2	3	4
RMS RADIUS :	0.310	1.092	1.092	0.926
GEO RADIUS :	0.376	1.874	1.874	1.792

SCALE BAR : 4

REFERENCE : CENTROID

Figure 3.3: Simulated lateral resolution characteristics of the distal-scanning objective system. (a) Spot diagram showing ray pattern and focal spot sizes in comparison with the airy disk radius. (b) Modulation transfer functions (MTFs) compared with diffraction-limited MTF. (c) Diagram of percentage encircled energy versus radial distance from centroid.

functions at different spot locations compared against diffraction-limited performance, and the encircled energy as a function of spot size. The results of the lateral resolution simulations are presented in Figure 3.3. As evidenced from Figure 3.3(a), the spot rays for all four tested locations lie within the airy disk radius, indicating that diffraction-limited performance is obtained over the entire desired field of view. Minimum spot size of 0.31 μm is obtained at the center of the field of view, while the resolution degrades to 1.092 μm at the ends of the field of view. The degree to which the system exhibits diffraction-limited performance is also often assessed by studying the modulation transfer function (MTF) for the system. Figure 3.3(b) plots the MTF (including tangential and sagittal response) for the four locations and compares them against the diffraction-limited curve. The plots indicate that at the center of the view field, the performance is virtually indistinguishable from the ideal case, while there is a small drop in performance moving towards the edges of the field of view. A similar trend is observed when monitoring Figure 3.3(c), a plot of the percentage of total energy enclosed in the beam as a function of the distance from the centroid of the beam spot.

The second set of simulations study the axial resolution characteristics of the system. Axial performance is assessed by monitoring the spot ray diagram as the beam propagates axially through the focal plane at the four locations being tested, and by measuring the Rayleigh range of the beam. Figure 3.4 presents the through-focus spot diagrams for the four tested locations and the axial resolution (defined here as twice the Rayleigh range) for the beam propagating axially through the center of the field of view. The through-focus spot diagrams [Figure 3.4(a)] show that the shape and extents of the spot changes quickly through even a small defocus of only 5 μm. This qualitatively indicates that the axial resolution is on the order of a few micrometers over the entire field of view. The performance is also expected to be best at the center of the field of

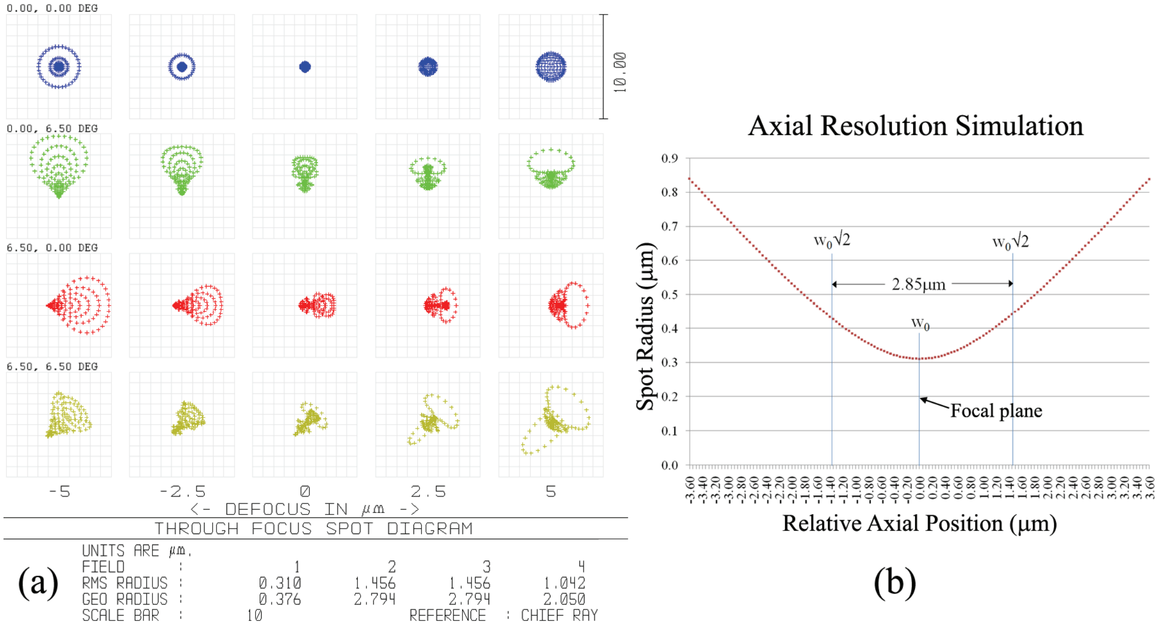

Figure 3.4: Simulated axial resolution characteristics of the distal scanning-objective system. (a) Through-focus spot diagrams at the four tested locations in the field of view. (b) Plot of beam waist radius as a function of axial position relative to the focal plane measured at the center of the field of view.

view where the beam maintains approximately a Gaussian shape as it propagates through the sample focal plane. Figure 3.4(b) shows a detailed plot of the spot size of the beam as is propagates through axial the focal plane at the center of the field of view. The Rayleigh range is calculated as the distance between the z-position of smallest beam waist (ω_0) to the z-position at which the waist reaches size ($\omega_0\sqrt{2}$). The axial resolution is defined here as twice the Rayleigh range, and is determined to be 2.85 µm in our case.

3.3.2 Theoretical resolution calculations

The resolution of the confocal system is not only dependent on the numerical aperture of the objective system, but also on the size of the confocal pinhole [92]. The lateral and axial resolution of the system can be calculated from the theory outlined in Refs [70, 91, 92]. If the single-mode fiber we employ as the confocal pinhole has a radius

ρ, core and cladding indices of n_1 and n_2, and operates at wavelength λ, the fiber parameter V is defined as –

$$V = \frac{2\pi}{\lambda}\rho\sqrt{n_2^2 - n_1^2} \tag{3.1}$$

The fiber spot radius that provides confocal action is then defined as –

$$r_0 = \frac{\rho}{\sqrt{2\ln(V)}} \tag{3.2}$$

The pinhole radius normalized in terms of the optical coordinates (wavelength) in the image space is given by equation (3.3) –

$$v_p = \frac{2\pi}{\lambda} r_0 (n \sin\alpha)_{fiber} \tag{3.3}$$

Ref. [92] provides a plot of the full width half maximum lateral resolution $v_{1/2}$ as a function of the normalized pinhole radius, which we provide here for easy reference.

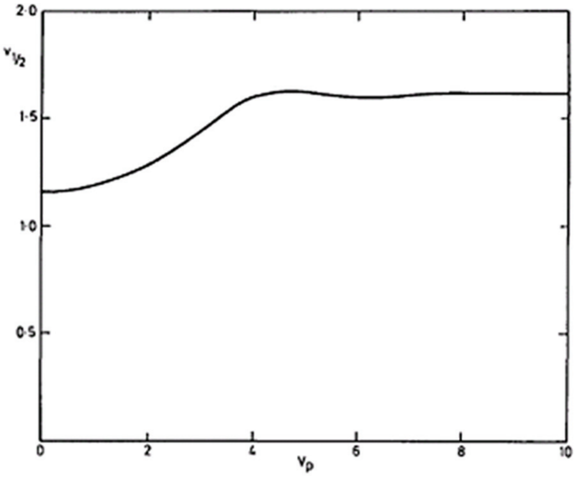

Figure 3.5: Normalized full width half-maximum lateral resolution as a function of the normalized pinhole radius (adapted from Ref. [92]).

The lateral resolution can then be converted into standard measurement units using equation (3.4) –

$$r_{FWHM} = \frac{v_{1/2}\lambda}{2\pi(n\sin\alpha)_{objective}} \tag{3.4}$$

For our system operating at 635 nm wavelength (λ), using a core radius ρ of 4.0 µm, core and cladding indices of 1.445 (n_1) and 1.440 (n_2) respectively, we obtain a fiber parameter V of 2.3768, and a fiber spot radius r_0, considering only the first mode, of 1.52 µm. For fiber NA of 0.11, the normalized pinhole radius v_p is calculated as 1.6543. Referring to Figure 3.5, the normalized full-width half maximum lateral resolution is determined to be 1.237. Using equation (3.4) and using the objective NA as 0.47 (based on the ZEMAX® simulations), the lateral resolution is calculated as 0.27 µm, as compared to the 0.31 µm value obtained from the simulations. This implies that, though the numbers match each other quite well, the pinhole created by the PM fiber is slightly smaller than the diameter of the first minimum of the point spread function created in the image space by a point source in the object space projected through the objective optics.

The axial resolution is calculated by a method described in Ref. [91]. The normalized detector intensity profile is given in terms of the normalized pinhole radius v_p by equation (3.5) –

$$I(u) = \left| \frac{v_p^2\left(1 - e^{-\left(v_p^2 - iu\right)}\right)}{\left(1 - e^{-v_p^2}\right)\left(v_p^2 - iu\right)} \right|^2 \tag{3.5}$$

Here u is the normalized unit of distance along the central optic axis (z-direction). The graph corresponding to equation (3.5) is plotted in Figure 3.6. From the figure, the value of u at which the intensity falls to half of its maximum value ($u_{1/2}$) is 3.41. The axial resolution is then calculated using equation (3.6) as –

$$z_{FWHM} = \frac{u_{1/2}\lambda}{4\left(n\sin^2\alpha\right)_{objective}} \tag{3.6}$$

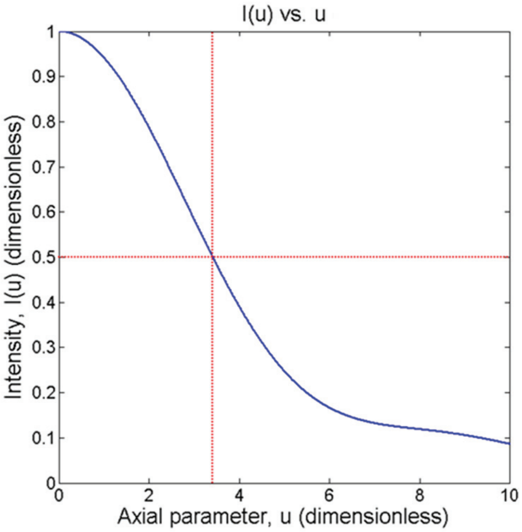

Figure 3.6: Plot of the normalized detector intensity profile *I(u)* as a function of normalized axial distance *u*.

Using the NA for our objective of 0.47 as before and 635 nm operating wavelength, we find the axial resolution to be 2.85 μm, which perfectly matches our ZEMAX® simulation results described earlier. This is expected in contrast to the slight difference obtained in the lateral resolution calculations as the axial characteristic is less dependent on pinhole size than the lateral resolution in this regime. The simulations and calculations show that we can expect to achieve sub-micrometer lateral resolution and single cell layer optical sectioning with the instrument, with slowly degrading performance on moving towards the edges of the field of view.

3.4 Handheld Instrumentation

The achievement of cellular-scale biopsy-free optical sectioning in a compact and versatile miniature probe would facilitate its application in surgical operating theaters and in *in-vivo* biomedical diagnostics and clinical studies. The incorporation of inexpensive batch-fabricated components in the distal system is also strongly motivated by the clinical considerations for a probe that can eventually be made disposable after one-time use. Here we describe the materials and methods employed to create our handheld confocal imaging instrumentation, and the impact that these design choices had on the measured optical performance characteristics of the system.

3.4.1 Materials and methods

We have developed a cost-effective MEMS mounting package fabricated by laser stereolithography rapid prototyping (manufactured by eMachineShop.com, Mahwah, NJ) using an acrylonitrile-butadiene-styrene (ABS) composite plastic to combine the micromirror scanner with the other optical components in a compact forward-imaging probe. The mechanical drawings for the MEMS mounting package and a photograph of our micromirror scanner mounted in a package are presented in Figure 3.7. The

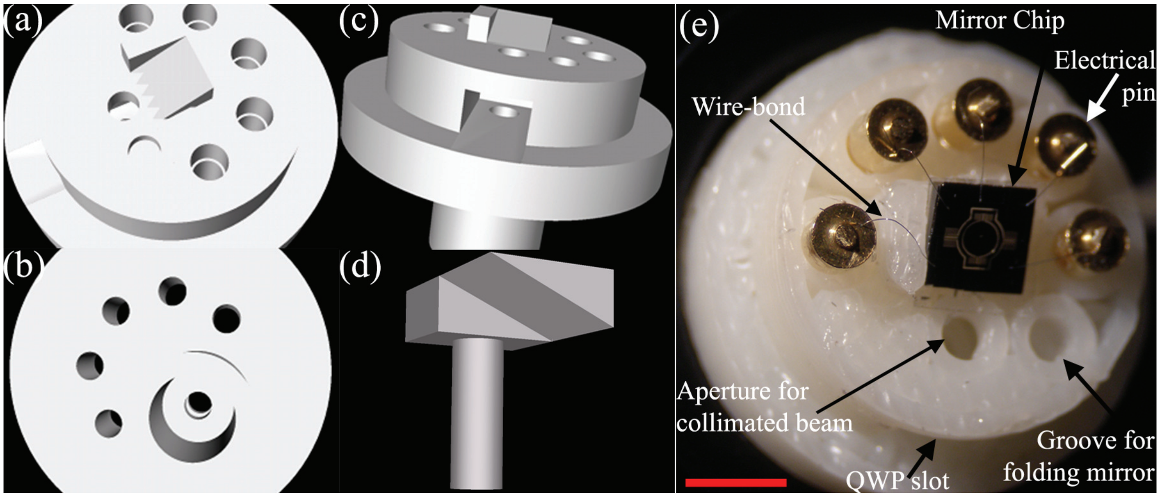

Figure 3.7: Illustrations of the design of the MEMS mounting package incorporated into the handheld confocal imaging instrument. (a-d) Mechanical drawings of the MEMS mount. (a) Top view. (b) Bottom view. (c) Oblique view. (d) Folding mirror (separate piece). (e) Photograph of the fabricated mount with a micromirror scanner packaged in it.

micromirror is placed on a 22° inclined surface [Figure 3.7(a)] to facilitate the creation of a folded forward-imaging optical path. The mount has a hollow tube of 4mm inner diameter on the back side [Figure 3.7(b)] to secure PM fiber acting as confocal pinhole along with the 5mm EFL aspheric collimating lens. The collimated beam passes through the QWP which can be introduced into a slot from the side of the package [Figure 3.7(c)]. The folding mirror and its associated stand are monolithically fabricated as a separate piece [Figure 3.7(d)], which can then be mounted into the slot provided on the front face of the mount. Finally, five vias are provided on the front surface to insert five electrical gold pins to power the micromirror scanner. Electrical connections are created by wire-bonding commonly used in the consumer electronics industry. The outer circumference of the package is threaded such that the objective lens (assembled separately) can be attached to the MEMS package, and its position adjusted to ensure that the reflective surface of the micromirror scanner coincides with the back focal plane of the first doublet lens DL1 of the Keplerian beam expander within the objective system. Figure 3.7(e) shows an optical photomicrograph of the fabricated mount with one of our micromirror scanners packaged in it.

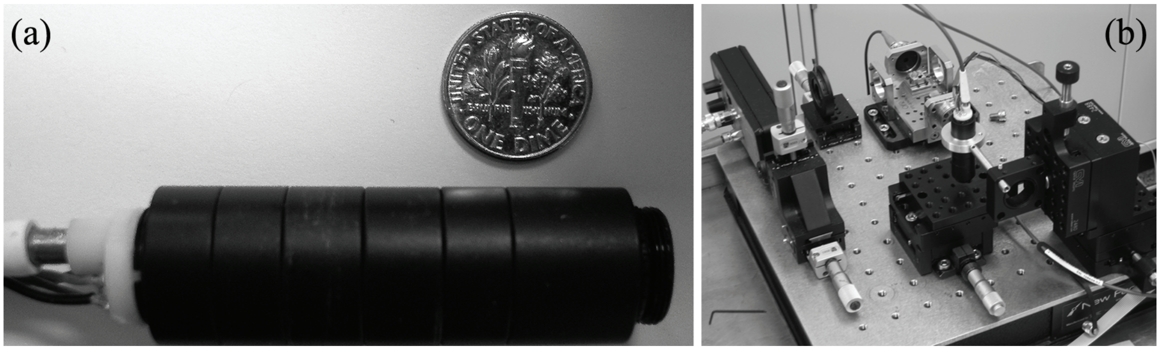

Figure 3.8: Photographs of the final assembled handheld probe and proximal instrumentation for the laser-scanning confocal microscope. (a) Fully assembled handheld probe. (b) Proximal instrumentation setup on a portable optical breadboard.

Our objective system is assembled from standard ½” tube lens optics (Thorlabs, Inc.). Attaching the objective module to the MEMS package with compatible threading completes the assembly of the final handheld system. Photographs of the assembled handheld probe and the proximal instrumentation are depicted in Figure 3.8. The objective working distance of the assembled probe is 1.56 mm, sufficient for the imaging depths required in most confocal imaging applications.

3.4.2 Image acquisition and processing

The trigger pulses from the FG are used t control the image acquisition. The resonant frequency of the inner axis of the micromirror scanner is tested beforehand, and the frequency of the sinusoidal output of the first channel of the FG is matched to it. Based on the field of view and resolution, an estimate for the minimum number of sampled points per line is calculated; based on this and the line scan rate (i.e., the inner axis resonant frequency), the sampling frequency of the NI PCI-6111 data acquisition (DAQ) board is set above the minimum Nyquist criterion. Also, based on the line scan rate, resolution and the field of view, the total number of lines to be scanned is also determined to satisfy the Nyquist criteria for spatial sampling. On receiving a trigger pulse, the DAQ board acquires samples during the forward trace of the line scan, and not during the retrace. This process is repeated until all the lines in the frame are acquired.

During the micromirror frame retrace, samples are not acquired and the acquired image is processed to improve image quality. The edges of the image are usually stretched due to the sinusoidal nature of the scan, and are cropped. High-frequency noise in the image is removed by 2D low-pass filtering (done by performing 2D Fast Fourier Transform, or FFT to transform to the spatial frequency domain, multiplying by a 2D matrix consisting of ones and zeros representing a circle function [93] and performing 2D inverse FFT to move back to the spatial domain). This is followed by image histogram equalization to utilize the entire dynamic range of the intensities available, and false coloring if operating in fluorescence mode. The instrumentation has the ability to stitch four fields of view together if the sample can be scanned on a movable stage. If image stitching is performed, the final brightness and contrast of the image are adjusted before saving the image data. All image processing is performed via a Matlab® graphical user interface program.

3.4.3 System performance characterization

The system resolution is experimentally determined by recording photodetector intensity against position while translating a mirror axially through the sample focal plane and a knife edge laterally in the focal plane across the beam spot. The lateral and axial resolutions are deduced from the measurement curves [Figure 3.9(a-b)] using the method described in Ref. [94] to be 0.49 μm and 4.18 μm respectively. These numbers are degraded somewhat from the values derived from the optical simulations and theoretical calculations, but nevertheless indicate that single cell layer optical sectioning is achieved

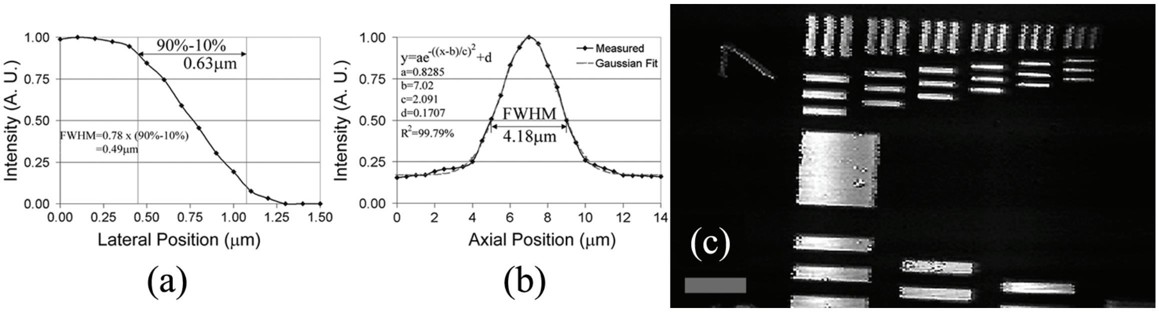

(a) (b)

Figure 3.9: Experimental measurement of the optical performance of the handheld laser-scanning confocal microscope. (a) Lateral resolution measurement. (b) Axial resolution measurement. (c) Image of the elements of group 7 of a USAF 1951 standard resolution target. Field of view: 200 μm × 125 μm. Scale bar: 25 μm.

in confocal imaging with this instrument. Misalignment along the axial direction between two or more of the optical elements in the handheld probe is the likely source of this degradation in resolution. Figure 3.9(c) presents an image (with 200 µm × 125 µm field of view) of the elements of group 7 of a standard USAF 1951 resolution target acquired using the instrument at 3.0 frames per second. The smallest elements in the image are 2.2 µm wide and spaced 2.2 µm apart. The edges of these lines are quite sharp, indicating qualitatively that sub-micrometer lateral resolution is obtained over the entire field.

3.5 Conclusions

We have demonstrated a handheld laser-scanning confocal microscopy probe incorporating a high-reflectivity two-axis scanning micromirror. ZEMAX optical design simulations and theoretical calculations indicated that single cell layer optical sectioning and sub-micrometer lateral resolution imaging can be expected from the instrument. We fabricated the handheld probe according to these design specifications incorporating batch-fabricated rapid prototyped components for MEMS packaging, providing a first step to creating disposable one-time-use probes. Further improvements in disposability can be achieved by using injection molded plastic objective lenses [95] and rapid prototyped objective lens packaging systems. Experimental measurements indicate that the sub-micrometer resolution and single cell layer axial optical sectioning are achieved using the probe. These results indicate portable handheld optical microscopy tools based on silicon micromirror technologies could be important in interventional imaging, complementing existing coarse-resolution techniques to improve the efficacy of disease diagnosis, image-guided excisional microsurgery, and monitored photodynamic therapy.

CHAPTER 4

IMAGING EXPERIMENTS

We attempt to verify the ability of our micromirror-based handheld laser-scanning confocal microscope to detect, via reflectance or fluorescence imaging, histologically relevant features in tissue samples to validate the hypothesis that such handheld systems can eventually complement existing low-resolution imaging methods in clinical breast cancer management. Towards this specific aim, we present the results achieved in two separate sets of imaging experiments. We present the expression maps for two biomarkers of breast cancer in human epithelial breast tissue slices obtained from metastatic breast cancer patients, prepared to mimic fluorescently-labeled sub-surface tissue. In the second set of experiments, we leverage the reflectance confocal imaging capabilities of our instrument to determine the morphological characteristics of swine liver at different depths from the surface. The considerations that led us to choose the specific imaging modalities in each case and the biomarkers tracked are outlined, followed by a discussion of the results and their implications.

4.1 Fluorescence Microscopy: Human Epithelial Breast Tissue

4.1.1 Imaging considerations

The monitoring of breast cancer can be achieved by following either the morphological or physiological changes that accompany the condition, or both, as previously discussed in the introduction to this dissertation. The morphological variations can be studied either by tracking the local spatial variations in refractive index (by reflectance imaging), or by studying the expression of specific biomarkers within the cell boundaries (via fluorescence imaging). The study of the overexpression by fluorescence, in addition to providing useful information on cytomorphology, can provide far more powerful detail on the tumor progression and insight into treatment strategies; therefore this is the more reasonable method to approach the problem of breast cancer imaging. A final point to make in favor of fluorescence imaging is that in our experiments on reflectance confocal microscopy of the breast tissue, we found that the spatial variations in local refractive index of the tissue were small, leading to low contrast in the images obtained by our instrument and a standard Olympus BX 51 bright-field microscope, as compared to when there was staining such as hematoxylin/eosin (H/E) (Figure 4.1). The adipocytes (fat cells) are clearly distinguishable in the images, but it is difficult to resolve other individual nuclei clearly, unlike in the H/E stained samples.

In spite of the many advantages that fluorescence confocal imaging can provide in

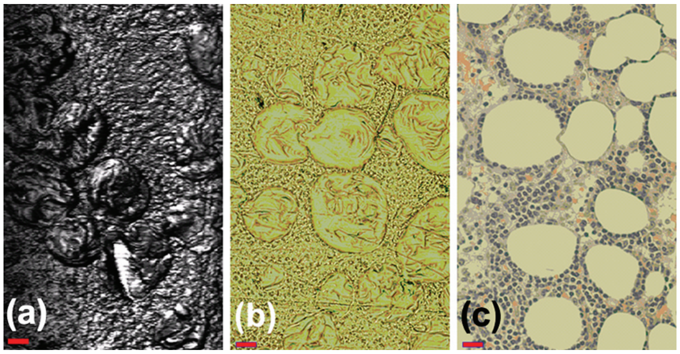

Figure 4.1: Reflectance confocal microscope imaging of human epithelial breast tissue using the handheld instrument. (a) Image acquired using the MEMS handheld instrument (four fields stitched). (b) Comparison image from Olympus BX51 microscope (bright-field, 20× objective). (c) Image of an adjacent microtome slice of the tissue with H/E staining, using the Olympus BX51 microscope (bright-field, 20×). Field of view of each unstitched image is 200 μm × 125 μm. Scale bar: 25 μm.

breast cancer management, the lack of established targeted *in vivo* contrast agents that can be used in humans represents an impediment to the immediate use of the instrument for breast cancer imaging. Several investigative efforts [64, 65, 96-99] have focused on development of suitable novel contrast agents and delivery platforms; this research running in parallel and complementary to our efforts, when combined, can result in innovative disruptive technologies for breast cancer research.

4.1.2 Biomarker selection

The choice of tumor biomarkers is important to obtain the maximum amount of actionable intelligence on the tumor. The choice is affected by the percentage incidence and specificity of the biomarkers to the tumor site, and also the qualitative information it can provide on the treatment strategies. We considered the use of several biomarkers of human breast cancers, listed in Table 4.1 [100].

Table 4.1: Biomarkers evaluated for use in breast cancer imaging experiments with the handheld laser-scanning fluorescence confocal microscope

No.	Biomarker	Localization	Notes
1	Cytokeratin	Cytoplasm	Defines subtypes of breast cancer [101]
2	Estrogen	Nuclear	Important in breast cancer treatment [9]
3	Progesterone	Nuclear	Important in breast cancer treatment [9]
4	EGFR (Her-1)	Surface	Diagnosis of many epithelial precancers [102]
5	Her-2	Cytoplasm	Organ specific, aggressive breast cancers [103]
6	Ki67	Nuclear	Proliferation marker [104]
7	ALDH-1	Cytoplasm	Marker of malignant mammary stem cells [105]
8	Bcl-2	Cytoplasm	Mediates apoptotic behavior [11]
9	EpCAM	Cytoplasm	Diagnosis of many epithelial precancers [9]
10	Mammaglobin	Surface	Highly organ specific [106]

Our instrument is capable of acquiring images by resolving the excitation of two fluorophores, AF-633 and AF-647. Since we were limited to two biomarkers, we chose cytokeratin and mammaglobin from the list in Table 4.1. The two were chosen because they stained different regions of the cells, they have high incidences as markers in breast cancer, they are specific to tumors (cytokeratin) and breast tumors (mammaglobin), and therefore are useful in obtaining information regarding breast tumors [101, 106-110].

4.1.3 Experimentation Procedure

Imaging experiments were conducted at the University of Texas Southwestern Medical Center at Dallas. All patients were enrolled using protocols (#092004-010) approved by the Institutional Review Board at UT Southwestern, and provided informed consent. On receipt, the samples were fixed in ice-cold acetone for 10 minutes, and rinsed in a mixture of phosphate buffer saline (PBS) and 0.1% Tween-20. The samples were then immersed in blocking buffer [PBS + 0.1% Tween-20 + 1% Bovine Serum Albumin (BSA)] and incubated for 30 minutes at 37°C. After incubation, the samples were rinsed in PBS, blotted dry. The samples were stained with the fluorescent contrast agents conjugated to appropriate antibodies and incubated for 40 minutes at 37°C. After rinsing with PBS + 0.1% Tween-20, the samples were dried, and mounting medium was added. The samples were covered with a 100 μm thick layer of polydimethylsiloxane (PDMS) infused with titanium dioxide that approximates the optical scattering properties of tissue [111]. The final prepared samples mimic the staining of a sub-surface (100 μm depth) layer of breast tissue with fluorescent contrast agents for imaging with the handheld microscope.

The prepared samples were first imaged under a bench-top Leica SP2 AOBS confocal microscope using a dry 0.7NA, 20× objective using 632.8 nm He-Ne laser excitation wavelength and emission filter spectra matched to the fluorophore emissions. Expression maps of the entire tissue sample were obtained from the bench-top instrument as controls for imaging with our handheld instrument. Image processing for image histogram equalization and encoding the fluorophores into color channels of the 8-bit images was performed during the imaging procedure in the proprietary software bundled with the Leica instrument. The samples were next imaged with our handheld instrument. Four fields of view were stitched together to form an image of size approximately 400 µm × 250 µm with the two fluorophores encoded into the green and red channels of the 8-bit composite color images. Image processing, including high-frequency noise removal, image histogram equalization, image rotation and resampling to match the orientation of the control images, was performed in a Matlab® programming environment.

4.1.4 Imaging results

The results of imaging six specimens obtained from metastatic breast cancer patients are presented in Figure 4.2. The expression of cytokeratin and mammaglobin are depicted in sub-figures (a) and (b) respectively, while the combined overlaid control images of the expression levels, obtained from the Leica bench-top confocal microscope are presented in sub-figures (c) of each image data set. The images obtained from the MEMS handheld instrument consist of four fields of view stitched together to form a composite image spanning 400 µm × 250 µm. The control images from the Leica confocal microscope span a field of view of 750 µm × 750 µm, and contain the same 400 µm × 250 µm region of the sample imaged by the MEMS handheld instrument within them; however, the orientation and position of that region within the field of view varies between the images. The scale bar in each image data set represents 100 µm in the control (c) images, and 33 µm in the MEMS handheld instrument images (a-b).

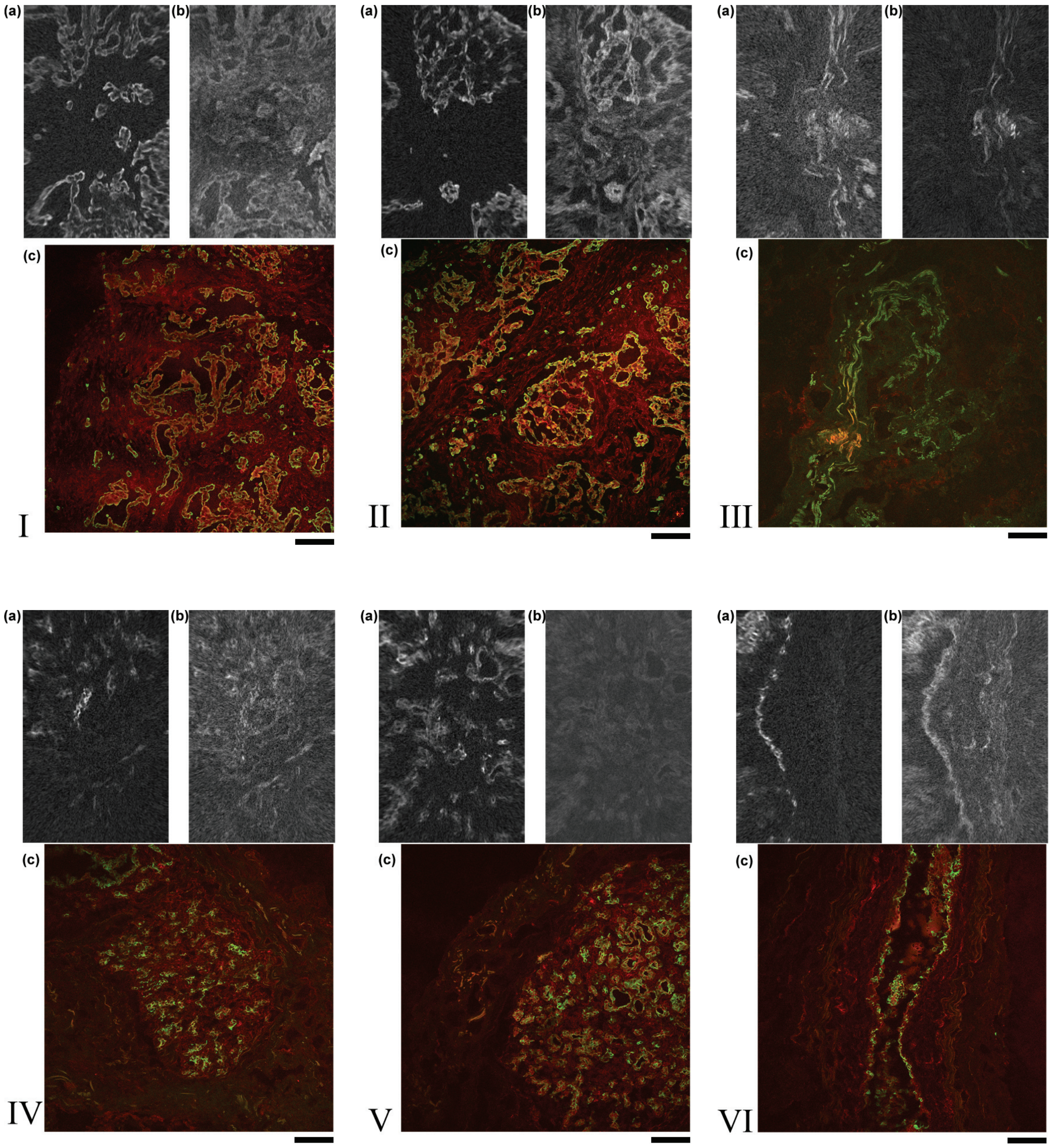

Figure 4.2: Results of imaging human epithelial breast tissue from metastatic breast cancer patients using the handheld laser-scanning confocal microscope. (I-VI) Image data sets from each of the six patients enrolled in the study. Images I-VI (a) present cytokeratin expression and I-VI (b) present mammaglobin expression. I-VI (c) are control images obtained using Leica confocal microscope with 20× 0.7NA dry objective. Field of view for I-VI (a-b): 400 μm × 250 μm (4 fields stitched); I-VI (c): 750 μm × 750 μm. Scale bar is 100 μm for I-VI(c), and 33 μm for I-VI (a-b).

4.1.5 Discussion

The comparison of the imaging results from the MEMS handheld instrument and the control images from the bench-top confocal microscope reveals potential for our laser-scanning microscope to provide expression maps of biomarkers that can indicate the presence, and state of tumor conditions. The features of cytokeratin expression are much more clearly seen in the images than mammaglobin expression, which exhibits significant background in the images. This can result due to a number of factors, including nonspecific binding, relative concentrations of the fluorophores, and imaging capture (exposure) times. The images from the handheld instrument are not perfectly oriented with the control images due to the lack of alignment of registration marks in the sample. Some high-frequency noise and distortion in the images from the handheld system are visible on closer inspection. Also noticeable is significant overlap of some of the features expressed in the cytokeratin maps into the maps of mammaglobin expression. This is due to the overlap of emission from the fluorophore used to map cytokeratin into the emission spectrum of the second fluorophore used to map mammaglobin expression. Improvements in the spectral discrimination, through use of multiple laser excitation sources, narrower filter spectral transmission characteristics (at the cost of reduced emission being collected at the photodetector), or narrow-band emitting quantum dot fluorophores is suggested to mitigate or eliminate this problem.

Histopathology has conventionally relied upon the use of hematoxylin-eosin (H/E) stained samples to perform morphological analysis to make a determination regarding the patient. In attempting to interpret the exact physiological significance of the fluorescence images and associated patient prognosis with the help of a pathologist from the University of Texas Southwestern Medical Center, it became clear that the morphology of the fluorescently-labeled tissue slides differs vastly from that of the H/E stained slides. Upon inspection of adjacent unstained microtome slides for the same features, it appeared that the morphological features in it more closely matched the features on the fluorescently-labeled slides than the associated H/E stained slides. We concluded that the H/E stain significantly alters the appearance of the sample. The thickness of the microtome slides (6 μm) may also have played a part in this comparison, as the structure of the tissue is expected to change over the several tens of micrometers in depth that the three slides cover. Fluorescence and H/E stained images from a much larger sample set of patients than undertaken in our study is required to progress further with regards to interpretation, as this involves a significant learning curve for the pathologist to understand and interpret the fluorescence images with the same accuracy and confidence as they have been trained to do over the years with H/E stained samples.

4.2 Reflectance Microscopy: *Ex Vivo* Swine Liver

4.2.1 Imaging considerations

Reflectance confocal microscopy can be extremely useful in situations where agents are not available for contrast enhancement in *in-vivo* imaging environments, and in situations where cytomorphological information can be sufficient for diagnostic purposes. Prior studies even suggest its usefulness in early breast cancer detection [71], in spite of the clear advantages, described earlier, of using fluorescent biomarkers. In order to demonstrate the capabilities of our instrument in such situations, we present here images of *ex vivo* swine liver obtained without any labeling using contrast agents acquired by our MEMS handheld laser-scanning confocal microscope in reflectance imaging mode.

4.2.2 Experimentation procedure

We conducted experiments at the University of Texas M. D. Anderson Cancer Center at Houston on *ex vivo* samples of swine liver to explore the applicability of our system in reflectance imaging mode to interventional imaging [84]. Samples were procured as part of a larger experiment being conducted on swine liver cirrhosis detection using imaging and spectroscopic methods. All animal experiments were approved by the institutional animal care and use committee at the University of Texas M. D. Anderson Cancer Center before the start of the study. *Ex vivo* samples were imaged directly under our instrument after excisional biopsy. After imaging, the samples were formalin-fixed before examination under a low-power digital microscope to identify gross tissue architecture.

4.2.3 Imaging results and discussion

Figure 4.3 presents images of normal *ex vivo* swine liver obtained at different imaging depths of the tissue without the use of fixing or contrast agents. Each image consists of four fields of view stitched together to form a composite image of 400 μm × 250 μm size. The liver usually contains a protective capsular layer [Figure 4.3(a)] forming the outermost surface. The depth of this capsular region is typically 1-5 cell layers [Figure 4.3(b)], and serves no functional purpose besides physical protection. Beneath this capsular layer, the liver consists mainly of hepatocytes, depicted in Figure 4.3(c). The liver is also characterized by a high density of sinusoids, depicted as white lines in Figure 4.3(c), which are small capillaries that pervade throughout the organ. These sinusoids in the image acquired by the MEMS instrument correspond to the white lines in the image of the stained slide depicted in Figure 4.3(d). However, there is insufficient native contrast to visualize the hepatocyte nuclei in the MEMS images.

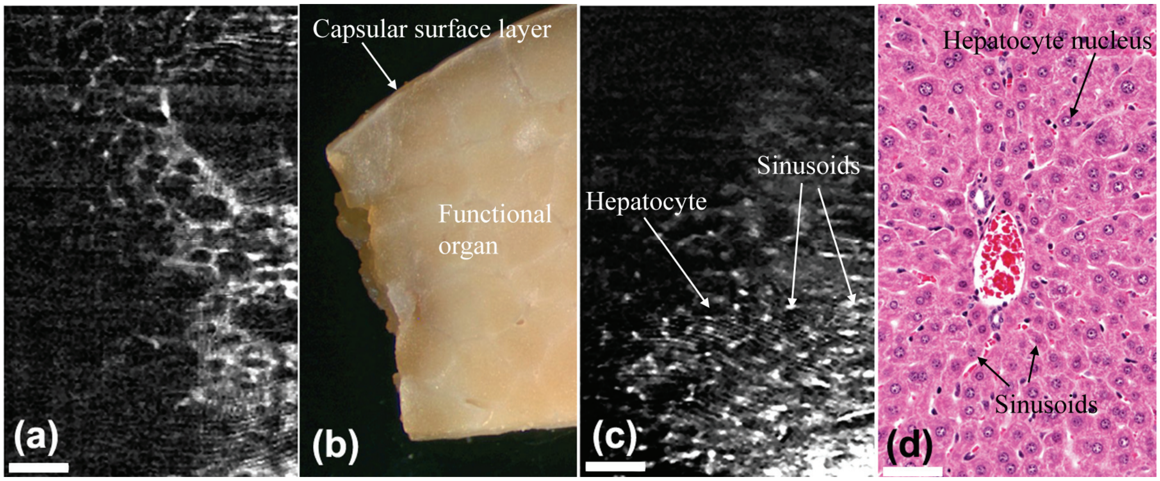

Figure 4.3: Results of experiments on *ex vivo* swine liver imaging using our MEMS handheld reflectance confocal microscope. (a) Image of the protective capsular layer (four fields stitched) using the MEMS instrument. (b) Photomicrograph of liver sample depicting the capsular layer in relation to the rest of the organ tissue. (c) Image of hepatocytes nuclei obtained by reflectance confocal microscopy using our handheld instrument. (d) Bright-field image using an Olympus BX51 20× microscope of a stained sample of swine liver tissue microtome slice. Scale bars: 50 μm.

4.3 Conclusions

The ability to detect histologically relevant features of breast carcinomas by high-resolution optical microscopy can prove to be a disruptive innovation that can significantly alter the technological and procedural landscape in image-guided intervention. Such tools can complement more conventional large-volume scanning systems to provide the physician with a comprehensive and detailed understanding of the physiology of the tissue. Laser-scanning confocal microscopy can reveal cytomorphological and physiological features of the tissue via reflectance and fluorescence confocal microscopies, respectively. We have demonstrated that a microelectromechanical handheld laser-scanning confocal microscope can serve this purpose. The design of the optical system provides sub-micrometer lateral resolution and single-cell-layer optical sectioning ability, similar to conventional histology. Using this instrument, expressions of two tumor biomarkers – cytokeratin and mammaglobin – are mapped in fluorescently-labeled tissue from metastatic breast cancer patients. Additionally, the reflectance confocal imaging capabilities of the instrument are demonstrated in imaging the hepatocytes nuclei in *ex vivo* swine liver samples, indicating that the instrument can be a potentially powerful tool in high-resolution precision image-guided intervention.

CHAPTER 5

MICROMIRROR-BASED IMAGING ENHANCEMENTS

The experiments described previously in this dissertation clearly affirm the utility of a portable, handheld, sub-cellular resolution laser-scanning confocal microscope towards early detection of epithelial breast cancer detection. The system is capable of providing 2D images of a single cell layer with sub-micron lateral resolution spanning a field of view of several hundred microns. The capabilities of such a microscope are well suited to studying the micro-scale morphology and tumor marker expression over a small optical section within the epithelium. However, in some circumstances, it may be useful to visualize, with slightly lowered resolution, a larger lateral field of tissue at depths in the millimeter range. Even more valuable would be the capability to visualize a three-dimensional volumetric image of the specimen to provide the physician with a better understanding of the morphology of the sample. Adapting the handheld microscope to endoscopic application through further miniaturization is another research thrust arousing significant interest that could revolutionize the field of image-guided intervention. Novel solutions heretofore unseen in the literature are required to enable forward-imaging at high resolution within internal non-tubular organs.

We have conceived and developed two separate imaging modalities that address these specific requirements, designed around the scanning micromirrors that form the core enabling technology. The first is a swept source optical coherence tomography system for high-speed 3D volumetric imaging of a $2 \times 1 \times 4$ mm^3 volume of turbid media. We demonstrate its capability of faster-than-video-rate 2D tomographic imaging and high-speed 3D volume mapping at over 10 million volume pixels per second *in vivo*. The second is a Fresnel zone plate monolithically integrated on the surface of the scanning micromirrors via patterning of optically reflective binary-phase modulation elements. The invention allows scanning and focusing functions to be integrated into the same device, thus obviating the need for multiple optical elements and eliminating cumbersome alignment. We envision that this device can contribute to significant size reduction of the probe, thus enabling fast-scanning forward-imaging endoscopic devices. We describe here a theoretical framework for designing the phase modulation elements, present simulations and experimental verification of device performance, and demonstrate reflectance imaging by incorporating it in our confocal system.

5.1 3D Imaging: Swept-Source Optical Coherence Tomography

Optical coherence tomography (OCT) has become a prominent imaging modality for minimally invasive *in vivo* optical biopsy and image-guided intervention studies [16, 112-116]. Invented in 1991 [117], OCT provides tomographic (i.e., cross-sectional) depth-resolved images of the sample, and may be considered the photonic equivalent of ultrasound. This property makes it an attractive option for optical diagnosis of diseases of internal organs, and has prompted several studies of its applicability to detecting tumors *in vivo*, including esophageal [118], cervical [119], intestinal [120], bladder [121] and breast cancers [122-125].

Miniaturization of OCT probes for endoscopic studies necessitates the development of alternative beam deflection mechanisms to galvanometric scanning. Proximal scanning techniques have been extensively investigated in prior studies. These techniques typically employ a tube containing a single-mode fiber fused to a microlens and right-angle prism. The tube is housed within a protective sheath, and can be translated axially [114, 126], or rotated [116] about the central axis of the probe. Tomographic 2D OCT images are obtained from these purely rotational and purely translational scans. A three-dimensional volume map may be obtained when both scan are employed simultaneously, resulting in a helical 3D scan [24], however rendering the image requires complex processing. Proximal scanning systems, besides suffering from slow scan rates, poor precision and repeatability, are only useful in sideways-imaging probes for visualization in tubular structures such as the gastrointestinal tract and esophagus. High-resolution 3D imaging in forward-imaging configuration can significantly enhance a physician's understanding of the pathology by providing tomographic, microscopic, and *en face* views of the sample simultaneously. 3D imaging probes require distal scanning mechanisms and advancements in catheter design to image in narrow, sensitive, and non-tubular human organs. Unfortunately, these probes are much harder to assemble in compact form factor, resulting in far fewer studies using them. Distal scanning can be performed by scanning the fiber, objective lens, and by beam steering using paired angle-polished rotating GRIN lenses or scanning micromirrors. Fiber and objective scanning can be performed using piezoelectric actuators [127] and tuning forks [128]. However, these suffer from limited field-of-view and scan rates, respectively.

Microelectromechanical system (MEMS) technologies are viewed as a potential solution to these problems. MEMS technology affords the unique capability to package micro-optical elements with actuators on a chip scale for *in vivo* imaging [129]. Scanning micromirror technologies have previously been used in OCT for endoscopic imaging [130-133]. Our high-speed 2-axis MEMS scanning micromirrors offers the advantages of high-reflectivity metal-coated surface, two-axis rotation about a single in-plane pivot point, and high-speed arbitrary scan patterns for *en face* imaging. We describe here its application to high-speed *in vivo* 3D imaging via optical coherence tomography.

5.1.1 Materials and methods

In this work, we employed swept-source optical coherence tomography (SS-OCT) utilizing a high-reflectivity two-axis vertical combdrive scanning micromirror. Spectral domain (i.e., Fourier-domain/Swept-source) techniques have been shown to provide significant signal-to-noise ratio and imaging speed advantages over time-domain OCT [134, 135]. SS-OCT, in particular, enables real-time micrometer-resolution diagnostic imaging over millimeter depth range due to improvements in spectral range, linewidth and scan speed of swept wavelength lasers. Figure 5.1 illustrates the schematic of our 3D SS-OCT instrument based on the two-axis silicon MEMS scanning mirror. Fiber-based instrumentation layout and swept-source configuration similar to that used in [136] is adopted due to the high sensitivity demonstrated by the approach, ease of alignment, portability, and maneuverability after incorporation of the scanning micromirror and optical elements into a miniaturized distal probe.

We used a high-speed fiber-coupled scanning light source that executes 20,000 wavelength scans per second over a 110 nm bandwidth centered at 1310 nm. The laser beam is coupled into a fiber-based Mach-Zehnder interferometer comprising a 90:10 coupler, two 3-port circulators, and 50:50 coupler. Port 2 of the circulators attach to the sample and reference arms of the interferometer. The sample arm has a single-mode fiber, the light output from which is collimated onto the micromirror. The micromirror is placed at the back focal plane of a Steinheil triplet lens (JML Optical, TRP14340/100, 0.6NA, 7.5mm EFL) serving as objective. The reference arm consists of a single-mode fiber, light from which is focused on to a stationary reference mirror via a relay lens. The

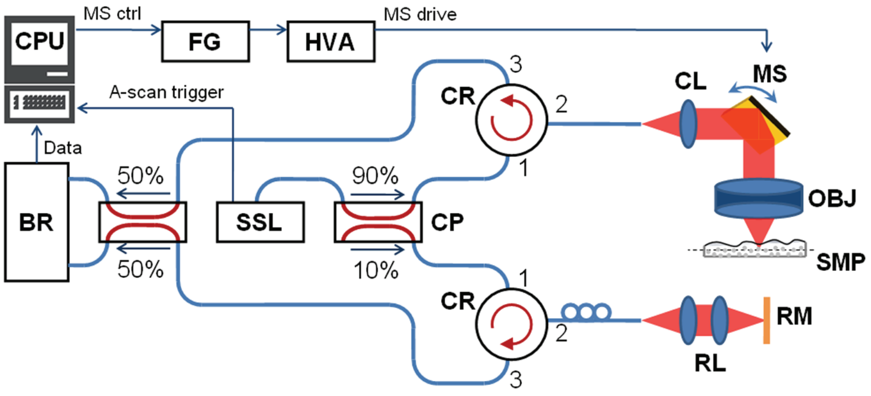

Figure 5.1: Illustration of optical scheme of the 3D swept-source optical coherence tomography system incorporating the scanning micromirror. SSL: swept-source laser; CP: coupler; CR: 3-port circulator; CL: collimating lens; MS: micromirror scanner; OBJ: objective lens; SMP: sample; RL: relay lens system; RM: reference mirror; BR: balanced receiver; FG: function generator; HVA: high-voltage amplifier; CPU: central processing unit.

optical path lengths of the reference and sample arms are matched to within a few tens of micrometers. Light directly backscattered from the sample and reference are recombined at the 50:50 coupler, and detected by a balanced infrared photodetector. Sampling of the photodetector output by the central processing unit is triggered at equal intervals of optical frequency. The phase difference between sample and reference arm reflections as a function of optical frequency is measured over the 110 nm spectral range by sampling the interference signal between the backscatter from the two arms through the infrared photodetector as the illuminating optical frequency is varied. The Fourier Transform of this spectral interference signal provides a map of the reflectivity profile of the sample as a function of depth [137]. The scanning micromirror moves the beam spot laterally in two dimensions (in raster fashion) and the axial reflectivity profiling is performed at each point to develop a 3D map of the object space. The detection and signal processing are performed in a LabVIEW software module.

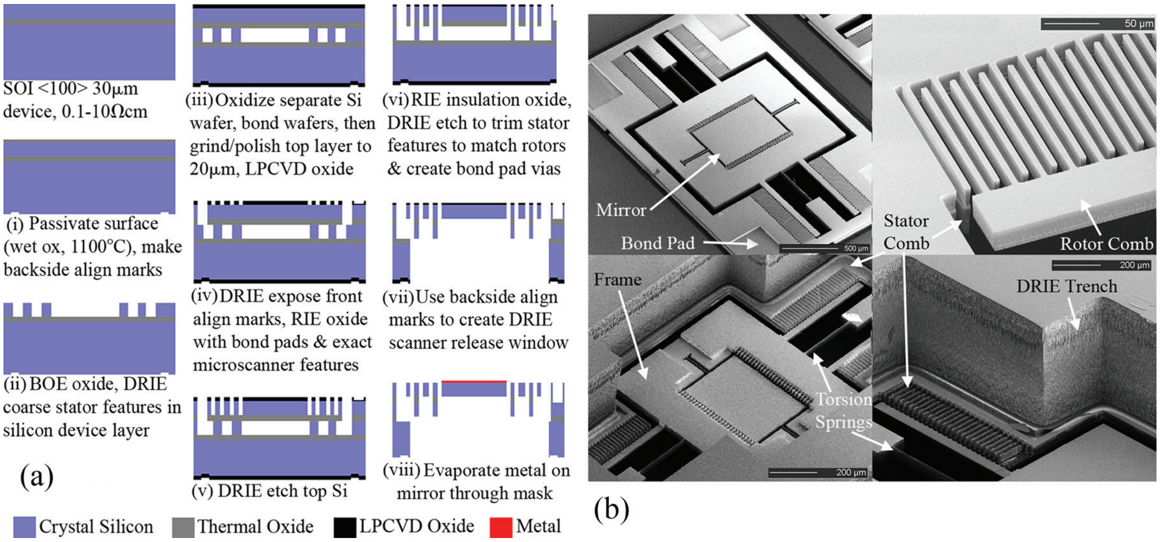

Figure 5.2: Fabrication of high-reflectivity two-axis vertical combdriven scanning micromirrors. (a) Process flow for device fabrication. (b) Scanning electron micrographs of the micromirrors depicting mirror and frame design, torsion springs, stator and rotor combs, bond pads, and backside deep reactive ion etching release window.

The scanning micromirrors used in this setup were fabricated by a five-mask process employing deep reactive ion etching different from that used in the experiments described earlier in this dissertation, and previously described in Refs [138, 139]. Figure 5.2(a) outlines the silicon micromachining process used to fabricate the scanning micromirrors. Coarse features of stationary electrostatic actuating comb drives are etched by deep reactive ion etching (DRIE) into the 30 µm conductive device layer of a silicon-on-insulator (SOI) wafer. A separate silicon wafer is oxidized to form an electrical isolation layer, fusion-bonded on top of the SOI wafer, ground down to 20 µm thickness, and polished to give a smooth (less than 50 nm RMS surface roughness) optical surface. The mirror and rotor combs are fabricated in this layer. A layer of 1.5 µm thick silicon dioxide, serving as a silicon etch hard mask, is deposited by low pressure chemical vapor deposition (LPCVD). After dry etching through the top device layer to expose alignment marks in the lower silicon layer, electrical bond pad features are etched partially (1.2 μm) and the exact features of the scanning micromirrors are etched through the oxide layer by reactive ion etching (RIE). The oxide layer is used as an etch mask to perform a DRIE–oxide RIE–DRIE sequence to create rotor comb features, bond pad vias to the lower silicon layer, and trim the underlying stator combs to match the lateral position of the stator comb features. This self-aligning technique affords a critical mask alignment tolerance of half the comb width (3.0 or 3.5 μm in our case) for stable and reliable scanner operation. A backside window is DRIE-etched beneath the device to release the micromirror, while simultaneously dicing the wafer into device chips. The remaining exposed oxide is removed from the front and backside by RIE. A <1-0-0> silicon wafer is anisotropically wet etched in potassium hydroxide using a silicon nitride masking layer at 70 ◦C to create a hard mask for sputtering. Using this hard mask, the micromirrors are selectively coated with metal by electron beam evaporation. The micromirror has design dimensions of 500 μm × 700 μm for compact oblique (up to 45°) illumination with a 500 μm diameter laser spot, and is coated with 125 nm of gold, resulting in greater than 90% uniform reflectance over the source spectrum. An important advantage of this scanner design is that, in a single plane, the mirror is suspended within a frame by the inner torsion springs and the frame is suspended by the outer torsion springs aligned in the orthogonal direction. This enables two-dimensional rotation about a single pivot point, reducing optical field distortions. Scanning electron micrographs of the fabricated device are shown in Figure 5.2(b).

5.1.2 Optical system design

The micromirror exhibits resonance on the inner and outer axes at 2.28 kHz and 385 Hz, respectively, and ±9◦ optical deflection on both axes for applied voltages of 110

V at low frequencies (Figure 5.3). Secondary peaks are also observed at half and twice the actual resonant frequency of the primary vibration mode shape. Due to the highly capacitive nature of the electrostatic actuators, the micromirror actuation requires very low current (usually of the order of 1–10 nA) for operation in non-resonant mode and around 2.4 μA in resonant mode on either axis.

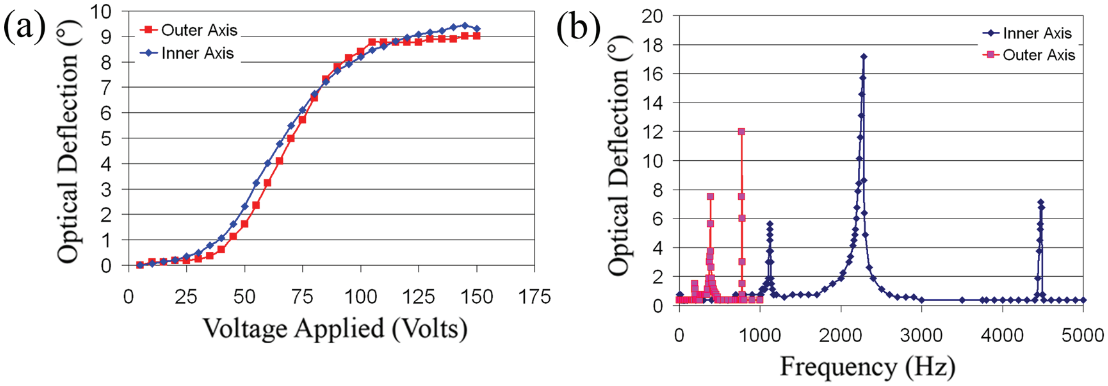

Figure 5.3: Operating characteristics of the high-reflectivity two-axis scanning micromirror. (a) Optical deflection characteristics for low-frequency voltage applied to a single vertical combdrive on each rotation axis. (b) Frequency-dependent optical deflection characteristics. Voltage applied to one vertical comb on each rotation axis is $V = 18.0 + 9.0 \sin(2\pi f t)$ volts.

The product of the micromirror scan angle and diameter determines the maximum number of resolvable points that can be obtained in the lateral dimensions. The choice of whether sharp resolution or large field of view is preferred is made in the process of selecting the numerical aperture of the objective system to focus the scanned beam onto the sample (the maximum imaging depth and resolution are determined solely by the characteristics of the swept wavelength laser, and are discussed later in this section). Ideally, lateral spatial resolution on the order of the diameter of a cell is preferred, along with a view field spanning between 1-2 millimeters. ZEMAX optical design simulations allow us to examine the suitability of the objective to meet these constraints and operate

(a) ZEMAX Layout: Scanning System

(b) Full-Field Spot Diagram

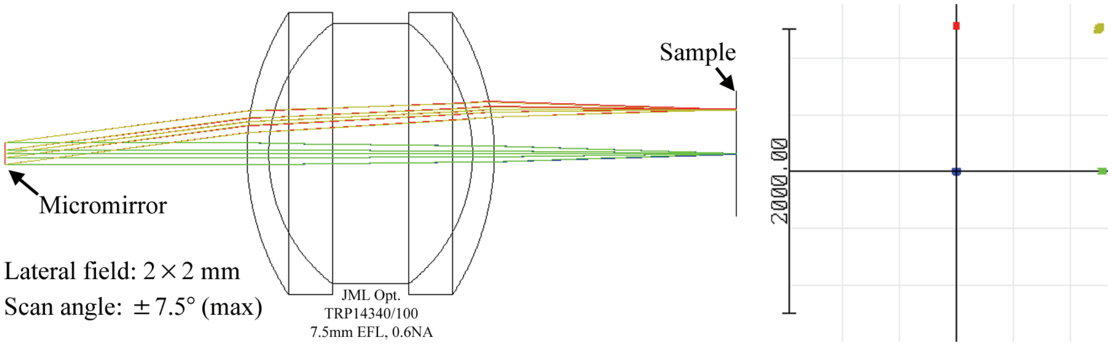

(c) MTF (λ=1.31μm) by spot location

(d) Focal plane spot size (λ=1.31μm)

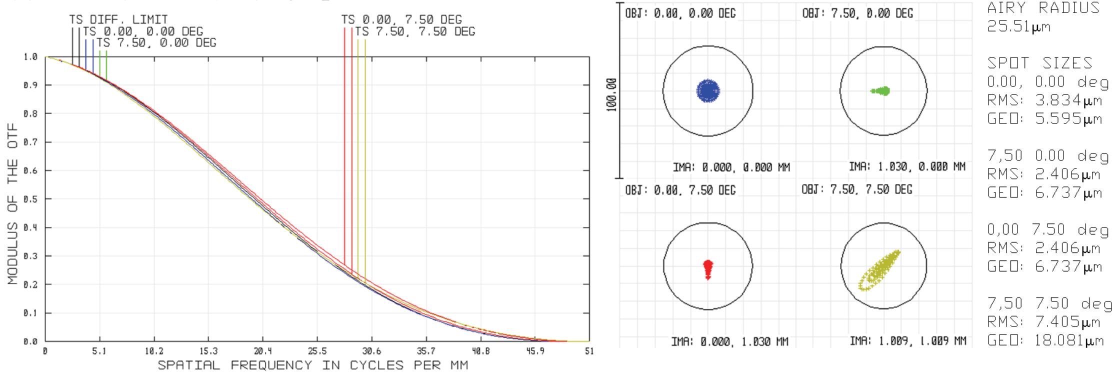

(e) Spot size vs. wavelength

(f) Through-focus spot size

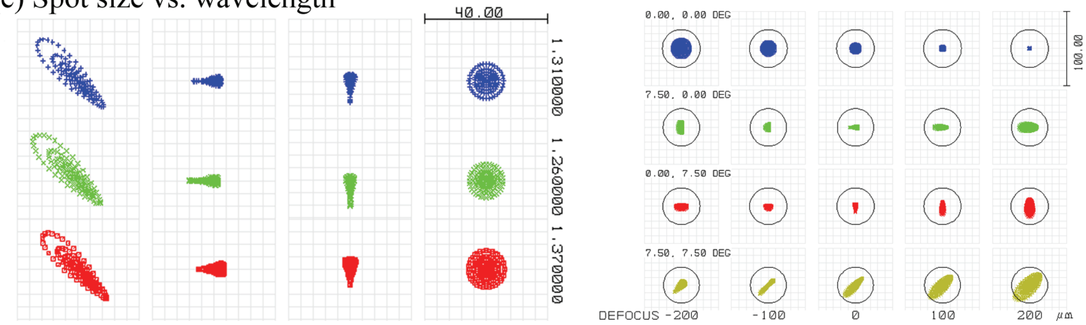

Figure 5.4: ZEMAX simulations of scan unit. (a) Layout of scanning unit. (b) Field diagram indicating the four locations where performance is characterized. (c) Modulation transfer functions of field configurations (1.31μm wavelength). (d) Focal plane spot size for field configurations, (1.31μm wavelength). (e) Focal plane spot size comparison at three wavelengths. (f) Relative spot sizes for the field configurations with defocusing.

with minimal aberrations over the entire source spectrum. The Steinheil triplet lens was chosen for its ability to provide achromatic operation, good off-axis performance, and minimum Seidel aberrations. Figure 5.4 includes a schematic of the optical layout of our scanning system in ZEMAX and graphics illustrating the calculated optical performance of the system over the desired lateral field of view of 2 × 2 mm.

The simulations indicate that the scanner is required to traverse a maximum optical scan angle of ±7.5° about each axis to obtain the required lateral view field of 2 × 2 mm, which is within the capabilities of our micromirror when using double-sided actuation. The modulation transfer functions, focal spot sizes, and defocused spot sizes (Figures 5.4(c-f)) for the center and extreme wavelengths of the source spectrum were calculated at the four positions within the view field indicated in Figure 5.4(b). The simulations show that diffraction-limited performance, with cellular-level lateral resolution, is obtained at all wavelengths within the source spectrum over the entire field of view. The axial resolution of the instrument is solely dependent on the characteristics of the swept wavelength source. The laser performs 20,000 wavelength scans per second over the 110 nm 3-dB spectral bandwidth centered at 1310 nm, theoretically providing $(2\ln 2/\pi)(\lambda_0^2/\Delta\lambda)$= 6.9 μm axial resolution. The laser coherence length is specified as 6 mm; however the imaging depth is practically limited to 1-2 mm in turbid samples due to degradation of the signal-to-noise ratio by light scattering in the tissue. The system acquisition rate of 10.8 million volume pixels (voxels) per second results in the completion of one entire volume scan in approximately 15 seconds, representing an order-of-magnitude improvement in acquisition rate over equivalent time-domain optical coherence tomographic systems.

5.1.3 Imaging results: *in vivo* human epidermis

We demonstrated the capabilities of our scanning micromirror based SS-OCT system by acquiring 3D reflectivity profiles over a 2 × 1 × 4 mm^3 volume of rigid

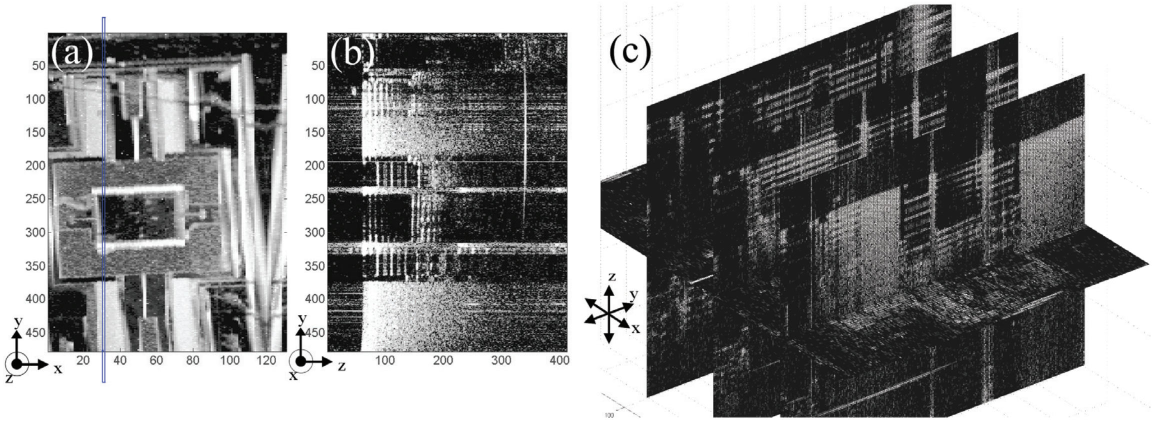

Figure 5.5: Results of 3D SS-OCT imaging of our scanning micromirror. (a) *En face* view of the scanning micromirror, depicting mirror surface, torsion rods, bond pads, electrical bonding wires, and sub-surface inner stator combs. Field of view is 2 × 1 mm. (b) Tomographic image of the scanning micromirror obtained at the location corresponding to the blue rectangle in (a). (c) Slice images at different positions and orientations through the micromirror device, demonstrating volume image acquisition capability.

structures, *in vitro* biological samples, and *in vivo* human epidermis. Lateral field of view of 2 × 1 mm is obtained by using both combdrive actuator banks on the inner axis, while using only a single bank on the orthogonal outer axis. Results of the 3D imaging of rigid structures, namely one of our packaged scanning micromirrors without metal reflectivity coating, are presented in Figure 5.5. The information present in the entire 3D volume can be represented in a 2D *en face* view by integrating the reflectivity profile along the axial direction. The micrometer-scale features, such as the micromirror torsion springs, electrical bond pads and a 20 μm diameter bonding wire connecting to the top left bond pad, are clearly visible from the *en face* image in Figure 5.5(a), indicating that the system achieves the micrometer resolution predicted by our ZEMAX simulations. The subsurface stator combs for the inner rotation axis are also visible in the image, as evidenced by comparison with the scanning electron micrographs in Figure 5.2(b). A single tomographic (cross-sectional) 2D image oriented along the direction of the blue rectangle in Figure 5.5(a) is depicted in Figure 5.5(b). Several tomographic cross-sectional slices across different positions and orientations of the micromirror are plotted in Figure 5.5(c), demonstrating the capability of the system to reveal the detailed internal structure of the imaged device. The vertical combdrives typically cause large amounts of laser light scattering, leading to the grainy portions in the image, similar to speckle noise. The mirror section of the device is not coated with any reflective metal, and is dark as it scatters very little of the incident light due to high transmission of silicon at infrared wavelengths.

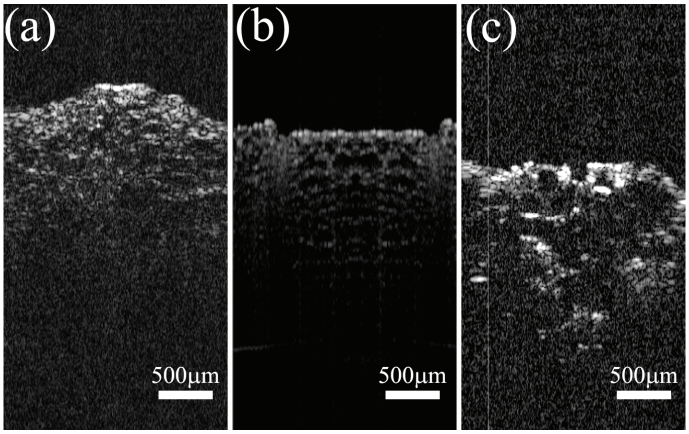

Figure 5.6: Tomographic 2D images of *in vitro* biological samples. Lateral scan width is 2 mm. (a) Single frame from 40 frames per second (fps) video of pickle slice obtained using the scanning micromirror. (b) Tomographic image of pickle slice from a different location using traditional galvanometric scanning. (c) Still frame from 40 fps video of an onion peel using the scanning micromirror.

We acquired tomographic images of *in vitro* biological samples at 40 frames per second (fps) by operating the scanning micromirror about only one axis of rotation. Figure 5.6 presents tomographic images of a pickle slice obtained using the scanning micromirror, and from a traditional galvanometric scanner from different regions of the sample, and an onion peel using the micromirror. Subsurface morphology is clearly visible in all the tomographic images.

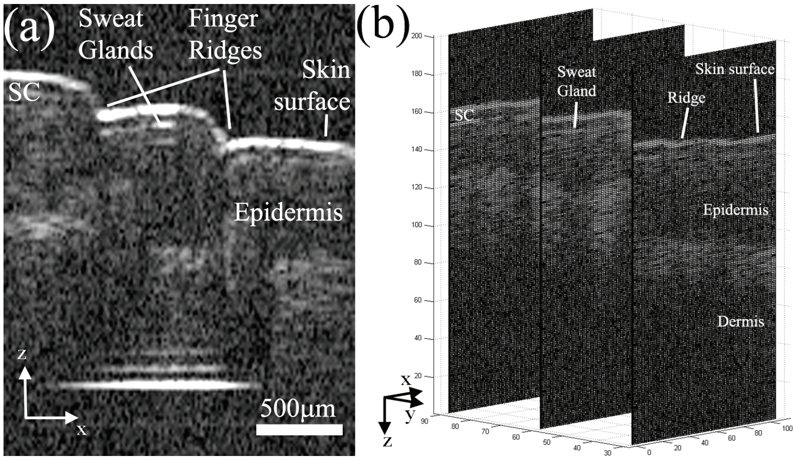

Figure 5.7: Results of 3D *in vivo* imaging of human skin using the micromirror-based SS-OCT system. (a) Still frame in 3D map acquired at 10.8 million volume pixels per second. Sub-surface tissue micro-architecture including skin surface, finger ridges, sweat gland grants, stratum corneum (sc), epidermis and dermis are clearly distinguished. (b) Tomographic slices of 3D volumetric data obtained from human skin. Each slice has a lateral extent of 1 mm (1 mm/100 pixels). The variation in epidermis thickness is visible from the parallel slices across different locations of the skin.

Finally, we obtained real-time 3D images of in vivo human finger skin using our system. Tomographic slices through the imaged volume are shown in Figure 5.7. The micron-scale tissue architecture including skin surface, finger ridges, sweat glands, stratum corneum, epidermis and dermis are clearly visible in the slice images. In some of the images, lens flare artifacts are visible, but these can be repositioned away from the imaging region of interest by varying the path length difference between the sample surface and reference reflection.

5.1.4 Discussion

The field of view and resolution of the instrument play an important role in determining the applicability of a device to clinical requirements. In SS-OCT, The lateral and axial resolutions of the instrument are governed by independent factors. The axial resolution is inversely proportional to the spectral bandwidth of the swept-frequency laser. The lateral resolution is determined purely by the micromirror and scanning optics. The diameter of the scanning micromirror limits the maximum beam diameter incident on the objective lens, and therefore determines the effective numerical aperture of the focusing lens. The number of resolvable points of our system can be improved by increasing the product of the mirror diameter–scanning angle product, which is then transformed into a given lateral field of view and resolution, depending on the numerical aperture of the objective, which can be selected according to the requirements of the application. In our experiments, some instability in lateral scanning was observed, which can be countered by using our CMOS-compatible scanning micromirrors with angular position feedback sensors incorporated monolithically into the device, enabling adaptive control of scan linearity. Miniaturization of the MEMS scanning optics with the use of fiber-fused graded index (GRIN) collimators, stationary micro-prisms and monolithic electronics integration such as flip-chip bonding for power supply and signal conditioning will enable possible clinical application of the instrument for applications such as gastroenterology, urinary/reproductive tract and pulmonary imaging that allow catheter diameters of 5 mm [16]. Real-time *in vivo* volume image acquisition of sub-surface morphology at micrometer resolution may enable their application to minimally invasive disease diagnostics, image-guided biopsy and photodynamic therapy.

5.2 Miniaturization: Scanning Fresnel Zone Plate Objectives

Miniaturization of distal-end optics assemblies is crucial to the successful transfer of innovative minimally-invasive diagnostic technologies from research laboratories to clinical medicine. Visualization in sensitive internal non-tubular human organs requires compact forward-imaging endoscopes, which have thus far proven to be difficult to assemble in small form factors. An examination of the common components present in endoscopic assemblies reveals the factors that limit miniaturization. Endoscopes that employ proximal scanning techniques such as those in Refs [114, 116] usually suffer from slow scan rates, poor precision and repeatability, and are intractable for forward-imaging. Endoscopes based on fiber bundle designs are adaptable to forward-imaging, but suffer from pixilation imaging artifacts. Therefore, endoscopes incorporating distal scanning mechanisms are favored for non-tubular organ imaging. These endoscopes usually incorporate a collimating element, such as a graded-index (GRIN) fiber-fused lens, and stationary mirror to direct the light exiting the optical fiber onto a scanning element, such as a scanning micromirror. The micromirror may be positioned before (pre-) or after (post-) an objective lens designed to focus the beam in to a small volume at the sample. The outer diameter and rigid length of the endoscope is determined by the sizes and positions that all of these components are required to have within the endoscope. In the case of pre-objective scanning, the beam deflecting off the micromirror is required to under-fill the lens to account for scanning, meaning that a large diameter lens is required. Post-objective scanning eliminates this drawback, but is not suited to imaging at the same high resolution as pre-objective scanning. This is because the objective has to have low numerical aperture (NA) to provide enough working distance within which to place the micromirror and sample to be imaged. Also, the complex assembly of these multi-element systems within the endoscope becomes increasingly challenging and expensive. The present invention attempts to address the above limitations by combining the beam scanning and focusing functions onto a single chip. The need for focusing optics is thus obviated, simplifying microendoscope assembly and improving form factor. Monolithic integration of a Fresnel zone plate [93] directly on the surface of a 2-axis scanning micromirror by patterning of reflective binary-phase modulation elements into the silicon of the mirror region of the device accomplishes this task. Careful design of the parameters of the zone plate, as outlined in the next section, can ensure that minimal degradation of the focal spot size occurs as the incident angle of the beam on to the zone plate is varied from the nominal angle (by rotation of the micromirror). In addition to simplifying the microendoscope assembly, the scanning Fresnel zone plate (sFZP) combines the strengths of pre- and post- objective distal scanning systems by providing the maximum possible working distance without requiring the use of an objective with low numerical aperture, as the act of beam convergence begins to occur only after being deflected by the scanning micromirror with patterned zone plate.

5.2.1 Theoretical Framework

Consider a Fresnel zone plate as shown in Figure 5.8. We desire to achieve focusing of coherent illumination incident on the zone plate along the axis of the global

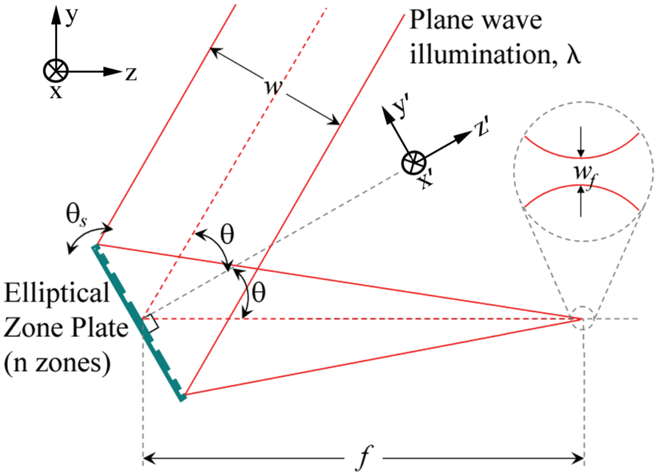

Figure 5.8: Illustration of the design parameters for the microelectromechanical scanning binary-phase reflective Elliptical Zone Plate (EZP). θ is the nominal off-axis illumination angle of incident light of wavelength λ, θ_s is the micromirror scan angle, w and w_f are the incident and focused beam waists, and f is the focal length of the EZP with n zones.

optical system, with respect to which the optic axis of the zone plate is tilted by an angle θ about the x-axis of the system (or equivalently, the x'-axis of the zone plate). This tilt causes the phase $\phi(y)$ of the incident light to vary across the zone plate according to equation (5.1) –

$$\phi(y) = -ky\sin\theta \tag{5.1}$$

For a point $P'(x', y')$ on the surface of the zone plate to lie on the boundary of a zone, it must satisfy the condition that the optical path length (OPD) difference between the ray from $P'(x', y')$ to the focus and the central point on the zone plate to the focus is an integral multiple of half the design wavelength, i.e. –

$$k\left(\left|\vec{P}O\right| - \left|\vec{O}'O\right|\right) + \phi(y) = n\pi \tag{5.2}$$

From Figure 5.8, the point $P'(x', y')$ on the surface of the zone plate transforms into the point $P(x, y, z)$ in the global coordinate system according to equation (5.3) –

$$[x', y'] \Leftrightarrow [x, y\cos\theta, -y\sin\theta] \tag{5.3}$$

Assigning $\left|\vec{O}'O\right|$ to be the focal length f of the zone plate, and applying (5.3) in (5.2), we obtain –

$$\left[x^2 + y^2\cos^2\theta + (f + y\sin\theta)^2\right]^{\frac{1}{2}} - f - y\sin\theta = \frac{n\lambda}{2} \tag{5.4}$$

$$\Rightarrow x^2 + y^2\cos^2\theta = n\lambda(f + y\sin\theta) + \frac{n^2\lambda^2}{4} \tag{5.5}$$

This, on simplifying and re-arranging, yields the design equation (5.6) –

$$x^2 + \cos^2\theta\left(y - \frac{n\lambda\sin\theta}{2\cos^2\theta}\right)^2 = nf\lambda + \frac{n^2\lambda^2}{4\cos^2\theta} \tag{5.6}$$

Equation (5.6) is similar to the standard equation for a Fresnel zone plate with circular zones, and reduces to it in the limit $\theta \to 0$. The second order term

$n^2\lambda^2/\left(4\cos^2\theta\right)$ is sometimes neglected for simplicity. Equation (5.6) can also be represented in a different form –

$$\left(\frac{x}{a_n\cos\theta}\right)^2+\left(\frac{y-b_n}{a_n}\right)^2=1 \tag{5.7}$$

Where $a_n=\dfrac{\sqrt{n\lambda\left(f\cos^2\theta+\dfrac{n\lambda}{4}\right)}}{\cos^2\theta}$ and $b_n=\dfrac{n\lambda\sin\theta}{2\cos^2\theta}$

Equation (5.7) describes an elliptical zone plate (EZP), in which the boundaries of the zones of the focusing element form a series of non-concentric ellipses, each having a minor-to-major axis ratio equal to the cosine of the illumination tilt angle. Equation (5.6) has been presented earlier in [140], but we derive it here from first principles for completeness. We now consider the aberration theory of EZPs to determine the operating limits of the device.

The design equation for the boundaries of the zones of an EZP determines the set of all points on the surface of the zone plate that have an optical path distance from the beam focus that differs from the path length from the zone plate center to the focus by an integral multiple of the half of the design wavelength [Equation (5.4)]. The optical path difference (*OPD*) is given by –

$$OPD=\left[x^2+y^2\cos^2\theta+\left(f+y\sin\theta\right)^2\right]^{\frac{1}{2}}-f-y\sin\theta \tag{5.8}$$

Using a strategy adopted earlier [141], we expand the *OPD* in a power series to analyze the aberrations of an EZP. Assuming that the dimensions of the EZP are much smaller than its focal length –

$$OPD=\left(f+y\sin\theta\right)\left[1+\frac{x^2+y^2\cos^2\theta}{\left(f+y\sin\theta\right)^2}\right]^{\frac{1}{2}}-f-y\sin\theta$$

$$= \left[f + y\sin\theta + \frac{x^2 + y^2\cos^2\theta}{2(f + y\sin\theta)} - \frac{(x^2 + y^2\cos^2\theta)^2}{8(f + y\sin\theta)^3} + \ldots \right] - f - y\sin\theta$$

$$= \frac{x^2 + y^2\cos^2\theta}{2(f + y\sin\theta)} - \frac{(x^2 + y^2\cos^2\theta)^2}{8(f + y\sin\theta)^3} + \ldots \qquad (5.9)$$

The term $(x^2 + y^2\cos^2\theta)^2 / \{8(f + y\sin\theta)^3\}$ represents spherical aberration. Spherical aberration is indiscernible until it reaches a value λ/4, and several wavelengths of spherical aberration are usually tolerable [142]. Setting the spherical aberration to quarter-wavelength, incorporating equation (5.5), neglecting $n^2\lambda^2 / \{4\cos^2\theta\}$, and assuming that the focal length is much larger than the EZP dimensions, we get –

$$\frac{n^2\lambda^2}{8f} = \frac{\lambda}{4} \Rightarrow n \approx \sqrt{\frac{2f}{\lambda}} \qquad (5.10)$$

Equation (5.10) estimates the maximum number of zones that can be incorporated into an EZP of focal length *f* at design wavelength λ without introducing significant spherical aberrations. This relation is identical to that of circular zone plates designed for normal illumination.

The EZP is normally designed for a specific wavelength. Chromatic aberration describes the change in axial position of the focus with change in illumination wavelength. If the EZP is designed for wavelength λ, we have –

$$OPD = \frac{n\lambda}{2} \qquad (5.11)$$

If the EZP is now illuminated with wavelength λ’, chromatic aberration will become noticeable when –

$$OPD = \frac{n\lambda'}{2} \pm \frac{\lambda'}{4} \Rightarrow \frac{n\lambda}{2} = \frac{n\lambda'}{2} \pm \frac{\lambda'}{4} \Rightarrow n \approx \frac{\lambda}{\Delta\lambda} \qquad (5.12)$$

Therefore, for systems where chromatic operation is desired (e.g., in confocal imaging systems where the axial scanning is performed by wavelength tuning), an EZP with larger number of zones is desired, while in systems requiring achromatic operation, equation (5.12) prescribes a limitation on the maximum number of zones, and therefore the minimum focal spot size, that can be achieved.

In a similar vein, the maximum scan angle can be deduced by considering the difference in OPD between a marginal and axial ray, when an additional tilt angle (i.e., micromirror rotation angle) α is introduced between the principal ray and the central axis. Assuming that the number of zones is relatively few (which is true in the case of small micromirror designs), we obtain equation (5.13) –

$$\alpha = (3n)^{-1/2} \tag{5.13}$$

The conditions described in equation (5.10), (5.12), and (5.13) restrict the maximum number of EZP zones and micromirror scan angle, therefore determining the maximum number of resolvable points in the image, or the "numerical aperture" of the EZP. The parameters described here can now be optimized to suit the requirements of the applications on the basis of these three conditions.

5.2.2 Materials and methods

The scanning Fresnel zone plate (sFZP) is created on a micromirror actuated by staggered vertical combdrives [143]. Coarse features of the stator are etched by Deep Reactive Ion Etching (DRIE) into 25 µm thick <1-0-0> Silicon-on-Insulator (SOI) device layer, as shown in the illustration of the fabrication process in Figure 5.9(a-f). An oxidized <1-0-0> wafer is fusion bonded on top of the patterned wafer, and ground down to 25 µm thickness with <50 nm RMS surface roughness to form the micromirror surface. Features of the EZP objectives are patterned on the surface to quarter-wavelength depth to provide π-phase shift relative to reflections off unetched areas. Exact features of the actuators aligned to the lower layer features are etched into a layer of silicon dioxide deposited by low-pressure chemical vapor deposition (LPCVD). Following this, a DRIE-oxide RIE-DRIE etching sequence forms the self-aligned vertical combdrive actuators. Backside substrate DRIE and oxide RIE on both sides releases the mirror and removes remaining protective oxide. Scanning electron micrographs of the fabricated device are presented in Figure 5.9(g-i).

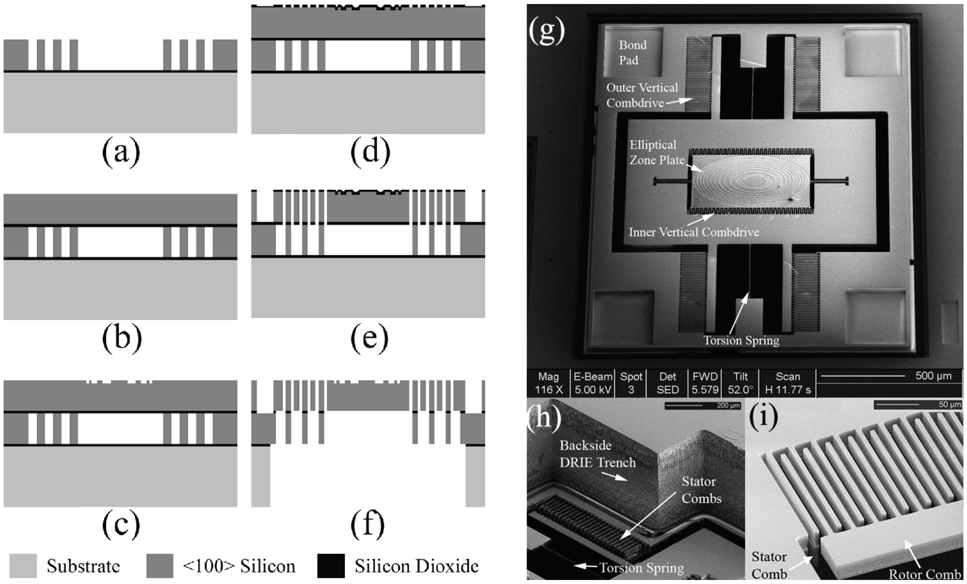

Figure 5.9: The microelectromechanical scanning Fresnel zone plate (sFZP). (a-f) Device fabrication process sequence. (a) DRIE of coarse features in to SOI device layer. (b) Bond oxidized wafer, grind/polish. (c) Pattern binary-phase modulation elements of zone plate into micromirror surface. (d) Deposit silicon dioxide and pattern with exact micromirror features. (e) DRIE-oxide RIE-DRIE etch sequence to create self-aligned actuators. (f) Backside DRIE to release micromirror, and oxide RIE on both sides to remove protective oxide. (g-i) Scanning electron micrographs of fabricated device. (g) Top view, showing EZP, vertical combdrives, torsion springs, and bond pads (h) Backside view showing DRIE trench to release the micromirror. (i) Close-in view of vertical combdrive actuators.

Preliminary testing of image-formation capabilities of the device was performed in a simple transmission-mode experiment depicted in Figure 5.10(a). A sample with spatially-varying transmission was placed in the focal plane of an sFZP, and transmitted light was concentrated into a photodetector using two collection lenses. The devices were then incorporated into a portable bench-top single-fiber laser-scanning reflectance confocal microscope that is better suited to eventual use for *in vivo* imaging applications. Polarized light from a 635 nm wavelength semiconductor diode laser is launched into a single-mode polarization-maintaining fiber, aligned to the fiber slow axis. After collimation into a beam matched to the size of the EZP on the sFZP, the linearly polarized light is converted into circularly polarized light by a quarter-wave plate before being simultaneously focused and scanned across the sample by our device. Reflected light from the sample maintains some component of circularly polarized light, which is converted into light linearly polarized along the fiber fast axis, orthogonal to the incident illumination. This allows the walk-off polarizer to separate the sample reflection from laser illumination and direct it to an avalanche photodetector.

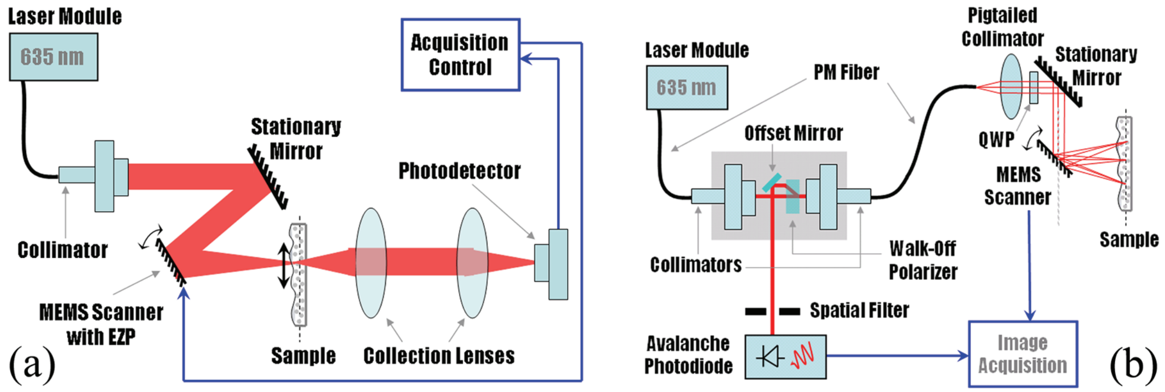

Figure 5.10: Imaging experiments to test image-formation capabilities of the micro-electro-mechanical scanning Fresnel zone plate (sFZP). (a) Schematic of transmission-mode imaging experiment for preliminary device testing. (b) Schematic of single-fiber laser-scanning reflectance confocal microscope incorporating the sFZP.

5.2.3 Experimental Results

The sFZP exhibits operating characteristics similar to the scanning micromirrors used in the SS-OCT study (Figure 5.3), as they were fabricated in the same batch of fabrication runs. The size of the focused spot of an EZP designed with 8 mm focal length for 635 nm wavelength illumination at 45° nominal incidence angle was profiled against micromirror rotation angle by measuring the far-field angular beam divergence (θ_f) of the Gaussian beam, and calculating the focused beam waist (w_f) using the formula –

$$\theta_f \approx \frac{2\lambda}{\pi w_f} \tag{5.14}$$

The measured focused spot size showed little degradation (Figure 5.11) for micromirror scanning angles up to 10° (optical) about both axes.

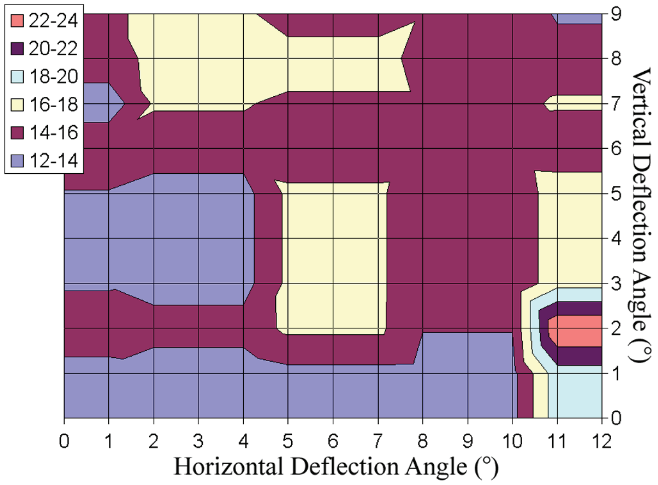

Figure 5.11: Map of diameter of the focused spot (in micrometers) created by an sFZP with 8 mm focal length for 635 nm illumination at 45° nominal incidence as a function of optical angular deflection of the sFZP.

The device was tested in the two setups depicted in Figure 5.10. Mylar transparencies printed with longhorn logos and numbers were imaged using the transmission-mode system at 5.0 frames per second [Figure 5.12(a)]. Images using the reflectance confocal imaging system of a standard USAF 1951 resolution target are depicted in Figure 5.12(b). Comparison with images obtained from an Olympus BX51 microscope using 10X objective, and calculations based on the line width of resolvable features in the resolution target images indicated an estimated field of view of 1 mm × 0.35 mm with approximately 15 μm lateral resolution.

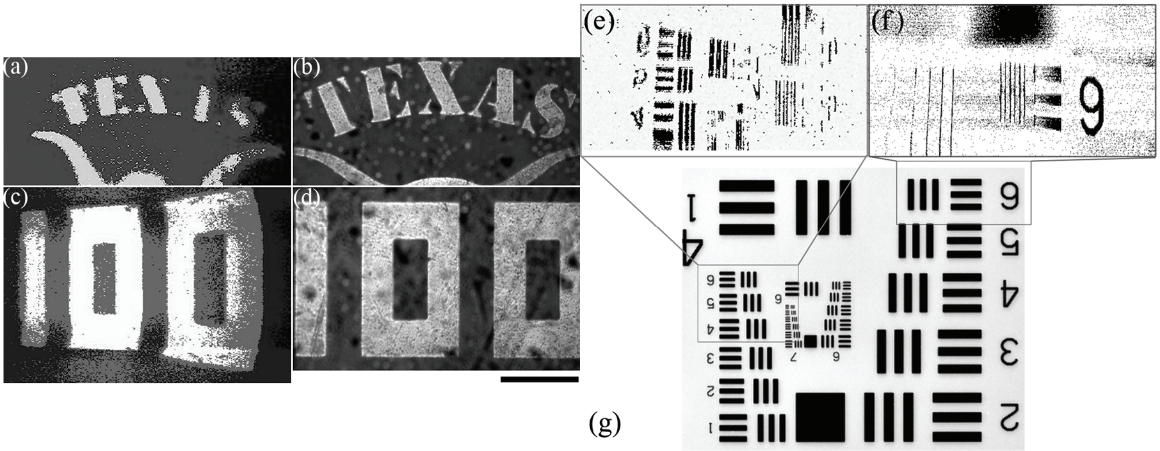

Figure 5.12: Imaging results using the sFZP device in experiments. (a,c) Mylar transparencies imaged using the sFZP in a preliminary transmission-mode imaging experiment. (b,d) Images of the samples using a Olympus BX51 reflectance microscope. (e-f) Results of imaging a USAF 1951 resolution target using a single-fiber laser-scanning reflectance confocal experiment. Field of view is 1 mm × 0.35 mm, and resolution is 15 μm. (g) Image of the resolution target using an Olympus BX51 microscope.

5.2.4 Discussion: Application Notes

The specific application of microelectromechanical scanning Fresnel zone plates may be considered as a special case of a class of devices employing phase modulation elements on high-speed rotating surfaces. Such devices may be applied, with great effect, in several other fields of endeavor.

Optical data communication networks have grown in transmission capacity and sophistication to accommodate the increasing demands on the internet. Wavelength and time-division multiplexed (WDM/TDM) optical network switches are an important

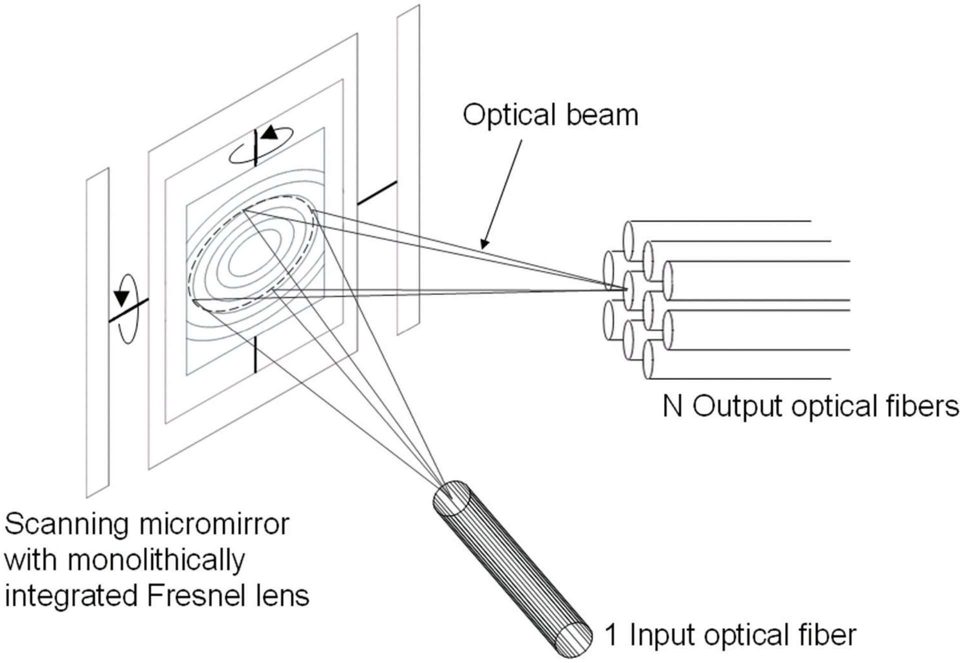

Figure 5.13: 1×N optical switch realized using two-axis scanning micromirror with monolithically integrated Fresnel zone plate.

component in optic-fiber communication. Microelectromechanical systems technologies demonstrate the unique ability to integrate electrical, mechanical, and optical elements on a single chip, and are therefore well suited to building WDM components. Our scanning micromirror with monolithically integrated Fresnel zone plate may be used a 1×N optical switch. The schematic of one embodiment of such a device is depicted in Figure 5.13. Light diverging while exiting from the input optical fiber is incident on the surface of the scanning micromirror, which is patterned with reflective phase modulation elements. In this particular instance, the pattern on the scanning micromirror is designed to behave as a Fresnel zone plate, which concentrates light into a small volume (at the beam focus), similar to the action of a lens. Rotation of the scanning micromirror about two axes (about a single pivot point) allows lateral scan of the focused beam. An output array of optical fiber may be placed at the focal plane of the scanning Fresnel lens. The output fiber into which the incoming beam must be directed can then be chosen by setting the rotation angle of the micromirror about the two rotation axes.

A second potential area of application is in high-speed tunable laser systems. Laser sources whose output wavelength can be tuned are extremely important in Wavelength Division Multiplexed (WDM) optical communication systems and in optical imaging techniques, including swept source optical coherence tomography. The Littrow configuration is a well-known and efficient method of obtaining a swept wavelength laser with large tuning range and narrow laser line width. A schematic for the Littrow configuration external cavity wavelength swept laser is shown in Figure 5.14.

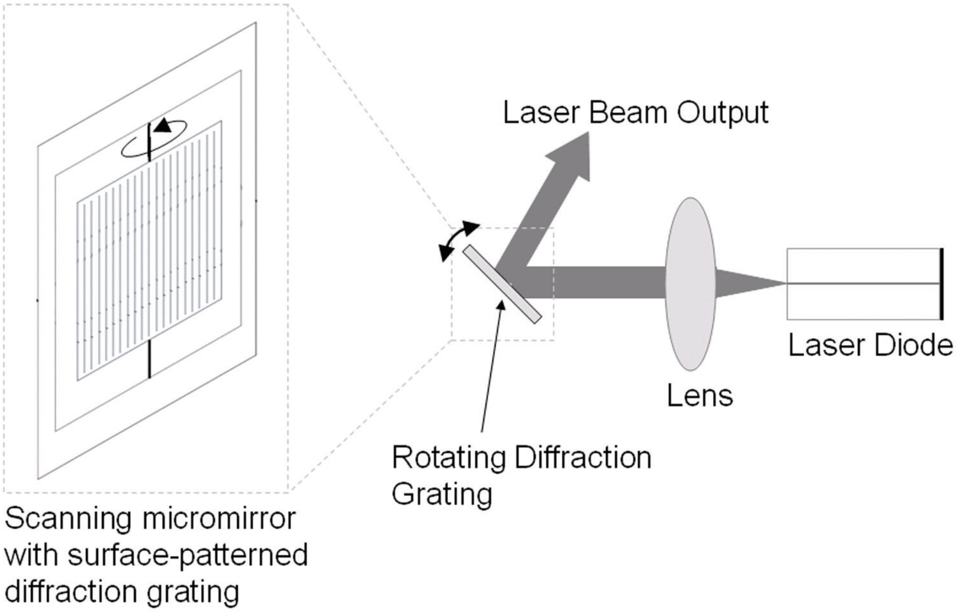

Figure 5.14: Schematic of Littrow configuration external cavity swept-wavelength laser using a scanning micromirror patterned with a linear diffraction grating.

A scanning micromirror (rotation about only one axis) with mirror surface patterned with a linear diffraction grating pattern can serve as the wavelength-selecting element in the Littrow configuration external cavity wavelength-swept laser [144]. In Figure 5.14, the laser diode amplifies a broad spectrum of wavelengths. Light exiting the laser diode is incident on a diffraction grating, which can be rotated about its central axis in order to change the angle of incidence of the light illuminating it. Light incident on the grating is either simply reflected off the grating as if it were a mirror (zeroth order diffraction), or diffracted at a wavelength-dependent angle (first and higher diffraction orders). First-order diffraction is strong while other orders are typically very weak and may be neglected. The different wavelengths of light incident on the grating are diffracted at different angles. There will be a single wavelength of light, whose diffraction angle equals the incidence angle, i.e., it retraces its path back directly into the laser diode. Therefore, a laser cavity is formed only for that particular wavelength, and therefore laser operation is restricted to that particular wavelength. By rotating the diffraction grating, the wavelength for which lasing operation occurs can be varied. Thus, a wavelength-swept laser can be obtained by continuously varying the rotation angle of the diffraction grating. The scanning micromirror with monolithically integrated diffraction grating can perform this function efficiently.

5.3 Conclusions

The scanning micromirror forms core enabling technological component that can enable several novel applications, including swept source optical coherence tomography and micromachined scanning Fresnel zone plate objectives. These two systems address important issues facing the microendoscope community in enabling physicians to visualize the micro-architecture of tissue in three-dimensions for a better understanding of tissue morphology, and creating more compact microendoscopes for unrestricted forward-imaging visualization in narrow, sensitive, and non-tubular human organs. In addition to these critical biomedical applications, the scanning Fresnel zone plates can potentially be used to solve several important problems in optical communication.

CHAPTER 6

DISSERTATION SUMMARY AND FUTURE DIRECTIONS

Microelectromechanical systems have emerged as a core enabling technology for the manipulation of light by micromechanical actuation and nanofabricated sub-wavelength optical phase modulation elements. Engineering of precision optical micro- and nano- systems can enable complex next-generation healthcare instruments providing new perspectives and enhanced minimally-invasive visualization of internal organs at levels of resolution and informative detail never captured before. Such miniaturized instruments can prove to be the driving force to make new discoveries and solve a myriad of healthcare-related problems of critical importance to the general public. We are particularly interested in the applicability of these instruments to endoscopic *in vivo* diagnostics, image-guided excisional microsurgery, and photodynamic therapy towards early cancer detection, treatment, and monitoring.

This dissertation experimentally demonstrates a handheld laser-scanning confocal microscope capable of both reflectance and fluorescence imaging targeted towards breast cancer imaging for early diagnosis and precise tumor margin assessment in cases of excisional therapy. The instrument is capable of resolving sub-cellular morphological features of single cell layer optical sections, of thickness similar to conventional histology, located up to several hundred micrometers deep within the tissue being investigated. The core technology that enables the instrument is a fast, highly reflective two-axis scanning micromirror driven by efficient self-aligned staggered vertical combdrives. The micromirror is fabricated by a novel micromachining process that requires only three masks (as opposed to six in competing technologies), and is compatible with traditional complementary metal-oxide-semiconductor (CMOS) processing employed in the consumer electronics industry. Our experiments and commercialization efforts reveal that micromirror fabrication processes compatible with traditional CMOS processing would enable integration of rotation sensors to adaptively correct for aberrations in beam scanning, while significantly increasing device yield, and reducing device development costs and barriers to market acceptance. The integrated optics-MEMS design approach translates the critical parameters required of our imaging instrument into the geometries of the micromirror. The dissertation presents imaging results from breast cancer, and also demonstrates applicability towards imaging of liver cirrhosis as an aid to surgeons in the operating theater. Additional, enhancements to endoscopic imaging enabled by the micromachined actuators are demonstrated by performing high-speed 3D forward-imaging optical coherence tomography and ultra-miniaturized imaging using a scanning Fresnel zone plate objective monolithically integrated on the surface of the micromirror.

The experimental results of this dissertation provide several key insights into the future directions this research can pursue. On the applications forefront, it is envisioned that highly detailed 3D simultaneously-correlated maps of the overexpression of multiple tumor markers will provide clinical diagnosticians and surgeons with the information they need to make the critical diagnosis and treatment decisions affecting patient outcomes with confidence. This dissertation addresses several of these aspects individually; however an endoscopic system that integrates these functions can be a powerful tool that can transform the field of *in vivo* minimally invasive intervention. Hyper-spectral microscopic imaging, a new imaging modality being developed in research laboratories, is one such transformative technique. The HMI collects the entire spectral information of the emission from multiple fluorescent tumor markers, each conjugated to a different targeted antibody. Using mathematical deconvolution algorithms, the relative contribution of each fluorophores can be assessed, yielding a map of the relative expression of the markers. We have previously employed this approach in the assessment of circulating tumor cells captured from whole blood of breast cancer patients, and believe this can be a revolutionary technique if adapted to minimally-invasive *in vivo* imaging. The fundamental micro-opto-electronic infrastructure, including the CMOS-MEMS co-fabricated micromirror and scanning Fresnel zone plate objectives that this dissertation presents, can be readily adapted to *in vivo* HMI imaging. From a commercial engineering perspective, a move to disposable cost-effective systems will enable rapid dissemination of the technology for use in clinical settings. In addition to the cost benefit realized due to economy of scale of the MEMS fabrication approaches, the laser seterolithographic rapid-prototyping methods employed in this research constitutes a step in this direction. Future implementations can incorporate custom-designed plastic injection-molded objective lens systems and batch-processed soft-material packaging systems. Advanced low-cost minimally-invasive systems realized by alternative soft packaging techniques and optical microelectromechanical systems hold the key to revolutionizing biomedical research and clinical diagnostic instruments in aid of global public healthcare initiatives.

References

[1] "CancerStats Reports: Worldwide Cancer," *Cancer Research UK*, 2005.

[2] "World Health Statistics," *World Health Organization*, 2008.

[3] K. McLarty and R. M. Reilly, "Molecular imaging as a tool for personalized and targeted anticancer therapy," *Nature*, vol. 81, pp. 420-424, 2007.

[4] "Cancer Facts and Figures," *American Cancer Society*, 2007.

[5] A. Jemal, T. Murray, E. Ward, A. Samuels, R. Tiwari, and A. Ghafoor, "Cancer Statistics, 2005," *Cancer Journal for Clinicians*, vol. 96, pp. 1094-1098, 2005.

[6] R. Etzioni, N. Urban, S. Ramsey, M. McIntosh, S. Schwartz, B. Reid, J. Radich, G. Anderson, and L. Hartwell, "The case for early detection," *Nature Reviews Cancer*, vol. 3, pp. 243-252, 2003.

[7] R. Herdman and L. Norton, *Saving Women's Lives: Strategies for Improving Breast Cancer Detection and Diagnosis*. Washington, D.C.: National Academies Press, 2005.

[8] http://www.son.wisc.edu/ce/programs/asynch/bccd/BrCa1/1-4-growthtypes.htm.

[9] R. G. McKinnell, R. E. Parchment, A. O. Perantoni, and G. B. Pierce, *The Biological Basis of Cancer, 2nd edition (Cambridge University Press, New York, 2006)*, 2006.

[10] M. J. Duffy, "Predictive markers in breast and other cancers: a review," *Clinical Chemistry*, vol. 51, pp. 494-503, 2005.

[11] H. Joensuu, L. Pylkkanen, and S. Toikkanen, "Bcl-2 protein expression and long-term survival in breast cancer," *American Journal of Pathology*, vol. 145, pp. 1191-1198, 1994.

[12] M. A. Olayioye, R. M. Neve, H. A. Lane, and N. E. Hynes, "The erB signalling network: heterodimerization in development and cancer," *The EMBO Journal*, vol. 19, pp. 3159-3167, 2000.

[13] T. T. Y. Wang and J. M. Phang, "Effects of estrogen on apoptic pathways in human breast cancer cell line MCF-7," *Cancer Research*, vol. 55, pp. 2487-2489, 1995.

[14] A. Karellas and S. Vedantham, "Breast cancer imaging: A perspective for the next decade," *Medical Physics*, vol. 35, pp. 4878-4897, 2008.

[15] D. A. Mankoff, "Molecular imaging as a tool for translating breast cancer science," *Breast Cancer Research*, vol. 10, pp. 1-12, 2008.

[16] Z. Yaqoob, J. Wu, E. J. McDowell, X. Heng, and C. Yang, "Methods and application areas of endoscopic optical coherence tomography," *Journal of Biomedical Optics*, vol. 11, pp. 063001, 2006.

[17] J. Bange, E. Zwick, and A. Ullrich, "Molecular targets for breast cancer therapy and prevention," *Nature Medicine*, vol. 7, pp. 548-552, 2001.

[18] D. Sidranksy, "Emerging molecular markers of cancer," *Nature Reviews Cancer*, vol. 2, pp. 210-219, 2002.

[19] R. Weissleder, "Scaling down imaging: molecular mapping of cancer in mice," *Nature Reviews Cancer*, vol. 2, pp. 1-8, 2002.

[20] R. Weissleder, "Molecular imaging in cancer," *Science*, vol. 312, pp. 1168-1171, 2006.

[21] R. Weissleder and M. J. Pittet, "Imaging in the era of molecular oncology," *Nature*, vol. 452, pp. 580-589, 2008.

[22] G. K. Fedder, R. T. Howe, T.-J. K. Liu, and E. P. Quevy, "Technologies for Cofabricating MEMS and Electronics," *Proceedings of the IEEE*, vol. 96, pp. 306-322, 2008.

[23] Y.-C. Cheng, C.-L. Dai, C.-Y. Lee, P.-H. Chen, and P.-Z. Chang, "A MEMS micromirror fabricated using CMOS post-process," *Sensors and Actuators A: Physical*, vol. 120, pp. 573-581, 2005.

[24] J. Su, J. Zhang, L. Yu, and Z. Chen, "*In vivo* three-dimensional microelectromechanical endoscopic swept source optical coherence tomography," *Optics Express*, vol. 15, pp. 10390-10396, 2007.

[25] A. F. Gmitro and D. Aziz, "Confocal microscopy through a fiber-optic imaging bundle," *Optics Letters*, vol. 18, pp. 565-567, 1993.

[26] S. A. Boppart, B. E. Bouma, C. Pitris, G. J. Tearney, J. G. Fujimoto, and M. E. Brezinski, "Forward-imaging instruments for optical coherence tomography," *Optics Letters*, vol. 22, pp. 1618-1620, 1997.

[27] S. Kwon and L. P. Lee, "Micromachined transmissive scanning confocal microscope," *Optics Letters*, vol. 29, pp. 706-708, 2004.

[28] Y. Yee, J. U. Bu, M. Ha, J. Choi, H. Oh, S. Lee, and H. Nam, "Fabrication and characterization of a PZT actuated micromirror with two-axis rotational motion for free space optics," *14th IEEE International Conference on Microelectromechanical Systems*, pp. 317-320, 2001.

[29] A. Jain, A. Kopa, Y. Pan, G. K. Fedder, and H. Xie, "A Two-Axis Electrothermal Micromirror for Endoscopic Optical Coherence Tomography," *IEEE Journal of Selected Topics in Quantum Electronics*, vol. 10, pp. 636-642, 2004.

[30] A. Jain, H. Qu, and S. Todd, "Electrothermal SCS micromirror with large-vertical-displacement actuation," *Proceedings of the Solid-State Sensor, Actuator, and Microsystems Workshop*, pp. 228-231, 2004.

[31] A. Jain, H. Qu, S. Todd, and H. Xie, "A thermal bimorph micromirror with large bi-directional and vertical actuation," *Sensors and Actuators A: Physical*, vol. 122, pp. 9-15, 2005.

[32] H. Xie, A. Jain, T. Xie, Y. Pan, and G. K. Fedder, "A single-crystal silicon-based micromirror with large scanning angle for biomedical applications," *Conference on Lasers and Electro-Optics*, pp. 858-860, 2003.

[33] H. J. Cho and C. H. Ahn, "Magnetically-driven bi-directional optical microscanner," *Journal of Micromechanics and Microengineering*, vol. 13, pp. 383-389, 2003.

[34] J. W. Judy and R. S. Muller, "Magnetic microactuation of torsional polysilicon structures," *Sensors and Actuators A: Physical*, vol. 53, pp. 392-397, 1996.

[35] A. D. Yalcinkaya, H. Urey, D. Brown, T. Montague, and R. Sprague, "Two-Axis Electromagnetic Microscanner for High Resolution Displays," *Journal of Microelectromechanical Systems*, vol. 15, pp. 786-794, 2006.

[36] H. Choo, D. Garmire, J. Demmel, and R. S. Muller, "Simple Fabrication Process for Self-Aligned, High-Performance Microscanners— Demonstrated Use to Generate a 2-D Ablation Pattern," *Journal of Microelectromechanical Systems*, vol. 16, pp. 260-268, 2007.

[37] R. A. Conant, J. T. Nee, K. Y. Lau, and R. S. Muller, "A flat high-frequency scanning micromirror," *Proceedings of the Solid-State Sensor and Actuator Workshop*, pp. 6-9, 2000.

[38] D. Hah, C.-A. Choi, C.-K. Kim, and C.-H. Jun, "A self-aligned vertical comb-drive actuator on an SOI wafer for a 2D scanning micromirror," *Journal of Micromechanics and Microengineering*, vol. 14, pp. 1148-1156, 2004.

[39] D. Hah, S. T.-Y. Huang, J.-C. Tsai, H. Toshiyoshi, and M. C. Wu, "Low-Voltage, Large-Scan Angle MEMS Analog Micromirror Arrays With Hidden Vertical Comb-Drive Actuators," *Journal of Microelectromechanical Systems*, vol. 13, pp. 279-289, 2004.

[40] M.-H. Kiang, O. Solgaard, K. Y. Lau, and R. S. Muller, "Electrostatic Combdrive-Actuated Micromirrors for Laser-Beam Scanning and Positioning," *Journal of Microelectromechanical Systems*, vol. 7, pp. 27-37, 1998.

[41] U. Krishnamoorthy, D. Lee, and O. Solgaard, "Self-Aligned Vertical Electrostatic Combdrives for Micromirror Actuation," *Journal of Microelectromechanical Systems*, vol. 12, pp. 458-464, 2003.

[42] K. Kumar, K. Hoshino, H.-J. Shin, R. Richards-Kortum, and X. J. Zhang, "High-reflectivity two-axis vertical combdrive microscanners for sub-cellular scale confocal imaging applications," *IEEE/LEOS International Conference on Optical MEMS and their Applications*, pp. 21-24, 2006.

[43] S. Kwon, V. Milanovic, and L. P. Lee, "Vertical Combdrive Based 2-D Gimbaled Micromirrors With Large Static Rotation by Backside Island Isolation," *IEEE Journal of Selected Topics in Quantum Electronics*, vol. 10, pp. 498-504, 2004.

[44] V. MIlanovic, M. Last, and K. S. J. Pister, "Laterally actuated torsional micromirrors for large static deflection," *IEEE Photonics Technology Letters*, vol. 15, pp. 245-247, 2003.

[45] V. Milanovic, G. A. Matus, and D. T. McCormick, "Gimbal-Less Monolithic Silicon Actuators for Tip–Tilt–Piston Micromirror Applications," *IEEE Journal of Selected Topics in Quantum Electronics*, vol. 10, pp. 462-471, 2004.

[46] P. R. Patterson, D. Hah, H. Nguyen, H. Toshiyoshi, R.-M. Chao, and M. C. Wu, "A scanning micromirror with angular vertical comb drive actuation," *15th IEEE International Conference on Microelectromechanical Systems*, pp. 544-547, 2002.

[47] W. Piyawattanametha, P. R. Patterson, D. Hah, H. Toshiyoshi, and M. C. Wu, "A 2D scanner by surface and bulk micromachined angular vertical comb actuators," *IEEE International Conference on Optical MEMS*, pp. 93-94, 2003.

[48] G.-D. J. Su, H. Toshiyoshi, and M. C. Wu, "Surface-Micromachined 2-D Optical Scanners with High-Performance Single-Crystalline Silicon Micromirrors," *IEEE Photonics Technology Letters*, vol. 13, pp. 606-608, 2001.

[49] C. Tsou, W. T. Lin, C. C. Fan, and B. C. S. Chou, "A novel self-aligned vertical electrostatic combdrives actuator for scanning micromirrors," *Journal of Micromechanics and Microengineering*, vol. 15, pp. 855-860, 2005.

[50] L. Zhou, J. M. Kahn, and K. S. J. Pister, "Scanning Micromirrors Fabricated by an SOI/SOI Wafer-Bonding Process," *Journal of Microelectromechanical Systems*, vol. 15, pp. 24-32, 2006.

[51] D. Hah, P. R. Patterson, H. D. Nguyen, H. Toshiyoshi, and M. C. Wu, "Theory and Experiments of Angular Vertical Comb-Drive Actuators for Scanning Micromirrors," *IEEE Journal of Selected Topics in Quantum Electronics*, vol. 10, pp. 505-513, 2004.

[52] K. E. Peterson, "Silicon as a Mechanical Material," *Proceedings of the IEEE*, vol. 70, pp. 420-457, 1980.

[53] C.-L. Dai, F.-Y. Xiao, Y.-Z. Juang, and C.-F. Chiu, "An approach to fabricating microstructures that incorporate circuits using a post-CMOS process," *Journal of Micromechanics and Microengineering*, vol. 15, pp. 98-103, 2005.

[54] H. Xie, Y. Pan, and G. K. Fedder, "A CMOS-MEMS mirror with curled-hinge comb drives," *Journal of Microelectromechanical Systems*, vol. 12, pp. 450-457, 2003.

[55] K. E. Peterson, "Silicon torsional scanning mirror," *IBM Journal of Research and Development*, vol. 24, pp. 631-637, 1980.

[56] D. Hah, H. Toshiyoshi, and M. C. Wu, "Design of Electrostatic Actuators for MOEMS Applications," *Proceedings of the SPIE*, vol. 4755, pp. 200-207, 2002.

[57] D. Lee, "Design and fabrication of SOI-based micromirrors for optical applications," *PhD Dissertation, Stanford University*, 2007.

[58] R. H. Webb, "Optics for laser rasters," *Applied Optics*, vol. 23, pp. 3680-3683, 1984.

[59] P. J. Brosen, "Dynamic mirror distortions in optical scanning," *Applied Optics*, vol. 11, pp. 2987-2989, 1972.

[60] S. P. Timoshenko and J. N. Goodier, *Theory of Elasticity*, 3rd ed. New York, NY: McGraw-Hill, 1970.

[61] A. P. Boresi and R. J. Schmidt, *Advanced Mechanics of Materials*, 6th ed. New York, NY: John Wiley & Sons, 2003.

[62] J. D. Plummer, M. D. Deal, and P. B. Griffin, *Silicon VLSI Technology*. Upper Saddle River, NJ 07458: Prentice Hall, Inc., 2000.

[63] K. Kumar and X. J. Zhang, "CMOS-compatible 2-axis self-aligned vertical comb-driven micromirror for large field-of-view microendoscopes," *22nd IEEE International Conference on MicroElectroMechanical Systems*, pp. 1015, 2009.

[64] J. E. Bugaj, S. Achilefu, R. B. Dorshow, and R. Rajagopalan, "Novel fluorescent contrast agents for optical imaging of *in vivo* tumors based on a receptor-targeted dye-peptide conjugate platform," *Journal of Biomedical Optics*, vol. 6, pp. 122-133, 2001.

[65] X. Gao, Y. Cui, R. M. Levenson, L. W. K. Chung, and S. Nie, "*In vivo* cancer targeting and imaging with semiconductor quantum dots," *Nature Biotechnology*, vol. 22, pp. 969-976, 2004.

[66] A. Siddiqi, L. Hui, F. Faruque, W. Williams, K. Lai, M. Hughson, S. Bigler, J. Beach, and W. Johnson, "Use of hyperspectral imaging to distinguish normal, precancerous, and cancerous cells," *Cancer Cytopathology*, vol. 114, pp. 13-21, 2008.

[67] P. R. Srinivas, B. S. Kramer, and S. Srivastava, "Trends in biomarker research for cancer detection," *The Lancet Oncology*, vol. 2, pp. 698-704, 2001.

[68] K. Carlson, I. Pavlova, T. Collier, M. R. Descour, M. Follen, and R. Richards-Kortum, "Confocal microscopy: Imaging cervical precancerous lesions," *Gynecologic Oncology*, vol. 99, pp. S84-S88, 2005.

[69] K. D. Carlson, "Fiber optic confocal microscope: *in vivo* precancer detection," *PhD Dissertation*, 2006.

[70] S. Kimura and T. Wilson, "Confocal scanning optical microscope using single-mode fiber for signal detection," *Applied Optics*, vol. 30, pp. 2143-2150, 1991.

[71] M. T. Tilli, M. C. Cabrera, A. R. Parrish, K. M. Torre, M. K. Sidawy, and A. L. Gallagher, "Real-time imaging and characterization of human breast tissue by reflectance confocal microscopy," *Journal of Biomedical Optics*, vol. 12, pp. 051901, 2007.

[72] M. S. Rahman, K. Sokolov, R. Richards-Kortum, T. Tkaczyk, and M. R. Descour, "High resolution optical imaging of pre-cancer with structured illumination - an integrated approach," *Conference on Lasers and Electro-Optics*, pp. 2224-2226, 2005.

[73] K.-B. Sung, C. Liang, M. R. Descour, T. Collier, M. Follen, A. Malpica, and R. Richards-Kortum, "Near real time *in vivo* fibre optic confocal microscopy: sub-cellular structure resolved," *Journal of Microscopy*, vol. 207, pp. 137-145, 2002.

[74] K.-B. Sung, R. Richards-Kortum, M. Follen, A. Malpica, C. Liang, and M. R. Descour, "Fiber optic reflectance microscopy: a new real time technique to view nuclear morphology in cervical squamous epithelium *in vivo*," *Optics Express*, vol. 11, pp. 3171-3181, 2003.

[75] C. Liang, M. R. Descour, K.-B. Sung, and R. Richards-Kortum, "Fiber confocal reflectance microscope (FCRM) for *in-vivo* imaging," *Optics Express*, vol. 9, pp. 821-830, 2001.

[76] A. R. Rouse, A. Kano, J. A. Udovich, S. M. Kroto, and A. F. Gmitro, "Design and demonstration of a miniature catheter for a confocal microendoscope," *Applied Optics*, vol. 43, pp. 5763-5771, 2004.

[77] K.-B. Sung, C. Liang, M. R. Descour, T. Collier, M. Follen, and R. Richards-Kortum, "Fiber-optic confocal reflectance microscope with miniature objective for *in vivo* imaging of human tissues," *IEEE Transactions on Biomedical Engineering*, vol. 49, pp. 1168-1172, 2002.

[78] M. R. Descour, A. H. O. Karkainnen, J. D. Rogers, C. Liang, R. S. Weinstein, J. T. Rantala, B. Kilic, E. Madenci, R. Richards-Kortum, E. V. Ansyln, R. D. Dupuis, R. J. Schul, C. G. Willison, and C. P. Tiggers, "Toward the develpoment of miniaturized imaging systems for detection of pre-cancer," *IEEE Journal of Quantum Electronics*, vol. 38, pp. 122-130, 2002.

[79] D. L. Dickensheets and G. S. Kino, "Micromachined scanning confocal optical microscope," *Optics Letters*, vol. 21, pp. 764-766, 1996.

[80] D. L. Dickensheets and G. S. Kino, "Silicon-micromachined scanning confocal optical microscope," *Journal of Microelectromechanical Systems*, vol. 7, pp. 38-47, 1998.

[81] C. L. Hoy, N. J. Durr, P. Chen, W. Piyawattanametha, H. Ra, O. Solgaard, and A. Ben-Yakar, "Miniaturized probe for femtosecond laser microsurgery and two-photon imaging," *Optics Express*, vol. 16, pp. 9996-10005, 2008.

[82] S. S. Rege, T. S. Tkaczyk, and M. R. Descour, "Application of the Alvarez-Humphrey concept to the design of a miniaturized scanning microscope," *Optics Express*, vol. 12, pp. 2574-2588, 2004.

[83] W. Piyawattanametha, R. P. J. Barretto, T. H. Ko, B. A. Flusberg, E. D. Cocker, H. Ra, D. Lee, O. Solgaard, and M. J. Schnitzer, "Fast-scanning two-photon fluorescence imaging based on a microelectromechanical systems two-dimensional scanning mirror," *Optics Letters*, vol. 31, pp. 2018-2020, 2006.

[84] K. Kumar, R. Avritscher, D. C. Madoff, and X. J. Zhang, "Handheld single-cell-layer optical sectioning reflectance confocal microscope for interventional imaging," presented at 29th Conference on Lasers and Electro Optics, Baltimore, MD, 2009 (accepted).

[85] K. Kumar, K. Hoshino, and X. Zhang, "Handheld subcellular-resolution single-fiber confocal microscope using high-reflectivity two-axis vertical combdrive silicon microscanner," *Biomedical Microdevices*, vol. 10, pp. 653-660, 2008.

[86] K. C. Maitland, H.-J. Shin, H. Ra, D. Lee, O. Solgaard, and R. Richards-Kortum, "Single fiber confocal microscope with a two-axis gimbaled MEMS scanner for cellular imaging," *Optics Express*, vol. 14, pp. 8604-8612, 2006.

[87] J. T. C. Liu, M. J. Mandella, H. Ra, L. K. Wong, O. Solgaard, G. S. Kino, W. Piyawattanametha, C. H. Contag, and T. D. Wang, "Miniature near-infrared dual axes confocal microscope utilizing a two-dimensional microelectromechanical systems scanner," *Optics Letters*, vol. 32, pp. 256-258, 2007.

[88] H. Ra, W. Piyawattanametha, M. J. Mandella, P.-L. Hsiung, J. Hardy, T. D. Wang, C. H. Contag, G. S. Kino, and O. Solgaard, "Three-dimensional *in vivo* imaging by a handheld dual-axes confocal microscope," *Optics Express*, vol. 16, pp. 7224-7232, 2008.

[89] X. Gan, S. P. Schilders, and M. Gu, "Image enhancement through turbid media under a microscope by use of polarization gating methods," *Journal of the Optical Society of America A*, vol. 16, pp. 2177-2184, 1999.

[90] J. M. Schmitt, A. H. Gandjbakhche, and R. F. Bonner, "Use of polarized light to discriminate short-path photons in a multiply scattering medium," *Applied Optics*, vol. 31, pp. 6535-6546, 1992.

[91] M. Gu, C. J. R. Sheppard, and X. Gan, "Image formation in a fiber-optical confocal scanning microscope," *Journal of the Optical Society of America A*, vol. 8, pp. 1755-1761, 1991.

[92] T. Wilson and A. R. Carlini, "Size of the detector in confocal imaging systems," *Optics Letters*, vol. 12, pp. 227-229, 1987.

[93] J. W. Goodman, *Introduction to Fourier Optics*, Third ed. Greenwood Village, CO: Roberts & Company Publishers, 2004.

[94] M. Rajadhyaksha, R. R. Anderson, and R. H. Webb, "Video-rate confocal scanning laser microscope for imaging human tissues *in vivo*," *Applied Optics*, vol. 38, pp. 2105-2115, 1999.

[95] K. Carlson, M. Chidley, K.-B. Sung, M. R. Descour, A. Gillenwater, M. Follen, and R. Richards-Kortum, "*In vivo* fiber-optic confocal reflectance microscope with an injection-molded plastic miniature objective lens," *Applied Optics*, vol. 44, pp. 1792-1797, 2005.

[96] S. Achilefu, R. B. Dorshow, J. E. Bugaj, and R. Rajagopalan, "Novel receptor-targeted fluorescence contrast agents for in vivo tumor imaging," *Investigative Radiology*, vol. 35, pp. 479-485, 2000.

[97] J. V. Frangioni, "*In vivo* near-infrared fluorescence imaging," *Current Opinion in Chemical Biology*, vol. 7, pp. 626-634, 2003.

[98] J. S. Reynolds, T. L. Troy, R. H. Mayer, A. B. Thompson, D. J. Waters, K. K. Cornell, P. W. Snyder, and E. M. Sevick-Muraka, "Imaging of spontaneous canine mammary tumors using fluorescent contrast agents," *Photochemistry and Photobiology*, vol. 70, pp. 87-94, 2008.

[99] G. A. Wagnieres, W. M. Star, and B. C. Wilson, "*In vivo* fluorescence spectroscopy and imaging for oncological applications," *Photochemistry and Photobiology*, vol. 68, pp. 603-632, 2008.

[100] A. Horton, K. Kumar, H. Liu, L. Cheng, N. Lane, E. Taylor, H. R. Garner, J. W. Uhr, and X. J. Zhang, "Quantitative immunophenotyping of circulating tumor cells in blood using microfluidic screening chip integrated with hyperspectral microscope," *15th International Conference on Solid-State Sensors, Actuators, and Microsystems*, 2009 (accepted).

[101] H. Eerola, M. Heinonen, P. Heikkila, O. Kilpivaara, A. Tamminen, K. Aittomaki, C. Blomqvist, A. Ristimaki, and H. Nevanlinna, "Basal cytokeratins in breast tumours among BRCA1, BRCA2 and mutation-negative breast cancer families," *Breast Cancer Research*, vol. 10, pp. R17, 2008.

[102] R. I. Nicholson, J. M. Gee, and M. E. harper, "EGFR and cancer prognosis," *European Journal of Cancer*, vol. 37, pp. S9-S15, 2001.

[103] D. J. Slamon, B. Leyland-Jones, S. Shak, H. Fuchs, V. Paton, A. Bajamonde, T. Fleming, W. Eiermann, J. Wolter, M. Pegram, J. Baselga, and L. Norton, "Use of Chemotherapy plus a Monoclonal Antibody against HER2 for Metastatic Breast Cancer That Overexpresses HER2," *New England Journal of Medicine*, vol. 344, pp. 783-792, 2001.

[104] A. Urruticoechea, I. E. Smith, and M. Dowsett, "Proliferation marker Ki-67 in early breast cancer," *Journal of Clinical Oncology*, vol. 23, pp. 7212-7220, 2005.

[105] C. Ginestier, M. Hur, E. Charafe-Jauffret, F. Monville, J. Dutcher, M. Brown, J. Jacquemier, P. Viens, C. Kleer, and S. Liu, "ALDH1 Is a Marker of Normal and Malignant Human Mammary Stem Cells and a Predictor of Poor Clinical Outcome," *Cell Stem Cell*, vol. 1, pp. 555-567, 2007.

[106] N. O. Brien, T. M. Maguire, N. O. Donovan, N. Lynch, A. D. K. HIll, E. McDermott, N. O. Higgins, and M. J. Duffy, "Mammaglobin A: A promising marker for breast cancer," *Clinical Chemistry*, vol. 48, pp. 1362-1364, 2002.

[107] I. Brotherick, C. N. Robson, D. A. Browell, J. Shenfine, M. D. White, W. J. Cunliffe, B. K. Shenton, M. Egan, L. A. Webb, L. G. Lunt, J. R. Young, and M. J. HIggs, "Cytokeratin expression in breast cancer: phenotypic changes associated with disease progression," *Cytometry*, vol. 32, pp. 301-308, 1998.

[108] R. H. Schreiber, S. Pendas, N. N. Ku, D. S. Reintgen, A. R. Shons, C. Berman, D. Boulware, and C. E. Cox, "Microstaging of breast cancer patients using cytokeratin staining of the sentinel lymph node," *Annals of Surgical Oncology*, vol. 6, pp. 95-101, 1999.

[109] O. Zach and D. Lutz, "Mammaglobin remains a useful marker for the detection of breast cancer cells in peripheral blood," *Journal of Clinical Oncology*, vol. 23, pp. 3160-3161, 2005.

[110] B. K. Zehentner, D. H. Persing, A. Deme, P. Toure, S. E. Hawes, L. Brooks, Q. Feng, D. C. Hayes, C. W. Critichlow, R. L. Houghton, and N. B. Kiviat, "Mammaglobin as a novel breast cancer biomarker: Multigene reverse transcription-PCR assay and sandwich ELISA," *Clinical Chemsitry*, vol. 50, pp. 2069-2076, 2004.

[111] A. B. Parthasarathy, W. J. Tom, A. Gopal, X. J. Zhang, and A. K. Dunn, "Robust flow measurement with multi-exposure speckle imaging," *Optics Express*, vol. 16, pp. 1975-1989, 2008.

[112] K. Kumar, T. E. Milner, and X. J. Zhang, "Microelectromechanical systems scanners enable *in vivo* 3D optical coherence tomography," *BioOptics World*, vol. 1, pp. 31-34, 2008.

[113] A. Sergeev, V. Gelikonov, G. Gelikonov, F. Feldchtein, R. Kuranov, N. Gladkova, N. Shakhova, L. Snopova, A. Shakhov, I. Kuznetzova, A. Denisenko, V. Pochinko, Y. Chumakov, and O. Streltzova, "In vivo endoscopic OCT imaging of precancer and cancer states of human mucosa," *Opt. Express*, vol. 1, pp. 432-440, 1997.

[114] G. J. Tearney, S. A. Boppart, B. E. Bouma, M. E. Brezinski, N. J. Weissman, J. F. Southern, and J. G. Fujimoto, "Scanning single-mode fiber optic catheter-endoscope for optical coherence tomography," *Optics Letters*, vol. 21, pp. 543-545, 1996.

[115] G. J. Tearney, M. E. Brezinski, B. E. Bouma, S. A. Boppart, C. Pitris, J. F. Southern, and J. G. Fujimoto, "In Vivo Endoscopic Optical Biopsy with Optical Coherence Tomography," *Science*, vol. 276, pp. 2037-2039, 1997.

[116] P. H. Tran, D. S. Mukai, M. Brenner, and Z. Chen, "*In vivo* endoscopic optical coherence tomography by use of a rotational microelectromechanical system probe," *Optics Letters*, vol. 29, pp. 1236-1238, 2004.

[117] D. Huang, E. A. Swanson, C. P. Lin, J. S. Schuman, W. G. Stinson, W. Chang, M. R. Hee, T. Flotte, K. Gregory, C. A. Puliafito, and J. G. Fujimoto, "Optical coherence tomography," *Science*, vol. 254, pp. 1178-1181, 1991.

[118] S. J. N. Gladkova, F. Feldchtein, A. Terentieva, B. Brand, G. Gelikonov, V. Gelikonov, A. Sergeev, A. Fritscher-Ravens, J. Freund, U. Seitz, S. Schroder, and N. Soehendra, "In vivo endoscopic optical coherence tomography of esophagitis, Barrett's esophagus, and adenocarcinoma of the esophagus," *Endoscopy*, vol. 32, pp. 750-755, 2000.

[119] P. F. Escobar, J. L. Belinson, A. White, N. M. Shakova, F. I. Feldchtein, M. V. Kareta, and N. D. Gladkova, "Diagnostic efficacy of optical coherence tomography in the management of preinvasive and invasive cancer of uterine cervix and vulva," *International Journal of Gynecological Cancer*, vol. 14, pp. 470-474, 2004.

[120] J. M. Poneros, S. Brand, B. E. Bouma, G. J. Tearney, C. C. Compton, and N. S. Nishioka, "Diagnosis of specialized intestinal metaplasia by optical coherence tomography," *Gastroenterology*, vol. 120, pp. 7-12, 2001.

[121] Y. Pan, J. P. Lavelle, S. I. Bastacky, S. Meyers, G. Pirtskhalaishvili, M. L. Zeidel, and D. L. Farkas, "Detection of tumorigenesis in rat bladders with optical coherence tomography," *Medical Physics*, vol. 28, pp. 2432-2440, 2001.

[122] S. A. Boppart, W. Luo, D. L. Marks, and K. W. Singletary, "Optical Coherence Tomography: Feasibility for Basic Research and Image-guided Surgery of Breast Cancer," *Breast Cancer Research and Treatment*, vol. 84, pp. 85-97, 2004.

[123] S. B. Colak, M. B. van der Mark, G. W. t Hooft, J. H. Hoogenraad, E. S. van der Linden, and F. A. Kuijpers, "Clinical optical tomography and NIR spectroscopy for breast cancer detection," *Selected Topics in Quantum Electronics, IEEE Journal of*, vol. 5, pp. 1143-1158, 1999.

[124] W. Luo, F. T. Nguyen, A. M. Zysk, T. S. Ralston, J. Brockenbrough, D. L. Marks, A. L. Oldenburg, and S. A. Boppart, "Optical biopsy of lymph node morphology using optical coherence tomography," *Technology in Cancer Research and Treatment*, vol. 4, pp. 539-547, 2005.

[125] A. M. Zysk and S. A. Boppart, "Computational methods for analysis of human breast tumor tissue in optical coherence tomography images," *Journal of Biomedical Optics*, vol. 11, pp. 054015-7, 2006.

[126] B. E. Bouma and G. J. Tearney, "Power-efficient nonreciprocal interferometer and linear-scanning fiber-optic catheter for optical coherence tomography," *Optics Letters*, vol. 24, pp. 531-533, 1999.

[127] B. A. Flusberg, J. C. Jung, E. D. Cocker, E. P. Anderson, and M. J. Schnitzer, "*In vivo* brain imaging using a portable 3.9 gram two-photon fluorescence microendoscope," *Optics Letters*, vol. 30, pp. 2272-2274, 2005.

[128] A. L. Polglase, W. J. McLaren, S. A. Skinner, R. Kiesslich, M. F. Neurath, and P. M. Delaney, "A fluorescence confocal endomicroscope for *in vivo* microscopy of the upper- and the lower-GI tract," *Gastrointestinal Endoscopy*, vol. 62, pp. 686-695, 2005.

[129] K. Kumar, T. E. Milner, and X. J. Zhang, "Biomedical Imaging: MEMS scanners enable *in vivo* 3-D OCT," *Laser Focus World*, vol. 44, pp. 87-90, 2008.

[130] A. D. Aguirre, P. R. Hertz, Y. Chen, J. G. Fujimoto, W. Piyawattanametha, L. Fan, and M. C. Wu, "Two-axis MEMS scanning catheter for ultrahigh resolution

three-dimensional and en face imaging," *Optics Express*, vol. 15, pp. 2445-2453, 2007.

[131] W. Jung, J. Zhang, L. Wang, P. Wilder-Smith, Z. Chen, D. T. McCormick, and N. C. Tien, "Three-dimensional optical coherence tomography employing a 2-axis microelectromechanical scanning mirror," *IEEE Journal of Selected Topics in Quantum Electronics*, vol. 11, pp. 806-810, 2005.

[132] Y. Pan, H. Xie, and G. K. Fedder, "Endoscopic optical coherence tomography based on a microelectromechanical mirror," *Optics Letters*, vol. 26, pp. 1966-1968, 2001.

[133] T. Xie, H. Xie, G. K. Fedder, and Y. Pan, "Endoscopic optical coherence tomography with a modified microelectromechanical systems mirror for detection of bladder cancers," *Applied Optics*, vol. 42, pp. 6422-6426, 2003.

[134] M. Choma, M. Sarunic, C. Yang, and J. Izatt, "Sensitivity advantage of swept source and Fourier domain optical coherence tomography," *Optics Express*, vol. 11, pp. 2183-2189, 2003.

[135] R. Leitgeb, C. Hitzenberger, and A. Fercher, "Performance of fourier domain vs. time domain optical coherence tomography," *Optics Express*, vol. 11, pp. 889-894, 2003.

[136] Y. Yasuno, V. D. Madjarova, S. Makita, M. Akiba, A. Morosawa, C. Chong, T. Sakai, K.-P. Chan, M. Itoh, and T. Yatagai, "Three-dimensional and high-speed swept-source optical coherence tomography for *in vivo* investigation of human anterior eye segments," *Optics Express*, vol. 13, pp. 10652-10664, 2005.

[137] S. R. Chinn, E. A. Swanson, and J. G. Fujimoto, "Optical coherence tomography using a frequency-tunable optical source," *Optics Letters*, vol. 22, pp. 340-342, 1997.

[138] K. Kumar, J. C. Condit, A. McElroy, N. J. Kemp, K. Hoshino, T. E. Milner, and X. Zhang, "Forward-Imaging Swept Source Optical Coherence Tomography using Silicon MEMS Scanner for High-Speed 3-D Volumetric Imaging," presented at Optical MEMS and Nanophotonics, 2007 IEEE/LEOS International Conference on, 2007.

[139] K. Kumar, J. C. Condit, A. McElroy, N. J. Kemp, K. Hoshino, T. E. Milner, and X. Zhang, "Fast 3D in vivo swept-source optical coherence tomography using a two-axis MEMS scanning micromirror," *Journal of Optics A: Pure and Applied Optics*, pp. 044013, 2008.

[140] J. M. v. Houten and M. H. A. J. Herben, "The elliptical Fresnel-zone plate antenna," presented at Ninth International Conference on Antennas and Propagation, Eindhoven, Netherlands, 1995.

[141] M. Young, "Zone Plates and Their Aberrations," *Journal of the Optical Society of America*, vol. 62, pp. 972-976, 1972.

[142] Q. Cao and J. Jahns, "Comprehensive focusing analysis of various Fresnel zone plates," *Journal of the Optical Society of America A*, vol. 21, pp. 561-571, 2004.

[143] K. Kumar, H. Cao, and X. J. Zhang, "Monolithic integration of binary-phase Fresnel zone plate objectives on 2-axis scanning micromirrors for compact

microendoscopes," presented at 2008 Solid-State Sensors, Actuators, and Microsystems Workshop, Hilton Head Island, SC, 2008.

[144] R. R. A. Syms and A. Lohmann, "MOEMS tuning element for a Littrow external cavity laser," *Journal of Microelectromechanical Systems*, vol. 12, pp. 921-928, 2003.

Vita

Karthik Kumar was born in Chennai, India, on November 12, 1981, the son of Mrs. Chitra and Mr. M. D. Venkatakumar. He attended D.A.V. (CBSE) Senior Secondary School in Gopalapuram, Chennai. In September 1999, he was admitted at the University of Madras in Chennai, India, where he received his undergraduate degree in Electronics and Communication Engineering. He enrolled in the Electrical and Computer Engineering graduate program at the University of Texas at Austin in September 2003. While a Master's student, he interned at the Photonics and Electronics Research Laboratory at Agilent, Inc., investigating plasma diagnostic tools for in-process testing of active-matrix thin-film transistors for organic-LED displays. Karthik earned his Master of Science degree in Electrical and Computer Engineering from the University of Texas at Austin in December 2005. His thesis research, supervised by Dr. Thomas E. Milner and Dr. H. Grady Rylander III, focused on bandwidth multiplexing techniques in swept-source optical coherence tomography. Since then, he has specialized in optical and fluidic microelectromechanical systems for early cancer detection under the guidance of Dr. John X. J. Zhang.

Permanent address: 'Chitrakoot', 2nd Cross Street
Singaravelan Main Road, Chinna Neelankarai
Chennai, Tamil Nadu 600 041, India

This dissertation was typed by the author.